

## ABSTRACT

Title of dissertation: A SEARCH FOR MUON NEUTRINOS  
COINCIDENT WITH GAMMA-RAY BURSTS  
WITH THE ICECUBE 59-STRING DETECTOR

Peter C. Redl, Doctor of Philosophy, 2011

Dissertation directed by: Professor Gregory Sullivan  
Department of Physics

Gamma-Ray Bursts (GRBs) are believed to be prime candidates to produce the cosmic ray flux above  $10^{18}$ eV. Cosmic rays are deflected by galactic and intergalactic magnetic fields and do not point back to their source, therefore cosmic ray observations cannot confirm or rule out GRBs as a source. Leading theories predict that if GRBs are indeed responsible for the highest energy cosmic rays, then they would produce a detectable TeV-scale neutrino flux in a  $\text{km}^3$  sized neutrino detector. Neutrinos are not deflected by magnetic fields and point back to their source, making it possible to correlate a neutrino flux with its source. The detection of a neutrino flux from GRBs would be strong evidence that GRBs are a source of the highest energy cosmic rays.

IceCube is the first  $\text{km}^3$  sized neutrino detector in the world and is therefore sensitive to the predicted TeV neutrino flux from GRBs. The finished detector consists of 5160 light-sensitive Digital Optical Modules (DOM) arranged on 86 Strings. There are 60 DOMs on a single string deployed at depths between 1450 and 2450

meters below the surface. The first IceCube String was deployed during the South Pole summer of 2004-2005 with construction of the IceCube detector finishing during the austral summer of 2011. The results presented here are from the 59-string detector, which operated from May 2009 to May 2010. IceCube is able to detect charged particles moving through its instrumented volume near the speed of light by detecting the Cherenkov light given off by those charged particles. Muon and anti-muon neutrinos produce secondary muons if they interact with a nucleon. If this interaction happens in or near the instrumented volume IceCube can detect those secondary muons. By searching for a neutrino signal coincident in time and space with satellite detected gamma rays from GRBs, the analysis presented here pushes the sensitivity for neutrinos from GRBs to 0.46 times the theoretically predicted neutrino flux. The result is combined with the previous search and a combined 90% upper limit of 0.22 times the theoretical predicted flux is set. The implication of this stringent limit on the model is discussed and future IceCube sensitivities are outlined.

IceCube is the largest neutrino detector in the world and with this result has entered the era of neutrino astrophysics by constraining long standing astrophysical neutrino production models.

A SEARCH FOR MUON NEUTRINOS COINCIDENT WITH  
GAMMA-RAY BURSTS WITH THE ICECUBE 59-STRING  
DETECTOR

by

Peter Christian Redl

Dissertation submitted to the Faculty of the Graduate School of the  
University of Maryland, College Park in partial fulfillment  
of the requirements for the degree of  
Doctor of Philosophy  
2011

Advisory Committee:

Dr. Gregory Sullivan, Chair/Advisor

Dr. Cole Miller, Deans Representative

Dr. Kara Hoffman,

Dr. Paulo Bedaque

Dr. Erik Blaufuss

© Copyright by  
Peter Christian Redl  
2010

## Dedication

I dedicate this to my family. I have received encouragement in all of my pursuits, without which I would not have completed this work.

## Acknowledgments

First and foremost, I would like to thank my family. Throughout my life I have been encouraged to follow my dreams, make my own mistakes and discoveries. Without this encouragement I would not have become a scientist. I would also like to thank my adviser, Greg Sullivan, for giving me a chance to work on this incredible experiment. I would like to thank him for allowing me to go to the South Pole, which is among the most incredible experiences of my life. Moreover, Greg has encouraged me to pursue my own interests, while providing valuable insights when necessary.

I would also like to thank Erik Blaufuss for patiently answering all of my questions. He guided my research by keeping me on track, making sure I understood what was important and what was not. Moreover, he saved me from getting stuck in computing 'hell' more than once by quickly fixing computing problems. Without Kara Hoffman I would likely still be working on an analysis that received little encouragement from the collaboration and was not very interesting. For helping me change my research focus I owe her my thanks! I would also like to thank John Pretz and Phil Roth, who were the 'old' graduate students when I joined the group. Both John and Phil helped me with my 'Noob' programming and physics questions, always patiently answering, never getting outwardly annoyed with me. Alex Olivas and Henrike Wissing have helped me complete this work by helping me with Monte Carlo simulations, furthermore they helped me on a personal level with 'nerd camp'. I would like to thank my fellow graduate students Brian, Kevin and Warren. Brian always had an open ear for all of my personal issues and provided

me with some valuable advise. Kevin's help with statistics questions, and great computing ideas have helped me throughout my graduate student career. Warren's great insight into physics and life has helped make my tenure as a graduate student easier to endure. The new graduate students, Rob and Mike have helped me put my own research into perspective by asking questions that made me think about my research from an outsiders point of view. Special thanks to Robert for reading my thesis and giving me helpful comments! Last but not least I would like to thank the research coordinators that have made my life much easier by always helping the absent minded scientist in me. Thank you Helina, Rozi and Naomi!

IceCube is a collaboration and without the hard work of a lot of people it would not have been possible and I want to thank the entire collaboration. There are a few people I would like to point out who have helped me especially. These people include Anna Franckowiak, Ignacio Taboada, Alexander Kappes, Levent Demiroers, Lotfi, Torsten Schmidt and Francis Halzen. Ignacio and Alexander have given me valuable input to my work and have helped me be a better physicist. Levent and Lotfi, reviewed my analysis and provided me with valuable input after going through my analysis with a fine tooth comb. Francis has helped me put my physics result into perspective and his unwavering optimism has helped make IceCube possible in the first place. Without Francis there would be no 'IceCube' for me to work on! Torsten helped me immensely with my service work and made a difficult task more interesting and a lot easier. Anna has helped me during my last stressful year in graduate school immensely by keeping an open ear! There are other people in IceCube that I feel like I should thank but this section could easily grow to epic

proportions if I named everybody, therefore let me just say: Thank you IceCube!

On a personal level I would like to thank all of my roommates who put up with my annoying habits and my friends who made graduate school a more pleasant experience! I would like to point out Brad Conrad, Colin McCann and Patricia Tierney who have listened to my concerns and complaints and helped each in their own way to make it through graduate school. Brad was always willing to listen to my concerns and gave me some valuable advice during my time as a graduate student. Colin and I took a very similar path through graduate school even though we were doing very different research. It helped me enormously talking to somebody who had an open ear and understood what I was going through. Patricia was there for me during some of the most difficult times of my life (when my father passed away for example) and never grew tired of me. She has also accomplished some incredible things in her life that made me not only proud, but also encouraged me in my own pursuits! There are many people that I am missing here that have had a great impact on my life, including some great friends from college and grad school (James, Jianhao, Eric E., Ed, Julie, Joe, Simon, Mike, Eric P., Brian, Ryan to name a few) and from school before that (Marcus, Jason, Kerstin, Marta, Hans, Christina, Mr. Konnie to name a few) and I want to say thank you to all of you!

Finally I would like to thank specific members of my family that have especially helped me throughout my life. First of all there is my mother, Wilfriede, who has always encouraged me and has been there for me throughout my life. It wasn't easy being a single mom raising me and I want to thank her for always finding the time to give me a great home, 'danke Mama'! I want to thank my grandparents who

have opened their home to me whenever I wanted to visit and made my childhood more fun and interesting. I would like to thank my grandfather for letting me play in his workshop and learn about electronics, steam engines and whatever else I was interested in. My grandmother on the other hand always provided a good meal, good conversations and good advice for which I am grateful. I have always had great respect for my uncle Reinhold who passed away far too soon, and I will always remember the advice and guidance he has given me. I would like to thank my stepfather, John, for opening his home to me and helping me through my teenage years. My father, Gustav, made my childhood more fun by telling me great stories, and lightening the mood whenever I felt overwhelmed, for which I am thankful. It saddens me that he passed away before I could complete this work, however, his love for logic problems and mathematics have been passed on to me, which has helped me throughout the years. Finally I would like to thank my cousin, Karin. Her positive attitude in life and great friendship throughout the years have had a very positive impact on my life! As with the previous sections there are many people I am missing here, but know that I am grateful to all of you! Thank you everybody!

I acknowledge financial support from the University of Maryland and NSF, without which this work would not have been possible.

# Table of Contents

List of Tables	x
List of Figures	xi
List of Abbreviations	xiv
1 Introduction	1
2 Gamma-ray Bursts	5
2.1 History . . . . .	5
2.2 Theory . . . . .	9
2.2.1 Introduction . . . . .	9
2.2.2 The Fireball Model . . . . .	10
2.2.3 Neutrino Production in the Fireball . . . . .	12
2.2.3.1 The Bulk Lorentz factor $\Gamma$ . . . . .	18
3 IceCube	20
3.1 Detection Principle . . . . .	22
3.1.1 Neutrino Interaction . . . . .	22
3.1.2 Muon Propagation . . . . .	23
3.1.3 Detecting Muons . . . . .	25
3.2 The Ice . . . . .	26
3.3 The Optical Detectors . . . . .	28
3.4 Online Systems . . . . .	33
3.4.1 Experiment Control - IceCube Live . . . . .	33
3.4.2 Data Acquisition . . . . .	33
3.4.3 Triggers . . . . .	35
3.4.3.1 Simple Multiplicity Trigger . . . . .	35
3.4.4 Processing and Filtering . . . . .	37
3.4.5 Filters . . . . .	41
3.4.5.1 The Muon Filter . . . . .	41
3.4.5.2 The Extremely High Energy Filter . . . . .	42
3.5 Calibration . . . . .	43
3.5.1 Timing Calibration . . . . .	43
3.5.2 DOM Calibration . . . . .	44
3.5.3 Geometry Calibration . . . . .	48
3.6 Effective Area . . . . .	49
3.7 Simulation . . . . .	50
4 Reconstruction Techniques in IceCube	54
4.1 DOM Cleaning . . . . .	54
4.2 DOM Calibration . . . . .	55
4.2.1 Droop Correction . . . . .	55

4.3	Feature Extraction . . . . .	57
4.4	Time Window Cleaning . . . . .	58
4.5	Reconstructions used in this analysis . . . . .	58
4.5.1	LineFit . . . . .	59
4.5.2	Maximum Likelihood Reconstruction . . . . .	60
4.5.2.1	Probability Density Function . . . . .	61
4.5.2.2	The Pandel Function . . . . .	64
4.6	Specific LogLikelihood based reconstructions used in this thesis . . . . .	67
4.6.1	Single Photoelectron Fits (SPE) . . . . .	67
4.6.2	Multiple Photoelectron Fits . . . . .	68
4.6.3	Paraboloid Fit . . . . .	70
4.6.4	Bayesian Up/Down Fit . . . . .	72
4.6.5	Energy Reconstruction . . . . .	73
4.7	The Topological Trigger . . . . .	73
5	GRB Selection . . . . .	76
5.1	Gamma-ray Burst Coordinate Network . . . . .	76
5.2	Satellites . . . . .	77
5.2.1	The Fermi Gamma-ray Space Telescope . . . . .	77
5.2.1.1	Gamma-ray Burst Monitor (GBM) . . . . .	78
5.2.1.2	Large Area Telescope (LAT) . . . . .	79
5.2.2	Swift . . . . .	80
5.2.3	Third Interplanetary Network (IPN3) . . . . .	85
5.2.3.1	Konus/Wind . . . . .	86
5.2.3.2	Agile . . . . .	86
5.2.3.3	Suzaku . . . . .	86
5.2.3.4	Integral . . . . .	87
5.2.4	Satellite Summary . . . . .	87
5.3	The IceCube 59-string GRB catalog . . . . .	88
5.3.0.1	GRB Neutrino Spectra Calculation . . . . .	88
6	Analysis Techniques . . . . .	100
6.1	Event selection . . . . .	100
6.2	Decision Trees . . . . .	101
6.2.1	Decision Trees technical details . . . . .	101
6.3	Boosting Algorithms . . . . .	102
6.3.1	AdaBoost . . . . .	103
6.4	Unbinned Likelihood Method . . . . .	104
7	Northern Hemisphere Search . . . . .	110
7.1	GRB Triggers . . . . .	110
7.2	IceCube Data . . . . .	111
7.2.1	Pre-selection Cuts . . . . .	111
7.3	Simulation . . . . .	113
7.4	Processing . . . . .	113

7.5	Boosted Decision Tree . . . . .	114
7.6	Unbinned Likelihood Method . . . . .	118
7.6.1	The Space PDF . . . . .	118
7.6.2	The Time PDF . . . . .	119
7.6.3	The Energy PDF . . . . .	120
7.6.4	The Test Statistic . . . . .	121
7.7	Cut Optimization . . . . .	121
7.7.1	Optimizing for discovery . . . . .	123
7.7.2	Optimizing for a Limit . . . . .	124
7.8	Analysis Potential . . . . .	126
7.9	Systematics . . . . .	128
7.9.1	Individual tunable parameters . . . . .	129
7.9.1.1	Dom Sensitivity . . . . .	129
7.9.1.2	Neutrino Cross Section . . . . .	130
7.9.1.3	Seasonal Variation . . . . .	130
7.9.1.4	The IceModel . . . . .	133
7.9.2	The Total Systematic error . . . . .	133
7.10	Result of this Analysis . . . . .	134
7.11	Combining this result with the previous result . . . . .	134
8	Discussion of the result . . . . .	136
8.1	Discussion of the Result . . . . .	136
9	Conclusion and Outlook . . . . .	145
9.1	Conclusion . . . . .	145
A	Shock Acceleration . . . . .	147
A.1	Accelerating Particles . . . . .	147
A.1.1	Fermi acceleration . . . . .	147
A.1.1.1	First order Fermi acceleration . . . . .	147
A.1.1.2	Physics inside the shock wave . . . . .	150
A.1.1.3	Second Order Fermi acceleration . . . . .	152
B	Neyman Limit and Combining Limits . . . . .	153
B.1	Neyman Limits . . . . .	153
B.2	Combining Limits . . . . .	154
B.2.1	Brute Force . . . . .	154
B.2.2	The Analytic Method . . . . .	154
B.2.2.1	Combining limits . . . . .	156
B.2.3	Conclusion . . . . .	156
	Bibliography . . . . .	157

## List of Tables

5.1	Satellite Parameters . . . . .	87
5.2	Average Parameters . . . . .	91
5.3	Burst Parameters . . . . .	92
5.4	Burst Spectrum Parameters . . . . .	95
7.1	Cuts summary . . . . .	115
7.2	DOM sensitivity . . . . .	129
7.3	Neutrino Cross Section . . . . .	130
7.4	Background Rate Variation . . . . .	133
7.5	Total Systematic Error . . . . .	133

## List of Figures

2.1	The BATSE Skymap . . . . .	6
2.2	BATSE burst durations . . . . .	7
2.3	Fireball Cartoon . . . . .	10
2.4	GRB $\gamma$ and $\nu$ Emission . . . . .	13
3.1	IceCube . . . . .	21
3.2	Feynman Diagrams for Neutrino Interactions . . . . .	23
3.3	Neutrino Cross Sections . . . . .	24
3.4	Muon Energy Loss in Ice . . . . .	25
3.5	Ice Properties . . . . .	27
3.6	DOM . . . . .	28
3.7	DOM QE . . . . .	31
3.8	Cherenkov light intensity . . . . .	32
3.9	I3Live . . . . .	34
3.10	DAQ . . . . .	36
3.11	The PnF system . . . . .	38
3.12	SPS Processing Times . . . . .	40
3.13	RAPCal . . . . .	45
3.14	ChargeHistogram . . . . .	48
3.15	EffectiveArea . . . . .	50
4.1	Droop Correction . . . . .	56
4.2	LineFitVelocity . . . . .	60
4.3	Cerenkov . . . . .	62

4.4	Pandel Function . . . . .	65
4.5	Delta . . . . .	69
4.6	Delta . . . . .	71
4.7	EnergyResolution . . . . .	74
5.1	GCN . . . . .	77
5.2	Fermi . . . . .	81
5.3	Swift . . . . .	83
5.4	Example IceCube Stability Plots . . . . .	89
5.5	Neutrino Spectra . . . . .	90
6.1	BDT Schematic . . . . .	105
7.1	DeltaAngle . . . . .	112
7.2	Level 3 Quality Parameters . . . . .	116
7.3	BDT Performance . . . . .	117
7.4	RatioBDT . . . . .	117
7.5	BackgroundPDF . . . . .	119
7.6	TimePDF . . . . .	120
7.7	EnergyPDF . . . . .	122
7.8	TestStatistic . . . . .	124
7.9	OptimizeDiscovery . . . . .	125
7.10	FluxNeededFor5Sigma . . . . .	125
7.11	Limit . . . . .	126
7.12	Fraction . . . . .	127
7.13	Statistical Plane . . . . .	128
7.14	SeasonalVariation . . . . .	132

7.15	Final Limit . . . . .	134
7.16	Combined Limit . . . . .	135
8.1	GammaRangeLimit . . . . .	138
8.2	TvarRangeLimit . . . . .	140
8.3	ExclusionRegion . . . . .	142
8.4	IC80 Exclusion Region for 10 Years of operation . . . . .	143
8.5	IC80 Worst Case Exclusion Region for 10 years of operation . . . . .	144

## List of Abbreviations

ATWD	Analog Transient Waveform Digitizers
BAT	Burst Alert Telescope
BATSE	Burst and Transient Source Experiment
BDT	Boosted Decision Tree
BGO	Bismuth Germanate
CUDA	Compute Unified Device Architecture
CTEQ	The Coordinated Theoretical-Experimental Project on QCD
DAQ	Data Acquisition System
DOM	Digital Optical Modules
DOR	DOM Readout
fADC	Fast Analog Digital Converter
FPGA	Field Programmable Gate Array
FoV	Field of View
GRID	Gamma-Ray Imaging Detector
GBM	GLAST Burst Monitor
GCN	Gamma Ray Burst Coordinate Network
GLAST	The Gamma Ray Large Area Space Telescope
GRB	Gamma-ray Burst
HV	High Voltage
IBIS	On Board Imager
IC	IceCube
IC40	The 40 string IceCube Configuration
IC59	The 59 string IceCube Configuration
INTEGRAL	International Gamma-Ray Astrophysics Laboratory
IPN3	Third Interplanetary Network
LAT	Large Area Telescope
LSB	Long Soft Burst
LLH	Log-Likelihood
Ldir	Length of the event parameter
MMC	Muon Monte-Carlo
MPE	Multiple Photo-Electrons
NaI	Sodium Iodide
Ndir	Number of direct hits
PDF	Probability Density Function
PE	Photo-Electron
PMT	Photo-Multiplier Tube
PnF	Processing and Filtering
RAPCal	Reciprocal Active Pulsing
rlogl	Reduced Log-Likelihood
SHB	Long Hard Burst
SPE	Single Photo-Electron
SPADE	South Pole Archival and Data Exchange
SPICE	South Pole Ice

TMVA    Toolkit for Multivariate Data Analysis with ROOT  
UHECR   Ultra High Energy Cosmic Rays  
UVOT    Ultraviolet and Optical Telescope  
XRT    X-ray Telescope

## Chapter 1

### Introduction

Gamma-Ray Bursts (GRBs) are brief flashes of gamma rays in the keV – MeV energy range that occur a few times per day. Even though new satellite observations and complementary ground based observations have helped with our understanding of GRBs, many open questions remain. Discovering neutrinos associated with a GRB would improve our understanding of the processes that go on inside a GRB. Furthermore it would be a major step forward in our understanding of the extragalactic universe. GRBs are believed to be a prime candidate for the production of Ultra High Energy Cosmic Rays (UHECRs) [1]. UHECRs are Cosmic rays that have energy  $\sim 10^{14}\text{eV} - 10^{19}\text{eV}$  and are believed to be of extra galactic origin. GRBs are one of the few objects that are energetic enough to produce such high energy cosmic rays [1]. The problem with this theory is that it cannot be verified directly, because cosmic rays are deflected by the Universe's magnetic fields and hence they do not point back to the source when they arrive here on Earth. Neutrinos on the other hand are not deflected by magnetic fields and hence point back to their source. It is believed that protons are present in the GRB fireball; however, those protons cannot escape the strong magnetic fields in the fireball. In order for protons to be able to escape they first have to interact with photons in a  $p\gamma$  interaction to produce a  $\Delta$ -baryon, which then decays into a pion and a nucleon (proton or neutron). The

pion further decays to a neutrino, which results in an observable neutrino flux here on Earth, while neutrons escape the strong magnetic fields near the source and then decay to a proton. This proton would be outside of the magnetic confinement of the source and would contribute to the cosmic ray flux seen on Earth [1, 2, 3]. Because both the cosmic rays and neutrinos are produced in the same reaction the cosmic ray flux is strongly coupled to the neutrino flux and the detection of neutrinos would be strong evidence for GRBs to be a source of cosmic rays.

IceCube is the largest neutrino detector in the world and is in a unique place to search for neutrino emission from GRBs with sufficient instrumented volume to be sensitive to the predicted neutrino flux. The best previous limit has been achieved with IceCube in the 40-string configuration and was set at 0.82 times [4] the theoretically predicted flux from [3]. The analysis presented in this thesis used IceCube in the 59-string configuration and after seeing a null result was able to set a neutrino flux limit of 0.46 times the expected theoretical flux. The limits from this search and the previous search were then combined to form a single limit of 0.22 times the theoretical flux. This limit confidently excludes the current theoretical model; however there are some standard values that are used in the calculation that are not measured for GRBs and hence the uncertainty in the prediction is large. In Chapter 8.1 we examine what the current limit can say about those model parameters.

The search method used in this analysis is an un-binned log likelihood (LLH) method applied to the time window around a GRB. A Boosted Decision Tree (BDT) is introduced as a way to separate signal from background events. The LLH method allows us to avoid strict angular cuts and reduces the likelihood of seeing a false positive.

Moreover, it takes into account the spectral differences in signal and background.

This Thesis is organized as follows:

- Chapter 2 describes the history of GRB observations and describes the leading theoretical model for gamma-ray emissions from GRBs. Furthermore the parameters that are needed for a neutrino flux calculation are described and the neutrino flux calculation is presented.
- Chapter 3 describes the IceCube detector, including the underlying principles that make the detector work as well as the technology used to build an instrument necessary to do an analysis of astrophysical importance. The simulation, of events will be covered in this section as well.
- Chapter 4 continues the discussion of IceCube with a focus on event reconstruction techniques used in the analysis. Background reduction techniques are described as well.
- Chapter 5 describes the satellites that provide the gamma-ray information for the GRBs used in the analysis. Included in this chapter are detailed tables showing the GRBs used in this analysis.
- Chapter 6 describes high level analysis techniques used in this Thesis, including Boosted Decision Trees and the LogLikelihood method.
- Chapter 7 describes the analysis that was done to search for neutrino emission from GRBs. This includes the method, the optimization and finally the result.

- Chapter 8 concludes this thesis with a discussion on the implication of this the results presented in this thesis. Moreover, the expectations from future searches in IceCube is presented.
- Chapter 9 gives a brief outlook of what is to come in the future.
- Appendix A gives an account of shock acceleration. This includes first and second order Fermi acceleration as well as brief description of the physical processes that lead to cosmic rays.
- Appendix B outlines two methods on how to combine two limits set by independent analyses. Both methods were applied to combine the 40-string and 59-string result in Chapter 7.

## Chapter 2

### Gamma-ray Bursts

Gamma-ray Bursts (GRBs) are short and intense bursts of gamma rays observed in the 100KeV-1MeV energy band [2]. GRBs are observed about once a day, are isotropically distributed in the sky and are able to outshine everything else in the gamma-ray sky. The  $\gamma$ -ray energy a GRB releases in a few seconds is comparable to the energy the entire Milky Way Galaxy puts out in a few years. The astrophysical mechanisms at work in these objects is not yet understood and a neutrino flux discovery would play an important role in our understanding of these objects.

#### 2.1 History

The discovery of GRBs happened accidentally in the late 1960's. The Vela satellites were launched with the mission to monitor the "Outer Space Treaty", which forbade nuclear explosions in space. The satellites never discovered a violation of the treaty; however, they discovered GRBs for the first time. It was determined that the gamma-rays did not originate from Earth, and hence were not caused by humans, but it still took a few years to declassify the data. In 1973 the discovery of GRBs was announced and confirmed by Russian observations with the IMP-6 satellite [5]. Several theories were developed to explain the origin of GRBs and

# 2704 BATSE Gamma-Ray Bursts

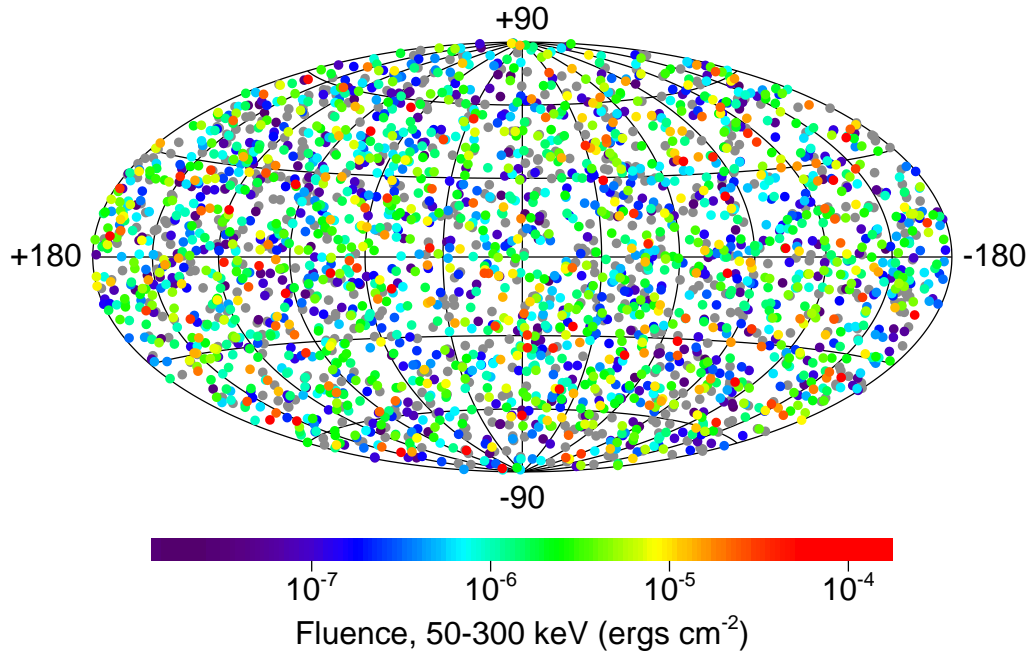


Figure 2.1: The distribution of BATSE burst in the sky. The distribution is isotropic and not centered in the galactic plane as earlier theories postulated and therefore GRBs are of extra galactic origin [7].

by the mid 1980's the claim of observing cyclotron spectral lines and the discovery of optical counterparts led to the belief that GRBs were of galactic origin [5, 6]. The belief was that neutron stars in the Milky Way Galaxy were the driving force behind GRBs. This theory was widely accepted and was not challenged until 1991 with the launch of the BATSE (Burst Transient Source Experiment) detector on the Compton Gamma Ray Observatory (CGRO) [7]. BATSE was sensitive to gamma-rays in the 15KeV-2MeV energy range and was able to observe 2704 GRBs through 2004. The observed GRBs are distributed isotropically in the sky (figure 2.1), which strongly disfavored any galactic origin model [8].

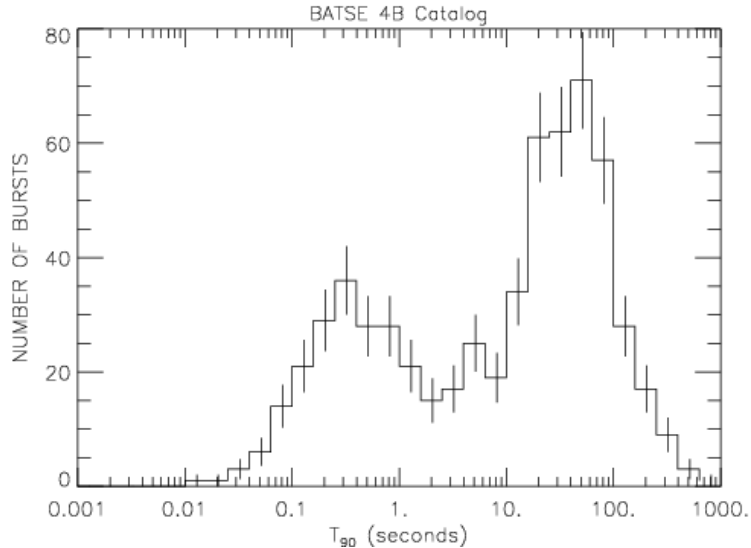


Figure 2.2: This plot shows the duration of all of the BATSE bursts. There is clearly a double peak that distinguishes GRBs into 2 categories [7].

Another BATSE result was that the GRB population could be split into two categories. The 2 categories are: Long and Short GRBs. Long GRBs are defined as GRBs that last longer than 2 seconds with short GRBs lasting less than 2 seconds. 90% of observed GRBs during the IceCube 59-string run are long GRBs. The BATSE length distribution can be seen in, figure 2.2 clearly showing that there are two separate GRB populations.

In 1996 the Beppo SAX satellite was launched, which opened up a new observation channel: X-Rays [9]. In February of 1997 Beppo SAX detected a GRB (GRB 970228), and when the x-ray camera was pointed towards the direction of the GRB, a fading afterglow in x-rays was observed [10, 11]. Later, ground based optical telescopes were also able to detect an optical afterglow, and after the GRB had faded completely, a faint distant galaxy was found at the location of the GRB. This was

additional proof that GRBs are an extra-galactic phenomenon. The red shift for this first observation was never determined. However, Beppo SAX found other GRBs for which the redshift was determined (see [12]). All of those measurements placed GRBs in distant galaxies. In 2000, the High Energy Transient Explorer (HETE-2) was launched and with the prime objective of carrying out multi-wavelength observations of GRBs [13]. HETE-2 was able to localize the position of GRBs to within arc-seconds using its wide field X-ray monitor (WXM) [13] and transfer that information to the ground within seconds of detecting a GRB. This enabled almost instantaneous ground based follow up observations in optical and radio. Some of the major achievements of HETE-2 was the discovery of nearby GRB 030329, which firmly connected GRBs with supernovas [14]. HETE-2 was also able to observe the first short/hard GRB (GRB 050709) with an optical counterpart [15]. The Swift satellite was launched in 2004 and combined a gamma-ray detector with X-ray, optical and UV follow up detectors [16]. Swift has the ability to quickly (within one minute of a gamma-ray detection) slew to the direction of a gamma-ray detection and point its follow up detectors in the direction of detected gamma-rays. This quick response to a GRB enables Swift to observe both the energetic prompt emission and the softer afterglow, as well as observe short burst afterglows on a consistent basis. Swift is also well suited for an IceCube GRB search because the uncertainty of the GRB location is usually much smaller than the directional uncertainty of IceCube.

The most recent gamma-ray mission is the Fermi Gamma-ray Space Telescope [17], which was launched in June 2008. The advantage of Fermi over previous missions is that the on-board Gamma-ray Burst Monitor (GBM) is sensitive to

GRBs, from anywhere in the sky that is not blocked by Earth or the moon. This all sky coverage comes at the expense of getting a precise measurement of the GRB location. For many Fermi GRBs, the directional uncertainty is of the same order as the directional uncertainty of reconstructed neutrinos in IceCube, which makes an analysis more complicated, however, since Fermi is able to detect many more bursts than Swift, it is still advantageous to consider the Fermi bursts in addition to Swift bursts. More information on the satellites used in this analysis as well as information on the specific GRBs used is found in Chapter 5.

## 2.2 Theory

### 2.2.1 Introduction

The extra-galactic nature of GRBs makes it difficult to identify the progenitors, however, the extra-galactic nature of GRBs is also convincing evidence that a GRB must be associated with the cataclysmic explosion of stellar mass objects. As mentioned above, the GRB population is split into two populations; long and short bursts. It is believed that long bursts are associated with the collapse of a massive star. This connection can be made because many of the observed long GRBs happen in rapidly star-forming galaxies and are sometimes associated with core collapse supernovae [14]. Less data is available for short GRBs and no afterglows were observed until 2005 [15]. Since 2005  $\sim 100$  short GRB afterglows have been observed and it was found that short GRBs happen in galaxies that have little or no star formation at all, and hence it is believed that short GRBs are not associated with

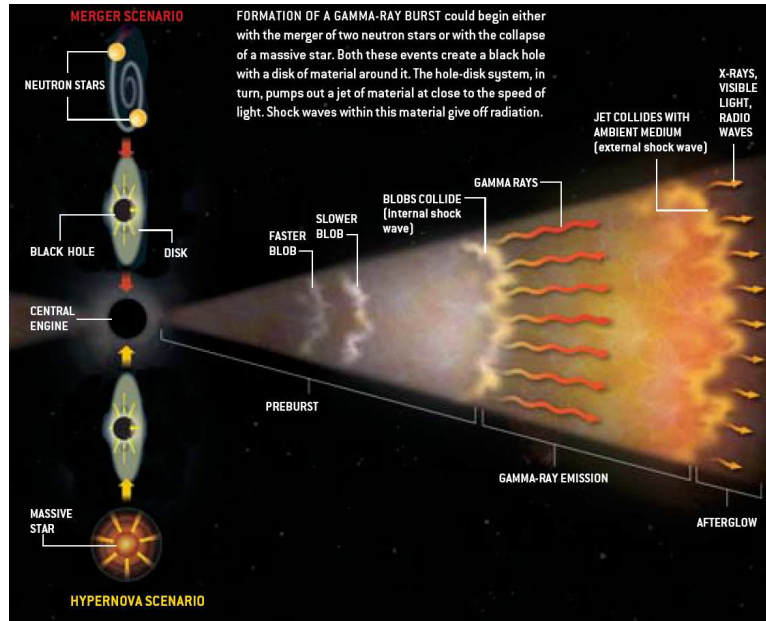


Figure 2.3: This figure shows a cartoon characterization of the GRB fireball model. Both progenitor scenarios are shown as well as the different stages of the GRB fireball [7].

the core collapse of a massive star [18]. The leading theory explaining short GRBs involves the merger of two compact objects. In both cases the released energy comes from the release of gravitational energy and the accretion of gas onto the central compact object, which is described by the fireball model [19]. A cartoon schematic of the fireball model is shown in figure 2.3.

### 2.2.2 The Fireball Model

The fireball model assumes a cataclysmic energy release in stellar mass objects from the release of gravitational energy. Accretion onto the central object further adds to the total energy released in the event. Material along the rotational axis falls in faster than material near the equator because of centripetal acceleration,

which results in a accretion disc surrounding the central object. The infall of material causes an inward pressure near the poles which is counteracted by an outward pressure from the stellar object. Once the outward pressure overcomes the inward pressure an explosion occurs near the poles that expands in the form of a collimated jet. A fraction of the total energy of this explosion is trapped in a  $e^+$ ,  $e^-$ , and  $\gamma$  fireball. This fireball is highly relativistic because of the low energy contribution of Baryons to the total energy of the fireball ( $M_B c^2 \ll E$  with  $M_B$  being the total mass of baryons and  $E$  is the total energy of the fireball). It is theorized that the baryons present in the fireball are protons that get accelerated along with the electrons. It is not clear that protons are necessary in this process, however, if present they would directly contribute to the neutrino emission described in the following sections and hence a neutrino observation would answer this question. This acceleration would also explain the source of UHECRs [1].

The observed prompt  $\gamma$ -ray spectrum is a broken power law with great variability in the spectrum. This implies that the radiation observed is not caused by a smoothly expanding fireball radiating thermally. The randomness observed can be achieved by having internal and external shocks reconvert the thermal energy of the expanding fireball into random kinetic energy [20] [21]. It is believed that during these internal shocks charged particles are accelerated to ultra-high energies, with the electrons giving off prompt gamma-ray emission via synchrotron radiation (see Appendix A for an overview on shock acceleration) [22]. It is believed that external shocks are responsible for the GRB afterglow emissions that are seen.

The prompt GRB photon spectrum  $\frac{dN_\gamma}{dE_\gamma}(E_\gamma)$  can be modeled by the Band function

as follows [23]:

$$\frac{dN_\gamma}{dE_\gamma}(E_\gamma) = A \begin{cases} \left(\frac{E_\gamma}{100\text{keV}}\right)^{-\alpha_\gamma} e^{(-E_\gamma/E_0)} & E_\gamma \leq \epsilon_\gamma^b \\ \left(\frac{E_\gamma}{100\text{keV}}\right)^{-\beta_\gamma} \left[\frac{(\beta_\gamma - \alpha_\gamma)E_0}{100\text{keV}}\right]^{\beta_\gamma - \alpha_\gamma} e^{-(\beta_\gamma - \alpha_\gamma)} & E_\gamma > \epsilon_\gamma^b \end{cases} \quad (2.1)$$

Where,  $E_\gamma$  is the photon energy,  $E_0$  is the reference energy and  $\epsilon_\gamma^b = (\beta_\gamma - \alpha_\gamma) \cdot E_0$  is the break energy of the photon spectrum.  $\alpha_\gamma$  is the spectral index of the gamma spectrum before the break in the energy spectrum, while  $\beta_\gamma$  is the spectral index after the break. The broken power law of the gamma spectrum is shown in figure 2.4. The typical break energy is  $\epsilon_\gamma^b \sim 250\text{keV}$  and the softening of the spectrum is generally explained in one of two ways.:

The most common explanation is that the softening of the spectrum by one power is caused by inherent cooling of electrons at high energies through synchrotron radiation [2, 23].

The second common explanation is that the spectrum softens because of inverse Compton scattering in the fireball reducing the number of high energy  $\gamma$ -rays present at the source [24].

For the GRBs in the IC59 sample  $\alpha_\gamma \sim 1$  and  $\beta_\gamma \sim 2$  are the approximate average values. These values are scattered over a wide range due to the variability in individual GRBs. It is worth noting that short GRBs tend to have harder spectra values with  $\alpha_\gamma \sim 0$  and  $\beta_\gamma \sim 1$ .

### 2.2.3 Neutrino Production in the Fireball

IceCube is designed to search for neutrino emission from astrophysical sources and therefore we focus on the model's neutrino production prediction in the analysis.

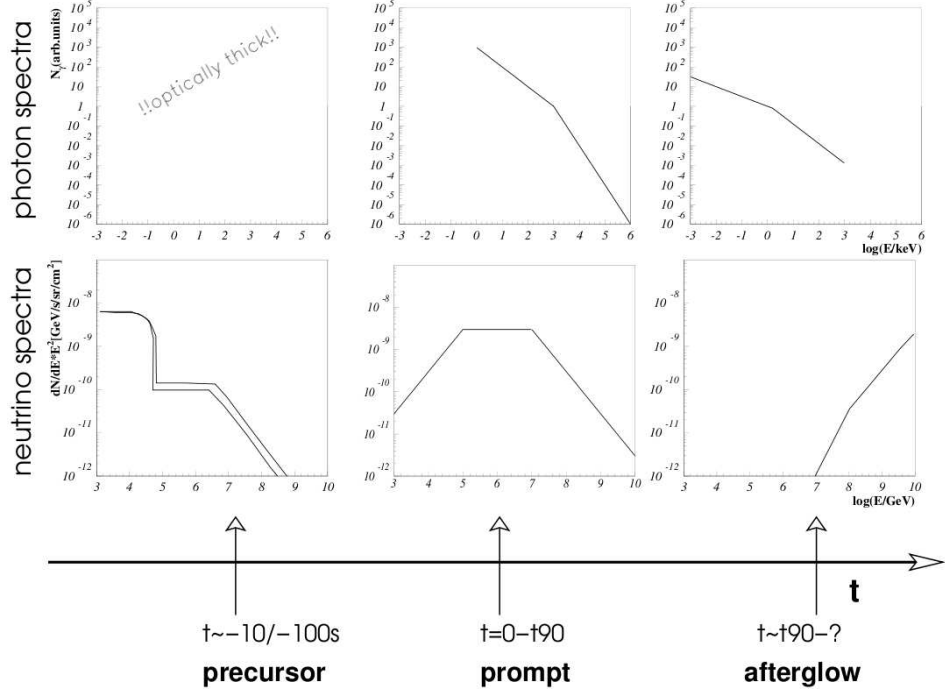


Figure 2.4: This plot shows typical light curves for  $\gamma$  and  $\nu$  emission for the precursor, prompt and afterglow phase. The analysis presented in this thesis focuses on neutrino emission from the prompt phase. Note the change in scale going from the  $\gamma$  plots to the  $\nu$  plots. Taken from [25].

This section will cover the production of neutrinos in the interaction of protons and photons. The information found in this section is predominantly found in [3]. Figure 2.4 shows the  $\gamma$ -ray spectrum and the neutrino spectra for a typical GRB. The calculation to obtain the neutrino spectrum is presented in this section.

Protons predominantly produce the parent pions that are needed for neutrino production via the process:

$$p\gamma \rightarrow \Delta \rightarrow n\pi^+ \quad (2.2)$$

and

$$p\gamma \rightarrow \Delta \rightarrow p\pi^0 \quad (2.3)$$

which have large cross sections of  $\sigma_{\Delta} \sim 5 \times 10^{-28} \text{cm}^2$  if enough center of mass energy is present to produce a  $\Delta$  (see equation 2.4). The charged pions from equation 2.2 decay into charged leptons and neutrinos while the  $\pi^0$  will decay into photons. The magnetic fields in the fireball are too strong for protons to escape and hence, if GRBs are indeed a source of cosmic rays, they would originate from the  $\Delta$  decay to a neutron and a charged pion. The neutron would be able to escape the magnetic fields and would decay back to a proton outside the fireball, which would be responsible for the cosmic rays observed on Earth. The  $\pi^+$  decay from the same reaction would produce the neutrinos, and hence cosmic ray production is strongly coupled to neutrino production. Moreover, photons are produced when the  $\pi^0$  decays, which couples the photons observed here on Earth to the cosmic ray and neutrino production in this model [2]. Therefore it is possible to normalize the expected neutrino flux to the observed gamma ray flux (this is done later in this chapter) [3].

In order for the photon-proton interaction to produce a  $\Delta$ , enough energy needs to be present in the particles. This is known as the  $\Delta$ -resonance [26], and in the co-moving frame the proton energy must meet this condition:

$$\epsilon'_p \geq \frac{m_{\Delta}^2 - m_p^2}{4\epsilon'_{\gamma}} \quad (2.4)$$

which corresponds to an energy of:

$$\epsilon_p \geq 1.4 \times 10^{16} \frac{\Gamma_{2.5}^2}{\epsilon_{\gamma, \text{MeV}}} \text{eV} \quad (2.5)$$

in the observer frame. Here primed values refer to values in the co-moving frame while un-primed quantities are in the observer frame. This produces a neutrino

energy of:

$$\epsilon_\nu = \frac{1}{4} \langle x_{p \rightarrow \pi} \rangle \epsilon_p \geq 7 \times 10^{14} \frac{\Gamma_{2.5}^2}{\epsilon_{\gamma, \text{MeV}}} eV \quad (2.6)$$

Here the photon energy is  $\epsilon_{\gamma, \text{MeV}} = \epsilon_\gamma / \text{MeV}$  and the bulk Lorentz factor is  $\Gamma_{2.5} = \Gamma / 10^{2.5}$ .  $\langle x_{p \rightarrow \pi} \rangle \simeq 0.2$  is the average fraction of energy that is transferred from the initial proton to the pion [27]. The factor of  $\frac{1}{4}$  comes from the fact that there are 4 final leptons produced each carrying an equal amount of energy ( $\pi^+ \rightarrow \nu_\mu \mu^+ \rightarrow \nu_\mu e^+ \nu_e \bar{\nu}_\mu$ ). These are all approximations but considering the large uncertainties that are inherit in modelling astrophysical phenomenon, these are adequate approximations.

In order for a  $\Delta$ -baryon to be produced, the center of mass energy of the  $p\gamma$  system must be larger than the  $\Delta$  rest mass. This implies that the photon and neutrino energy are inversely proportional,  $E_\nu \propto E_\gamma^{-1}$  and therefore the resulting neutrino spectrum traces the broken power law spectrum covered in section 2.2.2 [27]. Therefore:

$$F_\nu = \epsilon_\gamma \frac{dn_\gamma}{d\epsilon_\gamma} \propto \begin{cases} \epsilon_\gamma^{-\alpha_\nu} & \epsilon_\gamma < \epsilon_\nu^b \\ \epsilon_\gamma^{-\beta_\nu} & \epsilon_\gamma > \epsilon_\nu^b \end{cases} \quad (2.7)$$

Using the photon indices  $\alpha_\nu = 3 - \beta_\gamma$  and  $\beta_\nu = 3 - \alpha_\gamma$  can be calculated. Furthermore using equation 2.4 and  $E_\nu = \frac{1}{4} \langle x_{p \rightarrow \pi} \rangle E_p$  the first break energy can be found:

$$\epsilon_\nu^b = \frac{(m_\Delta^2 - m_p^2) \cdot \Gamma^2}{4 \cdot (1+z)^2 \cdot \epsilon_\gamma^b} = 7.5 \times 10^5 \text{GeV} \frac{1}{(1+z)^2} \left( \frac{\Gamma}{10^{2.5}} \right)^2 \left( \frac{\text{MeV}}{\epsilon_\gamma^b} \right) \quad (2.8)$$

Here an explicit dependence on redshift,  $z$ , has been introduced. It is important to note that the highest energy pions may lose energy due to synchrotron emission before decaying. This will reduce the energy of the resulting secondary particles

and hence final neutrino energy spectrum will steepen at higher energies. The effect becomes important when the pion lifetime and the synchrotron loss time become comparable:

$$\tau'_\pi \approx \frac{2.6 \times 10^{-8} \epsilon'_\pi}{m_\pi c^2} = t'_{sync} = \frac{3m_\pi^4 c^3}{4\sigma_T m_e^2 \epsilon_p i U'_B} \quad (2.9)$$

Where  $U'_B = \frac{B'^2}{8\pi}$  is the energy density in the magnetic field of the shocked plasma. The fraction of the internal energy carried by the magnetic field,  $\epsilon_B$ , can be defined as follows:

$$4\pi R^2 c \Gamma^2 B'^2 / (8\pi) = \epsilon_B L_{int} \quad (2.10)$$

with  $R \sim 2\Gamma^2 ct_v$  being the collision radius of different shells ( $t_v$  is the time difference between the emitted shells). This collision radius arises from the belief that different shock waves have velocities that differ by,  $\delta v \sim c/2\Gamma^2$ , where  $\Gamma$  is the average Lorentz factor for the entire fireball. Therefore different shells emitted at different times collide after time  $t_c \sim ct_v/\delta v$ , which corresponds to the above radius. This calculation is worked out in more detail in [28]. Comparing the pion life time to the synchrotron loss time yields:

$$\frac{t'_{sync}}{\tau'_\pi} = 0.21 \epsilon_e \epsilon_B^{-1} L_{52}^{-1} \Gamma_{2.5}^8 t_{\nu,-2}^2 \epsilon_{\pi 18}^{-2} \quad (2.11)$$

Where  $\epsilon_2$  is the fraction of internal energy converted to electrons  $L_{\gamma,52} = L_\gamma/10^{52} \text{ erg/s}$  is the  $\gamma$ -ray luminosity of the GRB,  $t_{\nu,-2} = t_\nu/10^{-2} \text{ s}$  is the GRB lightcurve time scale fluctuation time and  $\epsilon_{\pi 18} = \epsilon_\pi/10^{18} \text{ eV}$  is the pion energy. Above it was mentioned that synchrotron radiation losses become important when the synchrotron time scale is comparable to the lifetime of the pion,  $t'_{sync} \leq \tau'_\pi$ . This corresponds to

$\epsilon_\pi \leq \epsilon_{\pi s} \approx 4\epsilon_{\nu s}$  with:

$$\epsilon_{\nu_\mu}^s = \frac{10^{17}}{1+z} \epsilon_e^{1/2} \epsilon_B^{-1/2} L_{\gamma,52}^{-1/2} \Gamma_{2.5}^4 t_{t,-2} eV \quad (2.12)$$

Muons have a lifetime that is 100 times larger than that of pions, and therefore neutrinos produced from muon decay have a cutoff energy that is 10 times larger than neutrinos produced from pion decay [3].

$$\epsilon_{\nu_\mu, \nu_e}^s = \frac{10^{16}}{1+z} \epsilon_e^{1/2} \epsilon_B^{-1/2} L_{\gamma,52}^{-1/2} \Gamma_{2.5}^4 t_{t,-2} eV \quad (2.13)$$

Above this energy the spectrum hardens by 2 ( $\beta + 2$ ).

The resulting neutrino spectrum needs to be normalized to the gamma-ray fluence  $F_\gamma$ , which is assumed to be proportional to the neutrino fluence. A detailed account of this calculation is given in Appendix A of [3]. The last step of this calculation is to integrate the neutrino spectrum and set it equal to the integral of the gamma ray spectrum. This yields:

$$\int_0^\infty dE_\nu F_\nu(E_\nu) = \frac{1}{8} \frac{1}{f_e} \left(1 - (1 - \langle x_{p \rightarrow \pi} \rangle)^{N_{int}}\right) \int_0^\infty dE_\gamma F_\gamma(E_\gamma) \quad (2.14)$$

here

$$N_{int} = \left( \frac{L_\gamma^{iso}}{10^{52} \text{erg s}^{-1}} \right) \left( \frac{0.01s}{t_{var}} \right) \left( \frac{10^{2.5}}{\Gamma} \right)^4 \left( \frac{MeV}{\epsilon_\gamma^b} \right) \quad (2.15)$$

Here the factor of  $\frac{1}{8}$  accounts for the fact that half of the photon-hadronic interactions result in four leptons.  $f_e$  is the fraction of fireball energy that is carried in electrons rather than protons and hence the fraction of energy that does not participate in neutrino production.  $\left(1 - (1 - \langle x_{p \rightarrow \pi} \rangle)^{N_{int}}\right)$  represents the fraction of energy that is transferred to pions.

Now combining all of the above results the neutrino spectrum can be calculated:

$$\epsilon_\nu^2 \frac{dN_\nu}{d\epsilon_\nu} \approx \frac{1}{8} \frac{1}{\epsilon_e} \frac{F_\gamma}{\ln(10)} \frac{1}{f_e} \frac{L_{\gamma,52}}{\Gamma_{2.5}^4 t_{\nu,-2} \epsilon_{\gamma,MeV}^b} \begin{cases} \left(\frac{\epsilon_\nu}{\epsilon_\nu^b}\right)^\beta & \epsilon_\nu < \epsilon_\nu^b \\ \left(\frac{\epsilon_\nu}{\epsilon_\nu^b}\right)^\alpha & \epsilon_\nu^b < \epsilon_\nu < \epsilon_\nu^s \\ \left(\frac{\epsilon_\nu}{\epsilon_\nu^b}\right)^\alpha \left(\frac{\epsilon_\nu}{\epsilon_\nu^s}\right)^{-2} & \epsilon_\nu > \epsilon_\nu^s \end{cases} \quad (2.16)$$

Here  $\epsilon_\nu^b$  and  $\epsilon_\nu^s$  are given by equations 2.8, 2.12 and 2.13. Using this equation the neutrino spectrum for the GRBs present in this analysis can be calculated and plotted (shown in Figure 5.5). In table 5.4, the neutrino spectrum is given for the GRBs used in this thesis, while table 5.2 gives the average parameters used in this calculation. For more more information on the GRBs used in this analysis, see Chapter 5.

### 2.2.3.1 The Bulk Lorentz factor $\Gamma$

Because the Bulk Lorentz factor  $\Gamma$  is important in the overall normalization as well as in determining the break energies it is worth outlining how it is calculated. An estimate of the  $\Gamma$  factor can be made by assuming that in a fireball that produces as much energy as a GRB, pair production of  $e^+e^-$  in the  $\gamma$  fireball must be present [29]. The fact that photons with energy  $> 10GeV$  have been observed means that these photons survived pair production, which constrains  $\Gamma$  values to [3, 30]:

$$\Gamma \sim 250 \left[ L_{\gamma,52} t_{v,-2}^{-1} \left( \frac{\epsilon_{\gamma,max}}{100MeV} \right) \right]^{1/6} \quad (2.17)$$

Here a default value of  $100MeV$  was chosen even though some GRBs have higher recorded photon energies. It is worth noting that the bulk Lorentz factor is weakly dependent on luminosity, time structure and the maximum  $\gamma$ -energy. In this analysis

a  $\Gamma = 316$  is assumed in the neutrino spectrum calculations (this value was also used previously for an IceCube analysis [31]).

## Chapter 3

### IceCube

Neutrinos only interact weakly and hence are difficult to detect. However, because they only interact weakly, it also makes them the ideal cosmological messenger particles since they do not get absorbed on their journey to Earth and will point back to their source because they are unaffected by magnetic fields. It is postulated that in order to detect cosmological neutrino sources, a kilometer scale detector is needed [32]. This was the motivation for constructing the IceCube detector at the South Pole [33] [34].

The IceCube neutrino detector finished construction in December of 2010. It consists of 5160 photomultiplier tubes that instrument one cubic kilometer of South Pole ice. The photomultiplier tubes are able to detect Cherenkov light [35], produced by charged particles that pass through the instrumented volume. Neutrinos interacting near or in the detector will produce secondary charged particles through a charged current interaction with a nucleon. The secondary charged particles produce Cherenkov light and are thereby detected in IceCube. The pattern and timing information of the detected light can then be used to reconstruct the direction of the charged particle and hence the neutrino. IceCube is the largest detector of its kind and allows an unprecedented look at the neutrino sky. Figure 3.1 shows a visual representation of IceCube, giving a sense of scale.

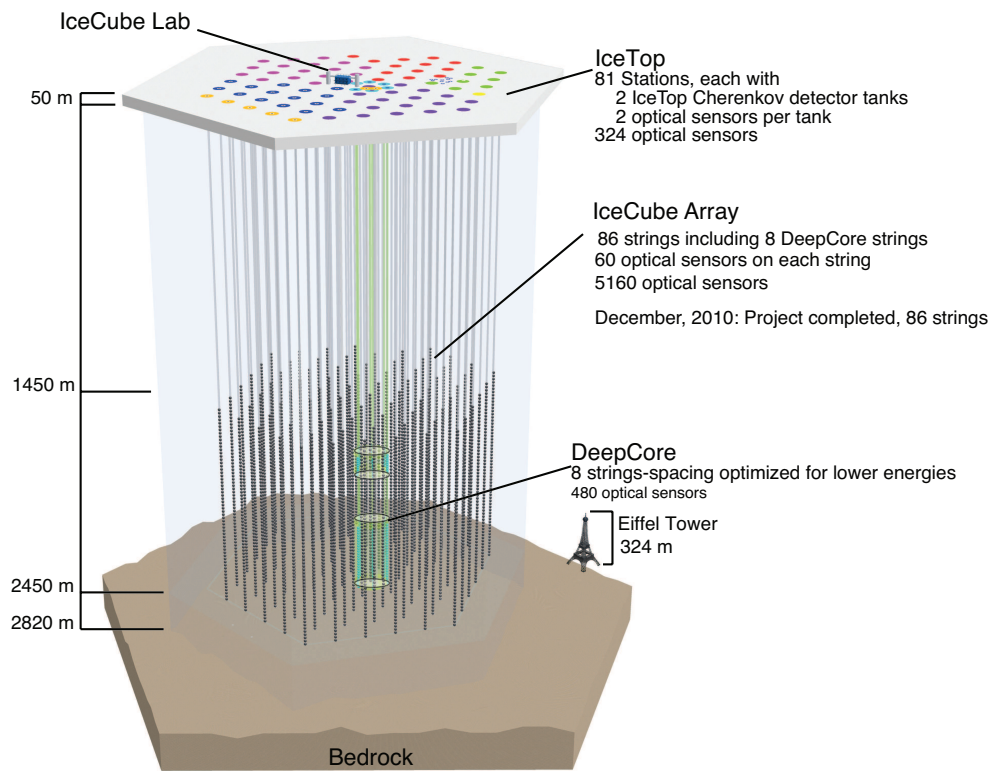


Figure 3.1: This schematic shows the IceCube detector constructed deep underneath the South Pole ice. For scale the Eiffel Tower is shown.

## 3.1 Detection Principle

As mentioned above IceCube cannot directly detect neutrinos. It relies on Cherenkov light that is produced by secondary particles. IceCube is optimized for detection of muons and hence muon neutrinos. There is some sensitivity to other neutrino flavors as well, although this analysis will focus on muon neutrinos. The strategy to detect neutrinos is to instrument a large, clear, and dark volume with light sensitive modules. IceCube has found such a volume in the Antarctic ice near the South Pole. IceCube was designed to be sensitive to neutrinos with energies  $> 1$  TeV.

### 3.1.1 Neutrino Interaction

This analysis will focus on the detection of muons that are produced by incident muon neutrinos. The process by which secondary muons are produced is called a charged current interaction. In the standard model of particle physics, there exists a three body vertex linking a  $\nu_\mu$ , a  $\mu$  and a  $W^\pm$  and a three body vertex involving a  $W^\pm$  that changes a u quark to a d quark or vice-versa. This makes it possible to write down the following reaction.

$$\nu_\mu + N \longrightarrow \mu + X, \tag{3.1}$$

Another important reaction is the neutral current interaction. In that case, a  $Z_0$  interacts with a quark resulting in the neutrino losing energy. This reaction is important since neutrinos moving through earth can lose energy in that manner. Figure 3.2 shows Feynman diagrams of both the neutral and the charged current

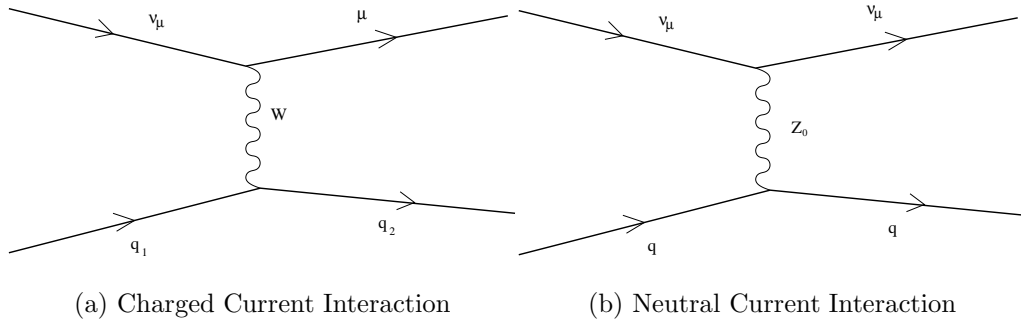


Figure 3.2: Feynman diagrams showing charged and neutral current interactions.

interaction. Both the charged and neutral current interaction cross-sections are energy dependent. The cross section increases with energy, so the highest energy neutrinos are attenuated the most by Earth. This effectively makes earth opaque for the highest energy neutrinos and IceCube is forced to look at the horizon to see the highest energy neutrinos. Figure 3.3 show the neutrino and antineutrino cross sections as a function of energy.

### 3.1.2 Muon Propagation

Following a charged current interaction, the secondary muon will move through the ice carrying a significant portion of the primary neutrino energy. The secondary muon will propagate through the ice and lose energy through ionization, pair production, bremsstrahlung and photo-nuclear interactions. As it turns out, we can write the energy loss of a muon moving through a medium as:

$$-\frac{dE}{dx} = a(E) + b(E)E \tag{3.2}$$

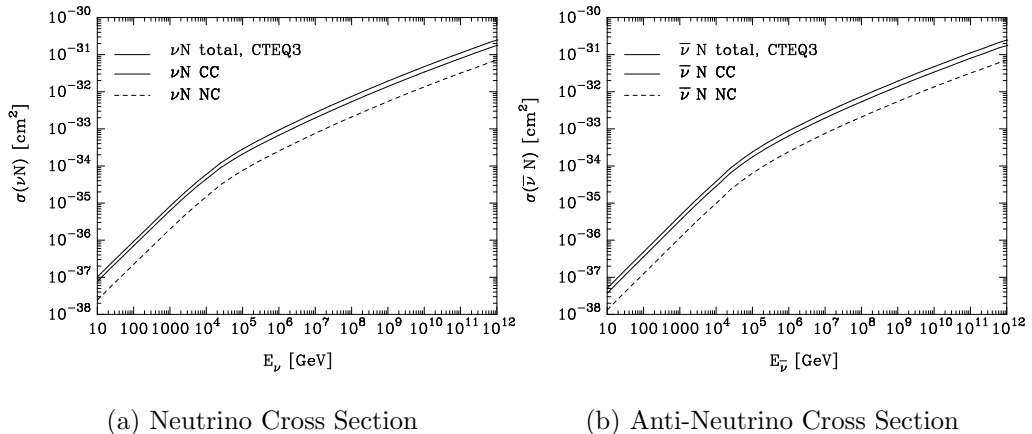


Figure 3.3: The neutrino-nucleon cross section as a function of neutrino energy  $E_\nu$ . The cross sections were calculated using the deep inelastic scattering model from CTEQ [36]. At low energies the neutrino cross sections are proportional to  $E_\nu$  however at higher energies,  $E_\nu \gg M_w^2/2M_N$ , the interactions is suppressed by the W-boson propagator and the cross section becomes proportional to  $\sim E^{0.36}$ . This plot is taken from [37]

In this equation the term  $a(E)$  represents the ionization energy loss and is known as the Bethe-Bloch equation [38]. The term  $b(E)$  is the sum of pair production, Bremsstrahlung, and photo nuclear contributions. Both of these functions are slowly varying at energies that are of interest in an IceCube analysis. Therefore we can make the approximation that both  $a(E)$  and  $b(E)$  are constant. If we further assume that the initial energy of the muon is  $E_0$  then we find that:

$$x \approx \frac{1}{b} \ln\left(1 + \frac{b}{a} E_0\right) \quad (3.3)$$

Here  $x$  is the total propagation length in meters. In order to have a sufficiently long track length for IceCube to be able to reconstruct a muon successfully, a threshold energy of 50GeV or higher is necessary. For energies higher than the threshold energy, muons that are produced outside of the detector volume will reach the

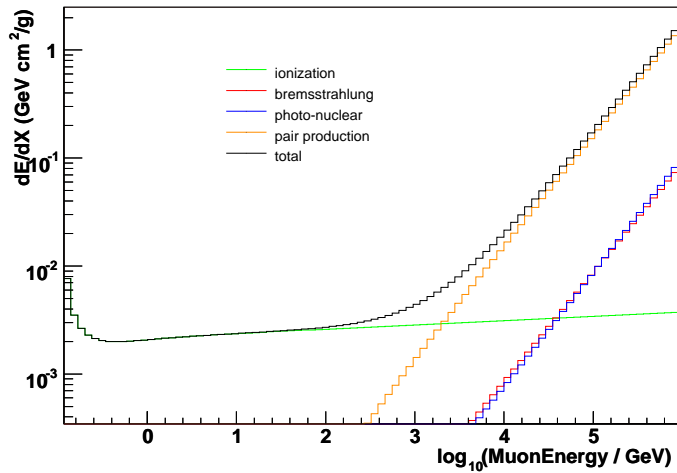


Figure 3.4: Muon Energy loss in a medium of similar density to Antarctic ice. Shown here are the most prominent energy losses. For energies above 100GeV the energy loss is dominated by stochastic energy losses. Obtained using MMC. [39]

detector, increasing the effective area. The muon energy loss is shown in Figure 3.4.

### 3.1.3 Detecting Muons

Once a muon is created with sufficient energy to move through the instrumented volume of IceCube, it still needs to be detected, and its direction reconstructed. In order to understand how this can be done it is useful to look at the Bethe-Bloch equation describing the muon energy loss due to ionization [38]:

$$-\frac{dE}{dX} = Kx^2 \frac{Z}{A} \frac{1}{\beta^2} \left[ \frac{1}{2} \ln \frac{2m_e c^2 \beta^2 \gamma^2 T_{max}}{I^2} s - \beta^2 - \frac{\delta}{2} \right] \quad (3.4)$$

Here  $E$  is the energy of the particles with  $X$  being the distance travelled.  $Z$  is the atomic number the absorbing material and  $A$  is the absorbing weight.  $m_e c^2$  is the rest mass energy of an electron,  $T_{max}$  is the maximum energy transfer and

$I$  is the mean excitation potential. The term in the Bethe-Bloch equation that is particularly important for IceCube is the density-correction term  $\frac{\delta}{2}$ . This term arises from the effective weakening of the muon field due to the polarization of the medium. This causes the energy loss to be decreased when the muon is traveling faster than the speed of light in the medium because this polarization adds coherently. This causes some of the radiation to escape at a fixed angle with respect to the muon's path. This effect is known as Cherenkov radiation and makes the type of neutrino astronomy done with IceCube possible. Cherenkov light is emitted at a constant angle given by  $\cos(\theta_C) = \frac{1}{n\beta}$ . Here  $n$  is the index of refraction of the medium and  $\beta$  is the speed of the particle in units of  $c$ . In ice this angle is  $\theta_C = 40.7^\circ$  for  $\beta = 1$ . A schematic of the Cherenkov light cone is shown in Figure 4.3.

## 3.2 The Ice

The Cherenkov radiation that is produced by the muon needs to propagate to the photo-multiplier tubes so that the muon direction can be reconstructed. The propagation of the photons produced by the muon is affected by the medium through which they move. In the case of the South Pole, ice there are dust layers that are the result of changing geological conditions over thousands of years. Today, these dust layers cause the optical properties of the ice to be depth dependent. There are two things that can happen to a photon as it moves through the ice before it gets to an optical module. First of all a photon can get absorbed, in which case it never reaches the optical module, or the photon can scatter. The absorption length

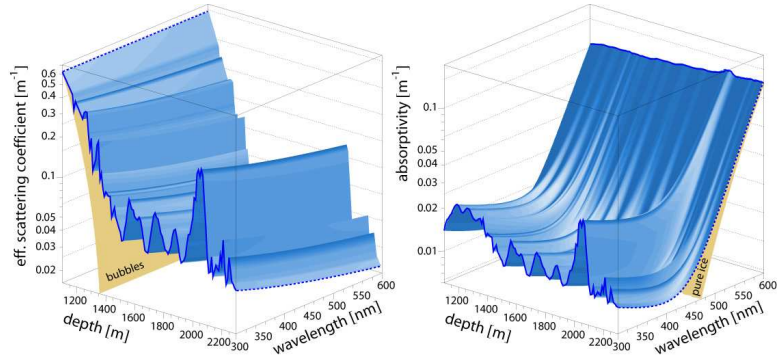


Figure 3.5: The left figure shows scattering length as a function of depth and wavelength while the right figure shows absorption length as a function of depth and wavelength. [40]

in ice is about 100m, which is similar to the string spacing but large compared to the DOM spacing on any given string. The scattering length, on the other hand, is only about 20m, and considering that the optical module spacing is 17m many of the photons that are detected are scattered before reaching an optical module. The most prominent feature in the South Pole ice is a dust layer at 2000m, which causes sharp peaks in both the absorption and scattering coefficients. This makes it difficult to detect light in that layer. The absorption length and scattering length as a function of depth and wavelength is shown in Figure 3.5. Both the simulation and reconstruction algorithms need to account for the fact that most of the observed photons have been scattered. It is therefore important to have a good understanding of the South Pole ice.

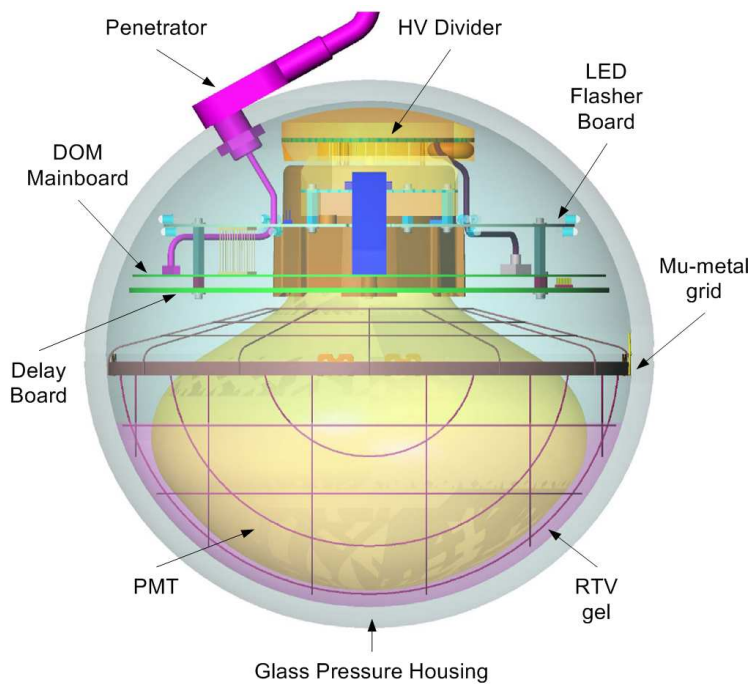


Figure 3.6: The IceCube DOM

### 3.3 The Optical Detectors

IceCube is an array of light-sensitive Digital Optical Modules (DOMs) buried in a cubic kilometer of ice below the geographic South Pole. In addition there is an above ground air-shower array designed to detect cosmic rays known as IceTop. In this thesis, only IceCube data was used and hence the focus here will be on IceCube.

Each DOM contains a 10-inch Photo-Multiplier tube (PMT) and the necessary electronics for collecting and digitizing voltage pulses from the PMT. Figure 3.6 shows a schematic of the DOM used in IceCube. The heart of the DOM is the PMT, which consists of a thin photo-cathode and a dynode chain. About 25% of the incident photons will interact with the cathode and because of the cathode's low

work function it will knock off a single electron. The knocked off electron is called a photo-electron (PE). There is a potential difference between the cathode and a series of dynodes, which causes the PE to be accelerated toward the first dynode where it knocks off more electrons. The subsequent dynodes are held at a progressively higher voltage and so the electrons knocked off from the first dynode get accelerated toward the the next dynode in the series, where the process repeats. Finally, the electrons reach the anode where they cause a sharp current pulse indicating the arrival of a photon. The gain of the the PMT is defined as the average number of electrons that are incident on the anode per photon, which is  $\sim 10^7$  for IceCube DOMs.

The PMTs used are manufactured by HAMAMATSU and are of the type R7081-02 with a 25cm diameter. The PMT has 10 dynodes and was chosen for its low dark noise rate of about 300Hz, with the actual noise rate of the deployed DOM being about 600Hz. Dark noise is caused by radioactive decays and thermal noise in the PMT. The rest of the noise comes from triboluminescence and light emitted by muons that are not associated with an event [41]. The peak quantum efficiency is reached at a light wavelength of  $\sim 400\text{nm}$ . In figure 3.7, the quantum efficiency of the IceCube DOM is shown as a function of wavelength. The Cherenkov spectrum for a particle moving through a medium is given by the Frank-Tamm formula 3.5 [42].

$$dE = \frac{\mu q^2}{4\pi} \omega \left( 1 - \frac{1}{\beta^2 n^2} \right) dx d\omega \quad (3.5)$$

Here  $\mu$  is the permeability and  $n$  is the index of refraction of the medium.  $q$  is the

electric charge of the particle moving through the medium, with  $\omega$  being the angular frequency of the Cherenkov radiation. The Cherenkov intensity is proportional to the frequency and hence falls off smoothly with larger wavelength. Figure 3.8 shows the Cherenkov light intensity as a function of wavelength in ice along with the sensitivity range for the IceCube PMT.

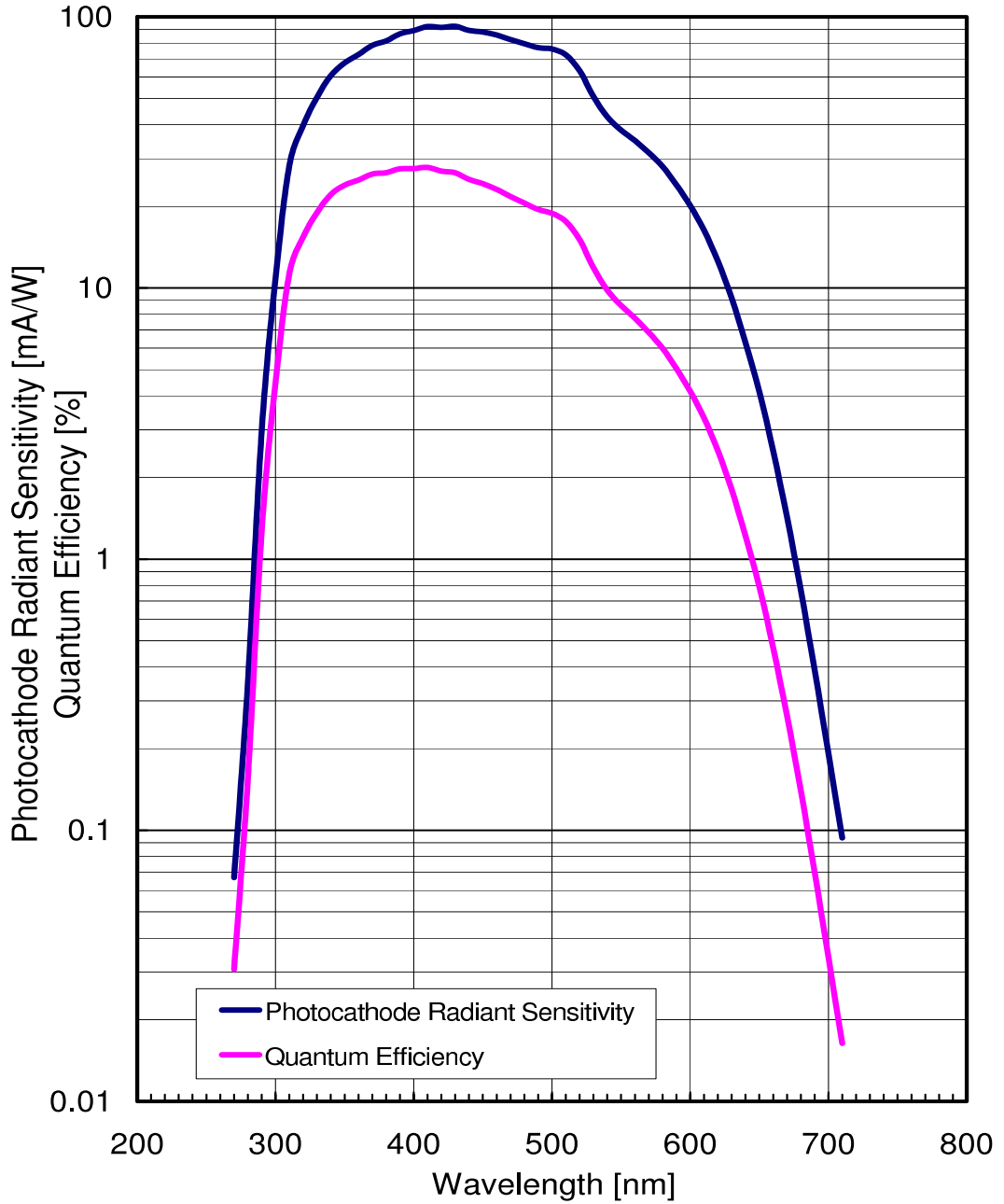
If the PMT output current exceeds a discriminator threshold of  $\sim \frac{1}{4}$ PE, the waveform is captured. The DOM has a Field Programmable Gate Array (FPGA) which initiates the recording of the waveform by the Fast Analog Digital Converter (fADC) and 3 Analog Transient Waveform Digitizers (ATWD). There are three ATWD channels with progressively lower gains of 16, 2 and 0.25 to increase the dynamic range of the readout. Usually only the first ATWD is read out, however, if the first channel saturates the second channel is read out. The third channel is read out when the first two channels saturate. Usually only the highest gain ATWD channel that is not saturated is used for event reconstruction.

To cut down on the noise rate a local coincidence condition is imposed on the DOM's. This is known as the Hard Local Coincidence condition (HLC). This condition causes DOMs only to be read out if one of its closest neighbors also recorded a PE within 1000ns. The local coincidence condition is a tunable parameter in the data acquisition system (DAQ) and is set to span the two DOMs above and the two DOMs below the DOM in question. The local coincidence condition suppresses most of the isolated noise hits and makes the data rate more manageable. New to the IC59 detector is that DOMs that do not satisfy the local coincident condition are read out as well (not the full waveform), but those DOMs cannot participate in

## Spectral Response Characteristics

Tube Type R7081-02  
Serial No. TA2374  
Date Oct.25, 2005  
Tested by M.SUZUKI  
Note

Max. Q.E. 27.9 %  
Wavelength of max. 410 nm



**HAMAMATSU**  
HAMAMATSU PHOTONICS K.K. Electron Tube Division

Figure 3.7: This figure shows the quantum efficiency (QE) of the IceCube DOM PMT as a function of wavelength. The peak QE is at 410nm for this particular PMT [43].

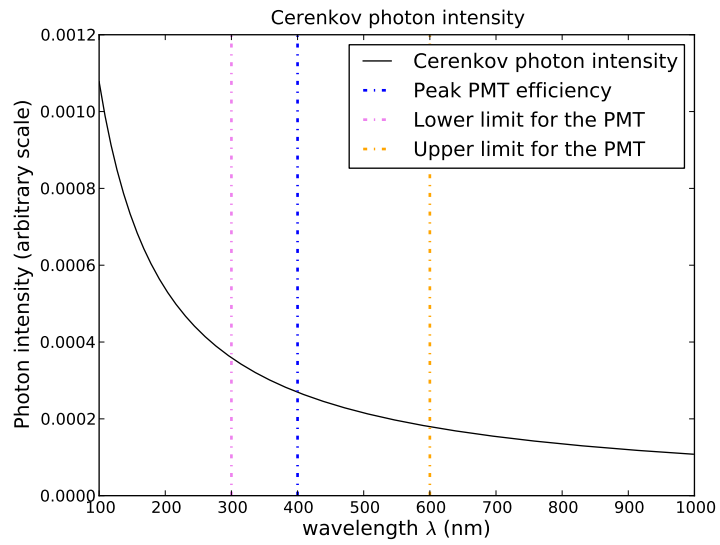


Figure 3.8: The figure shows the falling Cherenkov light intensity with larger wavelength  $\lambda$ . The purple and orange vertical lines indicate the sensitivity range for the IceCube PMT while the blue vertical line indicates the peak quantum efficiency for the IceCube PMT. The Cherenkov light intensity varies by about a factor of two over the sensitivity range of the PMT.

forming a trigger and are thrown out for most reconstruction techniques, however they may be useful for low energy events.

## 3.4 Online Systems

### 3.4.1 Experiment Control - IceCube Live

The IceCube Live system (a.k.a. I3Live) is the experiment control system for IceCube. It provides a simple web-interface that can be used to interact with the detector from the north or the south. Various subsystems of the south pole systems can be controlled through I3Live. In addition to controlling IceCube systems I3Live also provides a modest amount of information about the current and historical state of the detector. The system also allows for defining alerts based on any criteria (run failed etc.) that can be displayed on the webpage, E-mailed or used to page the IceCube staff at the South Pole. Figure 3.9 shows a screenshot of what I3Live looks like during normal operation. From the screenshot it can be seen that basic detector information is displayed, including how many DOMs are currently active, and which Data Acquisition System (DAQ) release is currently running. The current South Pole temperature is displayed as well even though it has little impact on experiment control.

### 3.4.2 Data Acquisition

The Data Acquisition system (DAQ) controls the detector and triggers. The DAQ collects the waveforms from each individual DOM and checks if any of the

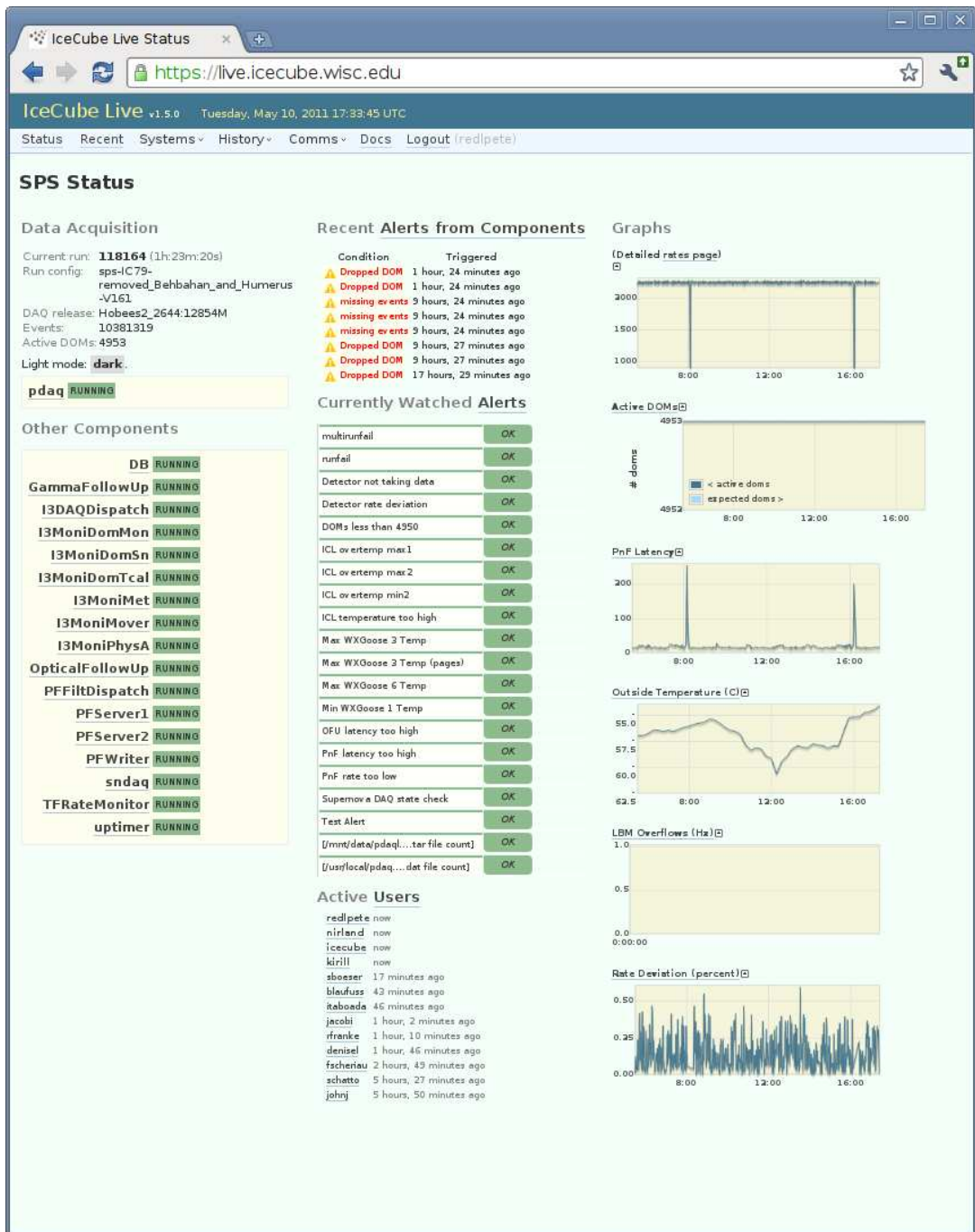


Figure 3.9: This screenshot shows an example of what I3Live looks like during normal operation. In addition to detector information, the current and past temperature at the South Pole is displayed.

trigger conditions that are configured are met. If that is the case, the DAQ forms an event out of the individual DOM waveforms. The DAQ system has a dedicated computer for each deployed string called the DOMHub. This machine houses several custom PCI cards, known as DOR (DOM Readout) cards which supply power to the DOMs on that string. Moreover, the DOR cards are responsible for the communication with the DOMs on that string. The DOMHubs also maintain time calibration records for each DOM and performs calibrations for readout and monitoring events. A schematic of the DAQ is shown in figure 3.10. For more information see [44].

### 3.4.3 Triggers

The DAQ can be configured to check many different trigger conditions and form events for each trigger condition. In the IC-59 detector configuration there were two main trigger conditions used for physics data. The Simple Multiplicity Trigger (SMT) and the String Trigger. The analysis that is presented in this thesis only used the SMT trigger and hence only the SMT trigger is explained. The String Trigger is a low energy trigger aimed at low energy vertical tracks, and since this analysis is predominantly interested in high energy events, String Trigger events are not considered.

#### 3.4.3.1 Simple Multiplicity Trigger

This analysis used the SMT trigger requiring at least 8 hard local coincident hits (see section 3.3 for the definition) within a time window of 5  $\mu$ s. Should that

# pDAQ System

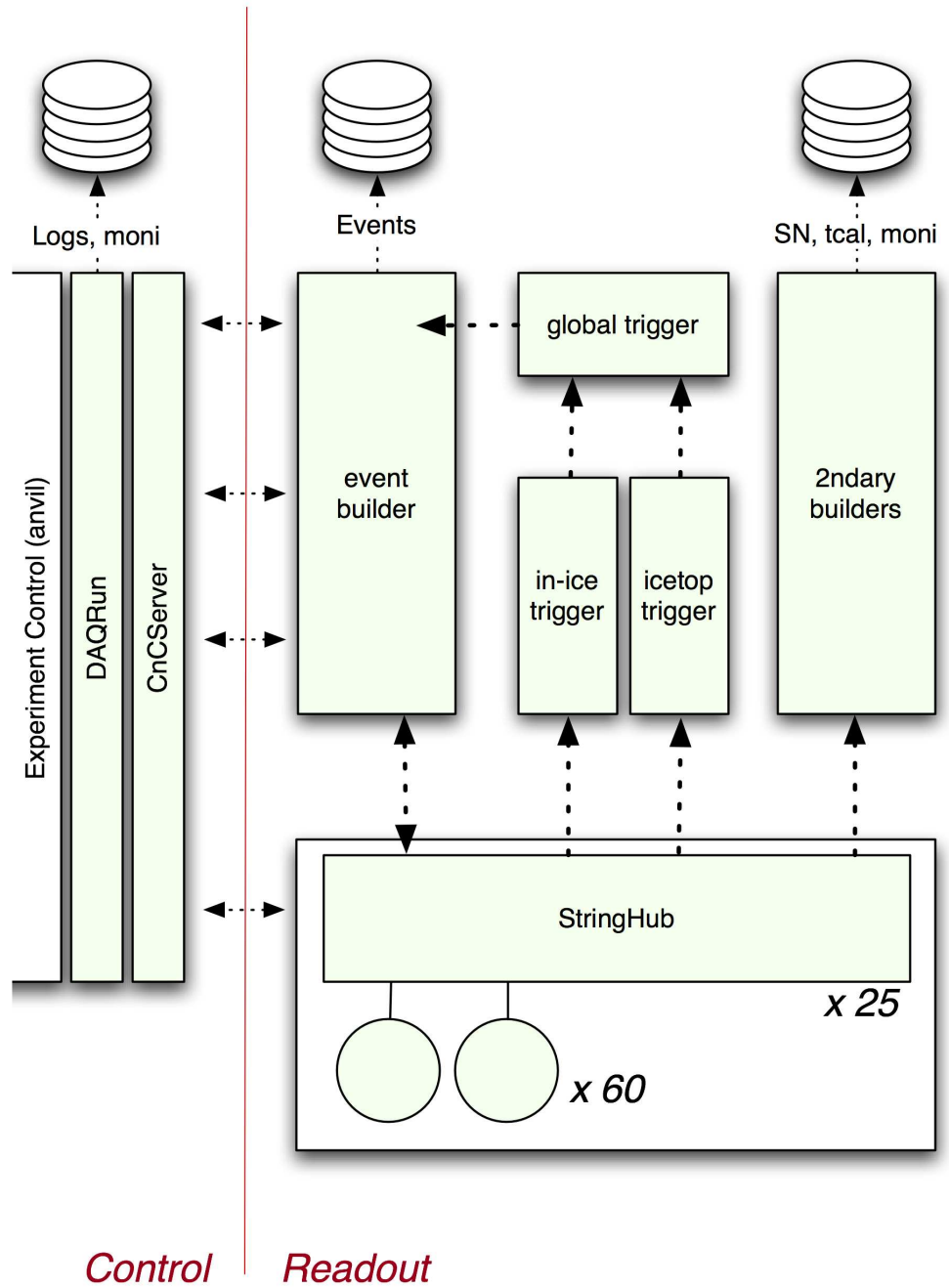


Figure 3.10: This figure shows the experiment control system on the left and the individual DAQ readout elements shown on the right. Taken from [44]

condition be met, a  $1 \mu\text{s}$  time window is added to the last hit. Should there be another HLC hit in that  $1 \mu\text{s}$  time window this window slides to the latest HLC hit. This is repeated until there are no more HLC hits in the  $1 \mu\text{s}$  time window. The time between the first HLC hit and the last HLC hit, forming the trigger, is called the trigger length and often is substantially less than  $5 \mu\text{s}$ . In order to catch early and late hits that did not play a role in making the trigger but might be of interest a readout window of  $-4 \mu\text{s}$  and  $+6 \mu\text{s}$  is added to the first and last trigger hit respectively and all hits that fall within this readout window are kept.

#### 3.4.4 Processing and Filtering

IceCube triggers at a rate of about 2000Hz in the IC-59 configuration, which translates to about 500 GB/day. The National Science Foundation (NSF) has allotted 80 GB/day of data transfer bandwidth acquired from NASA satellites to IceCube. This means that the data stream needs to be reduced at the South Pole before transfer is possible. This is accomplished by physics filters that are motivated by various physics analyses and select events based on criteria relevant to those analysis. Events that pass one or more of these filters are transferred to the north via communications satellites. Events that do not pass any of the filters do not get transferred over the satellite, however no event gets completely discarded as all events are written to tape at the South Pole. This is done in order to be able to analyze data later in the case some physics case was missed by the online filters. Tapes are shipped to the Data Warehouse in Wisconsin once a year for storage.

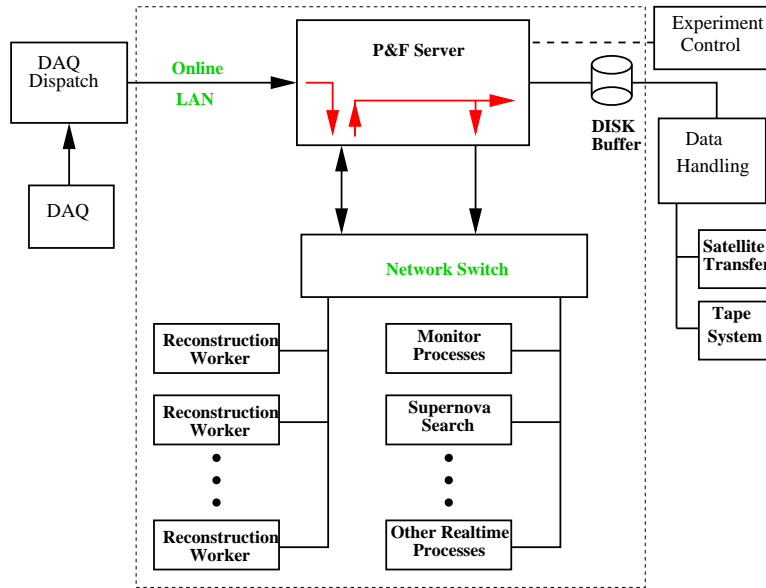


Figure 3.11: The PnF System

The physics filters are implemented by a system called Processing and Filtering (PnF) (figure 3.11). The PnF system can run independently from the DAQ system and data is fed to the PnF system through the DAQ-dispatch buffer. Ideally the time between data taking and processing that data in the PnF system is very short (5 minutes or less), however, in case of PnF system maintenance or unexpected outages this buffer can grow to hold several days worth of data if needed.

The event reconstruction is done by a cluster of machines called pfclients. The PnF server runs a daemon that monitors the DAQ-dispatch system and keeps track of which events need to be filtered. It also keeps track of each client and which client is ready for more data. The PnF server distributes events to the clients on an event by event basis which are recombined into larger files with chronologically ordered events. Events that pass any of the filters get passed to the South Pole Archival

and Data Exchange (SPADE) system. This system manages the transfer of data to the north. It is also responsible for writing all data that is produced to tape.

The south pole system consists of Dell™ servers. The servers are 12 core machines clocked at 2.93 GHz with 24-48Gb of available memory. The system has a total of 300 computing cores and runs Scientific Linux 5.5. There are machines available that are not currently part of the configuration but can be added to the configuration immediately should one of the machines experience a catastrophic failure. This makes the system to be robust with respect to failures of individual clients. The clients themselves process individual events as explained in the previous paragraph. A place of possible system concern is the recombination of events after they have been processed by the clients. The problem is that events necessarily are put back into chronological order after being processed, however, because each event takes a different time to process, the master client has to wait until all the processing clients have finished processing their respective events before it can recombine the events in the correct order. This works well if all of the events take about the same time to process, however, an event that takes vastly longer to process (10s of seconds vs. milliseconds) can cause the system to break. In order to avoid this failure, events that take longer than 30 seconds to process are not filtered and are marked as unfiltered and are transferred to the north. In the north, where processing is less time critical these events are re-examined and can be added back to the normal physics data. In figure 3.12 the processing times of a IC86 test run are shown. It can be seen that the majority of events get processed within 10's of ms with a few outliers. The group of events with processing times  $> 10^4$ ms, are the first events that get

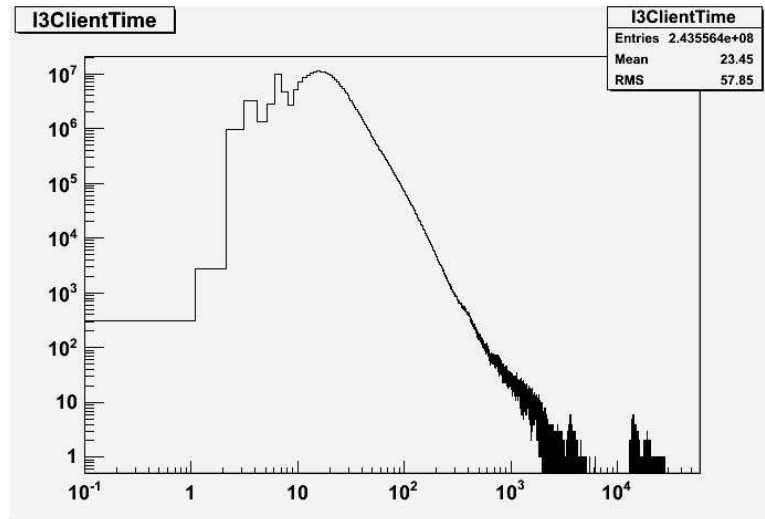


Figure 3.12: This figure shows the processing times of events from an IC86 test run in ms. The group of events with processing times  $> 10^4$ ms, are the first events that get processed in a run and take longer to process because software libraries need to be loaded into the clients memory before processing can begin. Once all the libraries are loaded into memory typical events reconstruct in  $10^1$ 's of ms.

processed in a run and take longer to process because software libraries need to be loaded into the clients memory before processing can begin.

In the IC59 configuration there were 20 active filters producing an event rate of 112Hz. In this analysis only 2 filters are considered; the Muon Filter and the Extremely High Energy (EHE) filter. They produce an event rate of 35Hz and 2.4Hz respectively. Since those are the only filters that are used in this thesis they will be the ones described in detail. Table 7.1 shows a summary of the event rates at each cut stage for the analysis presented here.

## 3.4.5 Filters

### 3.4.5.1 The Muon Filter

The Muon Filter is intended as a filter for SMT8 triggered events only, and hence it does not cover the lowest energy reach of IceCube. The addition of such events would not add sensitivity to the GRB search presented here. The muon filter is designed to be an all sky filter, and considering that the different hemispheres have very different properties, the muon filter needs to take this into account as well. The background in the northern hemisphere can be characterized as a mix of misreconstructed muons, the reducible background, and the irreducible background of atmospheric neutrinos, however, this background is very small and does not limit the sensitivity of this search. In the southern hemisphere, the background looks quite different. In this case a muon and a neutrino producing a muon will look the same to the detector. It is believed that the energy spectrum of astrophysical neutrinos is harder than the energy spectrum of cosmic-ray muons, and hence estimating the energy of an event can help distinguish astrophysical neutrinos from muons in that region. This is done by integrating the total charge of every DOM participating in an event, since higher energy events will have a higher total event charge. The total background increases for smaller zenith angles, and hence the energy cut is made more stringent for subsequently smaller zenith bands. To reduce the processing time, there is also a cut that gets applied before any LogLikelihood reconstructions are done. The cuts used in the muon filter are as follows (cut variables are discussed in Chapter 4.5):

**Base Cut prior to LLH fit:**

- $N_{ch} \geq 8 \ \&\& \ (N_{ch} \geq 10 \ || \ \text{LineFitZenith} < 70)$

**Northern hemisphere  $180^\circ - 80^\circ$ :**

- $\text{LLH1Zenith} < 80 \ \&\& \ \text{LLH1Zenith} \leq 180 \ \&\& \ \frac{\text{LLH1LogI}}{(N_{ch}-2)} \leq 8.2$

**Southern hemisphere  $80^\circ - 0^\circ$ :**

- $(\text{LLH1Zenith} < 70 \ \&\& \ \text{LLHZenith} \leq 80) \ \&\& \ \log(\text{IntCharge}) \geq 1.5$
- $(\text{LLH1Zenith} < 60 \ \&\& \ \text{LLHZenith} \leq 70) \ \&\& \ \log(\text{IntCharge}) \geq 2$
- $(\text{LLH1Zenith} < 50 \ \&\& \ \text{LLHZenith} \leq 60) \ \&\& \ \log(\text{IntCharge}) \geq 2.3$
- $(\text{LLH1Zenith} < 0 \ \&\& \ \text{LLHZenith} \leq 50) \ \&\& \ \log(\text{IntCharge}) \geq 2.7$

Here LLHZenith is the reconstructed zenith direction of an event. Nch is the number of hit DOMs in a given event with LineFitZenith being the reconstructed zenith direction using the linefit method described in 4.5.1. Most of the events used in this analysis come from this filter and hence it is an important part of the analysis.

### 3.4.5.2 The Extremely High Energy Filter

The EHE filter is designed as a catch all filter for high energy events anywhere in the detector. The overlap between the EHE filter and the Muon filter is non-zero, however, not all events that pass the EHE filter pass the muon filter. The idea of the EHE filter is similar to the southern hemisphere muon filter; it calculates the total charge for an event, and if that is beyond a tunable threshold, the event is kept. This

means that events that have a high enough total event charge are kept regardless of the reconstruction quality, with the assumption being that any event that has high enough energy is interesting. The total event charge is calculated using a different software project compared to the muon filter, though the results are comparable. The cut used in the EHE filter is:

### **EHE Filter Cut**

- The threshold value is  $\log_{10}(NPE) \geq 2.8$

Only a marginal number of events come from this filter, however, since it is designed to keep the highest energy events, it is still an important part of this analysis. This filter has a very high overlap with the muon filter and only about 10% of the events that pass this filter do not pass the muon filter as well.

## 3.5 Calibration

### 3.5.1 Timing Calibration

IceCube uses Coordinated Universal Time (UTC) for everything that requires a time. The time is set at the surface using GPS information; however, the same cannot be done for the DOMs since a GPS signal will not penetrate the polar ice cap. This means that the DOMs need to have their own clock to keep time. The DOM clock must be synced to the surface time periodically. This is done with a system called The Reciprocal Active Pulsing or RAPCal. The DOM oscillator is stable and hence this procedure is only done at a frequency of 1 Hz. The procedure

starts with the DOR card sending out a short bipolar pulse to the DOM, which is digitized in the DOM when it is received. The waveform is dispersed to  $\mu s$  length by the time it reaches the DOM and hence a relatively low sampling rate of 20 MHz can be used to capture the waveform. The DOM waits a pre-determined amount of time and then sends out an identical bipolar wave back to the DOR card. In addition, the DOM also sends out a time stamp and the waveform that it recorded in the ice. Once the waveform reaches the DOR card it gets digitized the same way the DOM digitized the waveform in the ice. The time stamp that was sent by the DOM is compared to the Universal Time, so a rough time offset between the DOM and the Universal Time can be achieved. However, a much better precision can be achieved because the waveform has to traverse the same cable going from the DOR card to the DOM as it has going from the DOM to the DOR card. This means that the wave dispersion will be identical going either way and so any feature of the waveform can be used to calibrate the DOM time to the Universal time (see figure 3.13).

### 3.5.2 DOM Calibration

Considering that DOMs are buried deep in the Antarctic ice, they need to be able to calibrate themselves periodically. This section will talk about this calibration (normally done once a month) by a program called *domcal* that is run on each DOM. The DOM mainboard includes a pulser that produces a PMT like pulse that can be used for calibration. The first step of DOM Calibration is to calibrate this

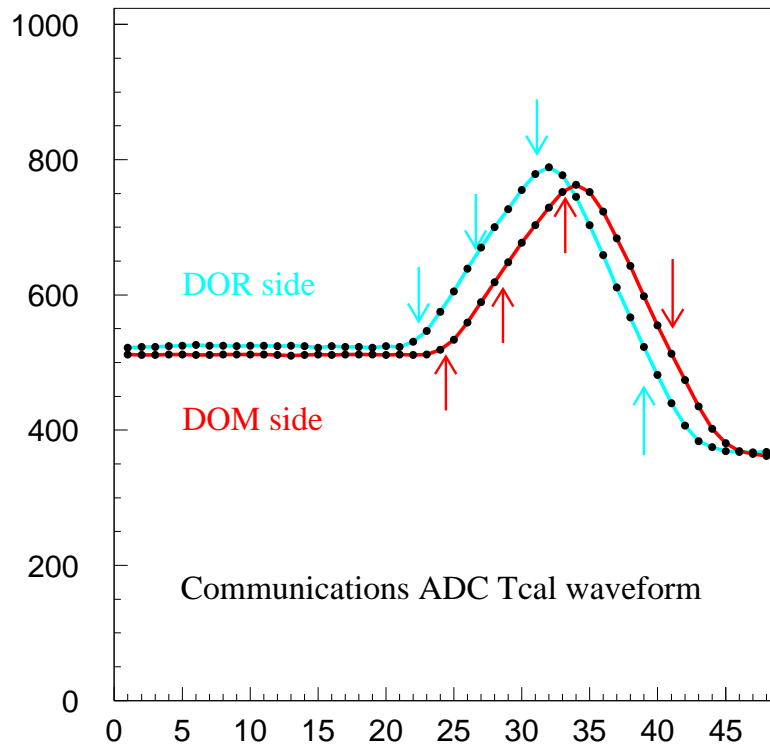


Figure 3.13: This figure shows 2 example waveforms used in the timing calibration. The waveform is shown on the DOR card side and the DOM side. The x-axis is in units of the 20 MHz communications cycle, and the arrows point out different features of the waveform that can be extracted and used for the timing calibration.

pulser. The discriminator on the mainboard is set to a fixed value and the pulser is ramped up until its waveforms trigger the discriminator, and hence the pulser is set to a known voltage. The next step in the calibration process is to calibrate the ATWD bins. Each ATWD produces a set of 128 10-bit numbers for a recorded waveform. The calibrated pulser is used to drive the DOM readouts and the response of each ATWD bin is recorded for known voltages to create a function that maps the ATWD bin response to the real input voltage. The ATWD channels are subject to different amplifications which usually are x16, x2, x0.25, but these values need to be measured directly. This calibration is done by feeding pulses from the pulser at a known voltage into the readout electronics. The output voltage for each ATWD can be measured and the gain for each channel can be calculated. The final ATWD calibration is a sampling speed calibration. The specification calls for a sampling rate of 3.3 ns/sample, however, this number can vary from ATWD to ATWD. The sampling speed is measured by feeding a waveform from the DOM clock to the ATWD which results in a sinusoidal pattern in the readout. The zero-crossings in the readout pattern are counted, which yields a relationship between the ATWD sampling speed and the clock frequency.

### **PMT Calibration**

After calibrating the ATWDs the PMT response to single photoelectrons (SPE) needs to be measured. This is done by turning on the PMT high-voltage and configuring it to collect individual photo-electron events. The timing and voltage information from the previous steps is used to calculate the integrated charge for each event to produce a charge histogram (Figure 3.14). In this histogram there

are 2 prominent features. The first is the exponential tail of low integrated charge which is the noise pedestal and comes from the low-amplitude noise in the PMT. The Gaussian SPE peak is the second feature visible in this plot. To calibrate the PMT the peak-to-valley ratio and the position of the SPE peak are calculated and used to determine the gain of the PMT. To build a relationship between the PMT gain and high voltage this is done for a variety of high voltage settings. The data that was used in this thesis had the high voltage set to a value that corresponds to a PMT gain of  $10^7$ .

### **Applying the calibration**

This calibration procedure is repeated at various times during the life of the detector. Currently it is done once a month, but as the detector matures it may be done less often to help increase the total detector up time percentage. Something to note is that the calibration is not applied in the DOM. The DOM transmits the raw data up to the surface and the calibration is applied later in the processing chain. The only calibration the DOM does is to subtract the noise pedestal. This process reduces most of the values to a baseline that is typically around  $\sim 10\%$  of the full scale. The advantage of having most values be similar values is that it helps with data compression, which is necessary to fit all of the DOM data into the available cable bandwidth.

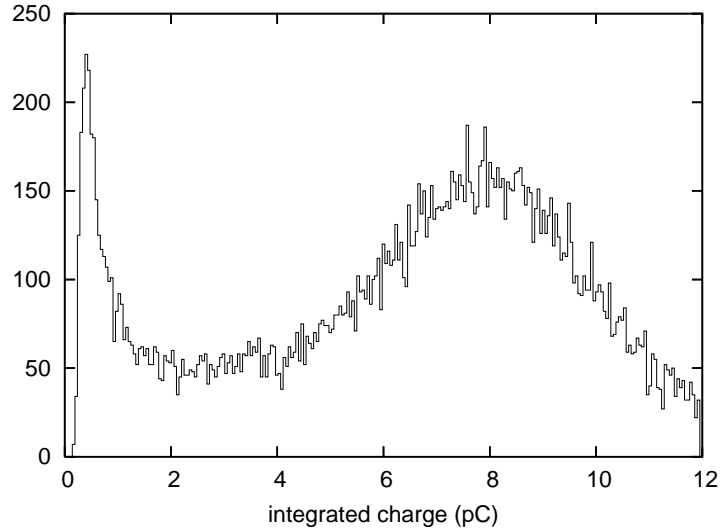


Figure 3.14: This is a typical charge histogram with a PMT voltage set to 1340 V. The Gaussian peak is the SPE peak. The noise pedestal and the second peak caused by random light is visible as well.

### 3.5.3 Geometry Calibration

For the geometry calibration there the vertical and horizontal positions of the DOMs needs to be considered. The vertical position of the DOMs is determined from the final position of the string. The string has sensitive pressure sensors 1000 meters apart at the top of the string and at the bottom of the string. From the final pressure readings before the hole re-freezes one can determine the depth of the string with respect to the water line and hence the final vertical position of the string can be determined. The individual DOM's position is determined by measuring the spacing between the DOMs as they are lowered into the hole. The horizontal position of the DOMs are determined by the combination of a hole location survey and drill position data acquired during the drilling process. Combining the vertical and horizontal measurements, the final DOM positions can be determined to within 0.5 meters,

which is comparable to the timing error of 1.5 ns. The geometry measurement is improved using flasher data after deployment and typically improves the initial position of a DOM by a few cm. The geometry measurement can potentially be further improved by using down going muon data that is in coincidence with IceTop data (IceTop is needed for the directional reconstruction).

### 3.6 Effective Area

It is useful to characterize the detector response in terms of a flux independent quantity. This value is the effective area  $A_{eff}$ . The effective area is defined using a predicted number of neutrino events  $N_{events}$  associated with a diffuse neutrino flux (differential in area, time, energy, and solid angle)  $\Phi(E, \theta)$ . Then the relationship between  $A_{eff}$  and  $N_{events}$  satisfies:

$$N_{events} = \int dt \int d\Omega \int dE \cdot \Phi(E, \theta) \cdot A_{eff}(E, \theta) \quad (3.6)$$

Since the effective area is defined flux-independent one can calculate the expected number of neutrino events in the detector for any neutrino signal without having to re-run simulation since all of the simulation and detector effects can be tied up in that function. While the effective area is flux independent, it is not selection independent, since harder cuts will remove more neutrinos and so  $N_{events}$  is dependent on the strength of the cuts. Since the flux is cut independent the effective area has to change with the cut strength. Figure 3.15 shows the effective area for this analysis at the final cut level as a function of energy. Since the analysis is limited to events that are reconstructed as coming from the northern hemisphere, the effective area

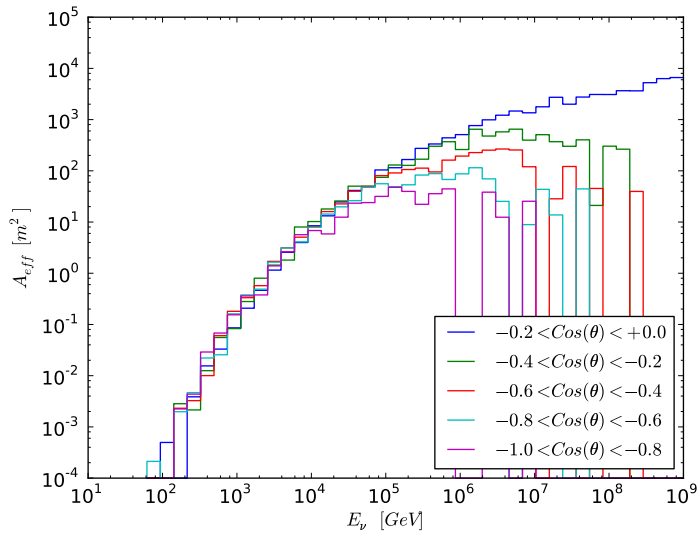


Figure 3.15: The Effective area of IceCube to muon neutrinos at the final cut level in the northern hemisphere analysis at different zenith bands. The effective area for the more up-going region is cut off at higher energies because Earth becomes opaque to neutrinos  $\sim 100$  TeV [45].

for that region is shown.

### 3.7 Simulation

This part of the chapter will be devoted to describing IceCube Simulation with a focus on the simulation that is actually used in this thesis. In essence there are two types of events that need to be simulated in IceCube: 1. Muons and neutrinos from the cosmic rays, which are backgrounds and 2. Muons (electrons, taus) produced in a charged current interaction, the signal. The analysis presented in this thesis uses data to characterize the background and hence background simulation is not needed directly. Background simulation is still used as a cross check and hence will

be discussed. Signal simulation is used in this analysis to develop cuts and calculate the final limit and hence is directly used in this analysis.

The cosmic ray background in IceCube is simulated by starting with a cosmic ray airshower program called CORSIKA [46]. CORSIKA models airshowers that are responsible for the down going muon background in IceCube. For each simulated CORSIKA event there is at least one airshower modeled that results in a single muon, however, because of the frequency of airshowers there is a non-zero probability that more than one airshower occurs in each event. Events with more than one airshower that result in more than one muon in IceCube at the same time are known as coincident events and are the principal source of background events at the highest cut levels. This is caused by the fact that coincident events happen often enough that some fraction of events will produce patterns in the detector that can mimic an up-going track very well, which makes it difficult to eliminate all coincident muons from the final sample.

Neutrino simulation is done with the NUGEN program. NUGEN simulates neutrinos (of whatever flavor is desired) from a zenith range with respect to the detector, or if desired can be configured to simulate a neutrino point source. In either case, it is assumed that a simulated neutrino also interacts near the detector and hence produces a muon. This is un-physical considering that neutrinos have a very small cross section, however, the alternative of throwing a very large number of neutrinos to see which ones interact would be a waste of CPU. To account for the optimistic interaction model near the detector each event gets a weight assigned to it, indicating how likely that particular interaction was, which allows us to work backwards

from a simulated neutrino sample to get the total number of neutrinos that would have been necessary to produce the particular result seen, and hence a final neutrino flux that would produce the observed result. NUGEN is able to produce different neutrino spectra with typical produced spectra being  $E^{-1}$  and  $E^{-2}$ . These spectra can be re-weighted to any spectrum that the user wishes (though harder spectra than the simulated spectrum severely undersample the high energy tail) and hence any spectrum of interest can be investigated without having to simulate that spectrum specifically.

After CORSIKA or NUGEN is run and a muon (or electron/tau etc.) is produced, the rest of the simulation chain is the same. The Muon Monte-Carlo (MMC) [39] program propagates muons through the south pole ice and tracks the continuous and stochastic energy losses. Photons are produced, which are propagated through the ice using a program called photonics [47]. Photonics uses information from MMC where along the track energy loss happened and then propagates photons through the ice and counts how many photo electrons (PEs) arrive at each DOM. It is time consuming to do this for each track considering that  $\sim 10^6$  photons need to be propagated through the ice and hence this is done once and the results are tabulated. From this tabulated result the total number of expected photons at each DOM can be calculated. Photonics also takes into account the ice properties, including absorption and scattering length, in this calculation. Recent advances in graphics card scientific computing using Compute Unified Device Architecture (CUDA) Programming [48] has made it possible to propagate photons for each event without having to tabulate them first. It is still significantly slower than the tabulated results but

shows promise as graphics card technology improves and may replace the tabulated result in the future, but for now has only been used as a cross check.

The next step in simulation is to simulate the hardware response of each DOM. This is done with the PMT-simulator, which is responsible for taking photo-electron arrival times and simulating the PMTs waveform response. The waveforms are then picked up by the DOM simulator which simulates the DOM's mainboard response to that waveform. This involves forming ATWD and FADC waveforms, simulating the discriminator condition, and finally applying the coincidence logic. The last step of the simulation chain is to run trigger-sim which takes the output from DOM simulator for all the DOMs and checks if any of the trigger conditions that were configured have been met. The end result of the simulation chain is a simulation file that can be used in the same way as a detector data file. The difference is that simulation files also contain information about all the particles involved in the process. This allows us to reconstruct simulation events the same way data events are reconstructed and gauge the performance of reconstruction algorithms by comparing the reconstructed track to the true track stored in the data file.

## Chapter 4

### Reconstruction Techniques in IceCube

In Chapter 3 data taking and calibration was described. This chapter will focus on what is done to the data in order to be able to do a physics analysis. The process of determining the path of a muon in the detector is called event reconstruction and is the focus of this chapter. Reconstruction is done in multiple steps since the best reconstruction techniques are also the most CPU intensive techniques and it is resource prohibitive to run them on all events that are detected by IceCube. This makes it necessary to first run less CPU intensive reconstruction techniques on all events followed by cuts that reduce the data volume by a factor of  $\sim 10$ . After those cuts the next level of reconstructions are done (level 2) followed by cuts that cut data down by another factor of  $\sim 10$ . The remaining events are processed to Level 3 which includes the most expensive reconstructions available.

#### 4.1 DOM Cleaning

The first step in the reconstruction chain is to remove DOM data from DOMs that are considered bad. A DOM can be considered bad for a various reasons and there are about 50 bad DOMs in the IC-59 configuration. Some are bad because they never powered up, just stopped turning on, or have high current and cannot be operated. Bad communication with the surface is another problem that can

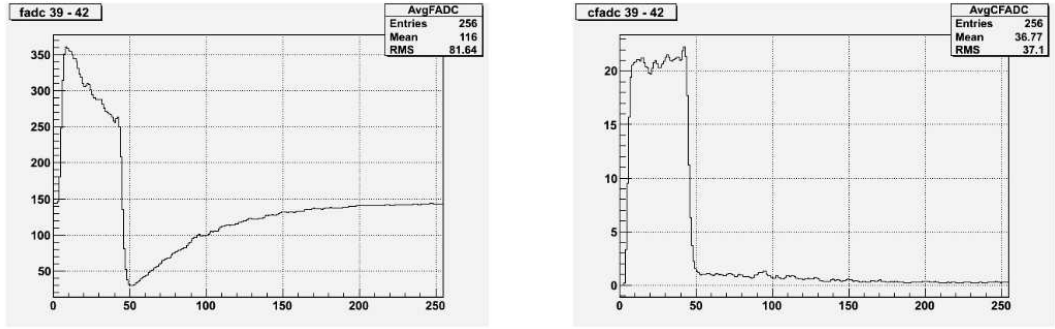
occur, and last, but not least, some have broken LC connections and hence can only contribute to SLC data. The DOM failure rate in IceCube is around 1%. Most of these DOMs do not produce data and any data that is produced is removed before moving on.

## 4.2 DOM Calibration

The next step in the reconstruction chain is to calibrate the raw ATWD and FADC waveforms using the DOMcalibrator module. This module combines the waveforms of all ATWD channels into one calibrated waveform on a bin by bin basis. This means that, if a high gain channel is saturated, the next higher gain channel is used for that bin. To get the entire waveform it is ensured that the length of the longest ATWD channel is equal to the length of the calibrated waveform. DOMcalibrator uses information obtained by the DOM calibration process described in Chapter 3.5.2.

### 4.2.1 Droop Correction

One of the issues that DOMcalibrator has to contend with is transformer droop in about  $\sim 10\%$  of all DOMs. The transformer droop that is seen in IceCube data is caused by a toroid located between the PMT and the HV (High Voltage) board on the DOM. The toroid coupling effectively acts as a high pass filter on the PMT output and causes the tails of the waveforms to droop. This effect is temperature dependent, which makes it more difficult to correct for. However, DOMcalibrator



(a) Before Droop Correction

(b) After Droop Correction

Figure 4.1: The result of droop correction on an uncalibrated waveform. [49]

effectively inverts the toroid high pass filter in software to correct this.

The waveform droop is corrected using a double time constant model instead of a simple single time constant high pass filter model. This means that the response to an impulse signal  $\delta(t)$  is given by:

$$\delta(t) \sim N((1 - f)e^{-t/\tau_1} + fe^{-t/\tau_2}) \quad (4.1)$$

instead of:

$$\delta(t) \sim \frac{1}{\tau} e^{-t/\tau} \quad (4.2)$$

Here  $N$  is the normalization constant and  $f$  gives the mixing of the two characteristics containing  $\tau_1$  and  $\tau_2$ .  $\tau_1$  and  $\tau_2$  must be computed for each DOM separately because they are temperature dependent. The parameters  $\tau_1$ ,  $\tau_2$  and  $f$  are read from the calibration database while  $N$  is naturally computed according to those values. The result of droop correction on an uncalibrated waveform is shown in figure 4.1.

### 4.3 Feature Extraction

The information in this section is taken from [50]. Feature Extraction is the process used to extract important features from the calibrated waveforms. The calibrated waveforms are deconvolved into the sequence of photon-electron arrival times which is done in the software project FeatureExtractor. Feature extraction works by iteratively fitting an increasingly higher number of single photo electron (SPE) waveforms to the calibrated waveform. It is assumed that the calibrated waveforms consist of single SPE-like waveforms and so the total waveform is the sum of all SPE waveforms given by:

$$F^n(t) = b_0 + \sum_{k=1}^n A^k f\left(\frac{t - t^k}{\delta^k}\right) \quad (4.3)$$

$b_0$  is the baseline estimate while  $A^k$ ,  $t^k$ , and  $\delta^k$  are the amplitude, time and width of the  $k^{th}$  pulse respectively. An SPE waveform is given by the function  $f(x)$ .

The process begins with  $n = 1$  and assumes progressively more SPE waveforms in the hypothesis function. At each iteration the parameters are changed to minimize  $\chi^2$  for the fit. The time difference between the fitted waveform and the predicted waveform is then used to seed the time for the  $n + 1$  pulse in the next iteration. This process continues until  $\chi^2$  becomes better than a preset value, stops improving with more fits, or a predefined maximum of SPE pulses is reached. The final result is a number  $N$  of SPE-like waveforms. The time and charge of each of the waveforms is used by further reconstructions.

## 4.4 Time Window Cleaning

Before reconstructions are done, time window cleaning is performed. The purpose of time window cleaning is to reduce early and late noise hits that may skew a fit. Historically, when IceCube was running alongside AMANDA, hits were recorded up to  $50\mu\text{s}$  before and after the first hard local coincidence hits. Considering that a muon takes  $3\mu\text{s}$  to pass through the detector, a  $50\mu\text{s}$  readout window recorded a lot of noise hits that were not part of the event. In the IC-59 detector the readout window has been reduced to  $-4\mu\text{s}$  and  $+5\mu\text{s}$  and hence the total number of noise hits has been reduced as well. Nevertheless time window cleaning is still performed on all events.

Time window cleaning works by using a sliding time window of  $6\mu\text{s}$  that is allowed to slide along all of the hits in an event and maximizes the number of DOM hits found inside that time window. Hits that are outside this time window are removed from the event and the remaining hits are used in event reconstruction.

## 4.5 Reconstructions used in this analysis

This section is devoted to reconstructions specifically used in this analysis. Other analyses have used different reconstruction techniques, however, there is a large overlap.

### 4.5.1 LineFit

Linefit is a simple and computationally fast first guess algorithm. Linefit has two purposes: first, because of its speed it can be run on all events that are produced by the detector, so it serves as a first reconstruction to cut events that are down-going muons. The second purpose is to provide a seed track to be used by other reconstruction algorithms that require a seed track. Of course, instead of using linefit one could use a random direction as the input to likelihood reconstruction, but considering that likelihood reconstructions benefit from a good guess, the linefit track as a seed improves those reconstructions.

Linefit makes the flawed assumption that light travels as a plane wave at a velocity  $\vec{v}$  through the ice. The linefit algorithm is a  $\chi^2$  fit that uses the above assumption to fit a direction for the muon. If we assume that an event has a total  $N_{hit}$  hits with each hit having position  $\vec{r}_i$  and time  $t_i$  then we can write an equation for  $\chi^2$  as follows:

$$\chi^2 = \sum_{i=1}^{N_{hit}} (\vec{r}_i - \vec{r} - \vec{v} \cdot t_i)^2 \quad (4.4)$$

Here  $\vec{r}$  is the reconstructed position and  $\vec{v}$  is the reconstructed velocity vector. An analytic minimization for the above equation exists and the solution can be written as follows:

$$\vec{r} = \langle \vec{r}_i \rangle - \vec{v} \cdot \langle t_i \rangle \quad (4.5)$$

$$\vec{v} = \frac{\langle \vec{r} \cdot t_i \rangle - \langle \vec{r}_i \rangle \cdot \langle t_i \rangle}{\langle t_i^2 \rangle - \langle t_i \rangle^2} \quad (4.6)$$

Here  $\langle X_i \rangle$  is the average over all hits of parameter  $X_i$ . The reconstructed velocity  $\vec{v}$  is used in this thesis as one of the input variables to the boosted decision

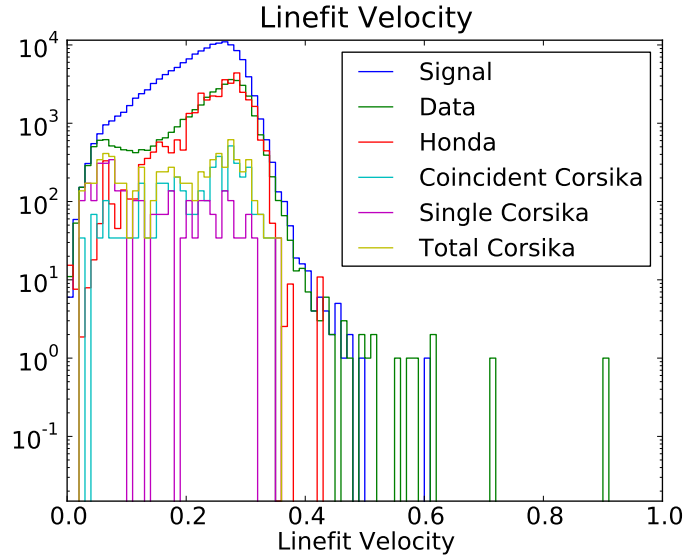


Figure 4.2: This figure shows the linefit velocity at level 3. The velocity is in  $m/ns$ .

tree. In figure 4.2 the linefit velocity for data, signal and background simulation is shown. The velocity is in  $m/ns$  and you can see that there is a peak of  $|\vec{v}|$  near the speed of light. This happens because for well reconstructed tracks the velocity from equation 4.6 is near the speed of the particle passing through the detector, which is  $c$  for muons.

#### 4.5.2 Maximum Likelihood Reconstruction

The muon track reconstruction work horse is the maximum likelihood reconstruction method. In this method, the problem of reconstructing the event can be generalized to estimating a set of unknown parameters  $\mathbf{a}$ , which are related to a set of experimentally measured parameters  $\mathbf{x}$ . A likelihood function  $L$  is formed and the parameters  $\mathbf{a}$  can be determined by maximizing the likelihood with respect to

the measured parameters. The likelihood function is defined as follows:

$$L(\mathbf{x}|\mathbf{a}) = \prod_i p(x_i|\mathbf{a}) \quad (4.7)$$

Here  $p(x_i|\mathbf{a})$  is the probability density function (PDF) of observing the set of measured values  $x_i$  for a given set of parameters  $\mathbf{a}$ .

In the context of IceCube this technique can be used with a little modification. The muon track parameters  $\mathbf{a}$  are assumed to be the vertex position of the track  $x$ ,  $y$  and  $z$  along with the time  $t$ . The zenith angle  $\theta$  and the azimuth angle  $\phi$  describe where the muon is coming from, and are part of the parametrization. This parametrization has too many degrees of freedom, since the position of the vertex is arbitrary in time, meaning that at each time there is vertex that would minimize the parameters. To overcome this issue the time  $t$  of the vertex is assumed to be constant. This leaves five independent variables in the likelihood description.

In this thesis, only DOMs that have a hit are considered. Future implementation of this reconstruction algorithm will likely also take into account DOMs that did not have a hit recorded in the event, but should have been hit according to the current track parameters  $\mathbf{a}$ .

#### 4.5.2.1 Probability Density Function

To define the PDF we have to make a few simple assumptions. First, it is assumed that the muon track is infinitely long moving at the speed of light ( $\beta = 1$ ). The Cherenkov light created by such a muon forms a cone as seen in figure 4.3 and

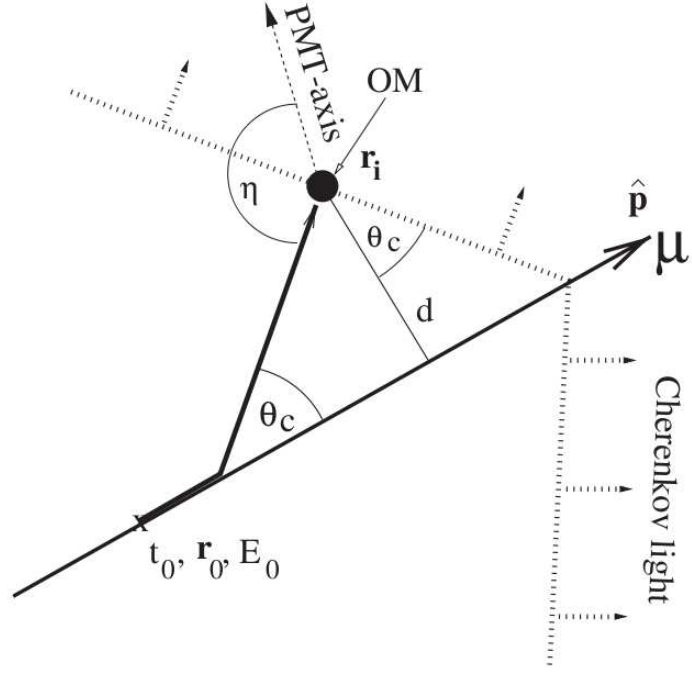


Figure 4.3: This plot shows the Cerenkov cone and the definition of the variables used in the reconstructions.[51]

is described by:

$$\mathbf{a} = (\mathbf{r}_0, t_0, \hat{\mathbf{p}}, E_0) \quad (4.8)$$

Here  $\mathbf{r}_0$  is an arbitrary point along the track at time  $t_0$ . The muon has energy  $E_0$  and direction  $\hat{\mathbf{p}}$  at that time. It would be possible to use a different coordinate system for the reconstruction, and the choice is arbitrary. The reconstruction proceeds by minimizing  $-\log(L)$  with respect to  $\mathbf{a}$ . This minimization gives the same result as maximizing  $L$ , but is computationally easier.

So far the experimentally measured quantities  $\mathbf{x}$  have not been discussed. Each DOM records the full waveform when it is hit by a photoelectron. As discussed before, Feature Extraction will extract the time and the amplitude of the pulse seen.

The timing along with the location of a DOM  $i$  (at  $\mathbf{r}_i$ ) can be used to determine the expected arrival time of a photon given a track hypothesis. From figure 4.3 this time can be written as:

$$t_{geo} = t_0 + \frac{\hat{\mathbf{p}} \cdot (\mathbf{r}_i - \mathbf{r}_0) + d \cdot \tan(\theta_c)}{c_{vac}} \quad (4.9)$$

Where  $c_{vac}$  is the speed of light in vacuum. This equation assumes that the phase and group velocity are the same and hence is the simplest form. The actual  $t_{geo}$  calculation in the code uses the phase velocity to determine the Cerenkov angle, while the group velocity is used to determine the time taken by the light to travel from the hypothesized track to the point of detection [52]. Considering that photons have a scattering length of  $\sim 20$  m in ice and hence many photons will not arrive at the expected time. This means that a residual time,  $t_{res}$ , defined as the difference between the recorded hit time,  $t_{hit}$ , and  $t_{geo}$  can be calculated:

$$t_{res} \equiv t_{hit} - t_{geo} \quad (4.10)$$

A positive value for  $t_{res}$  means that the photon arrived later than expected. For each hit that was recorded in an event ( $x_i$ ) a time residual,  $t_{res,i}$  can be calculated given a track hypothesis  $\mathbf{a}$ . This turns the function  $p(x_i|\mathbf{a})$  into a probability density function in  $t_{res}$ . The residuals distribution will depend on how far the photon had to travel before reaching a DOM ( $d_i$ ) and the angle  $\eta_i$  of the Cerenkov cone to the DOM.  $\eta_i$  is important because a DOM facing away from the Cerenkov cone will only be able to observe backscattered photons, which increases the value of  $t_{res}$  on average. This means that a single hit probability becomes a function of just three

variables,  $t_{res}$ ,  $d_i$  and  $\eta_i$ :

$$p(x_i|\mathbf{a}) \rightarrow p(t_{res,i}|\mathbf{a} = d_i, \eta_i) \quad (4.11)$$

This means that the time likelihood function can be written as follows:

$$L_{time} = \prod_{i=1}^{N_{hits}} p(t_{res,i}|\mathbf{a} = d_i, \eta_i) \quad (4.12)$$

A single DOM could contribute multiple hits to this likelihood. This simplified likelihood still does not allow the reconstruction of the muon direction unless there is a function that gives an analytic estimate of the photon arrival time distribution. This problem was solved with the Pandel Function.

#### 4.5.2.2 The Pandel Function

The Pandel function [53][54][55] is an analytic estimate for the arrival time distribution for a monochromatic, isotropic point of light in a medium, where scattering is the dominant effect. Cerenkov light is produced along the track and hence behaves like a string of isotropic point sources. In ice, the scattering length is  $17m$  while the absorption length is  $100m$  and therefore scattering dominates. This means that the Pandel function can be used as an analytic estimator for photon arrival times. The Pandel function is expressed in terms of  $t_{res}$  and the distance  $d$  to the point of emission:

$$p_{pandel}(t_{res}, d) \equiv \frac{1}{N(d)} \frac{\tau^{(-d/\lambda)} t_{res}^{(d/\lambda-1)}}{\Gamma(d/\lambda)} \cdot e^{-(t_{res} \cdot (\frac{1}{\tau} + \frac{c_{medium}}{\lambda_a}) + \frac{d}{\lambda_a})} \quad (4.13)$$

$$N(d) = e^{-d/\lambda_a} (1 + \frac{\tau \cdot c_{medium}}{\lambda_a})^{-d/\lambda} \quad (4.14)$$

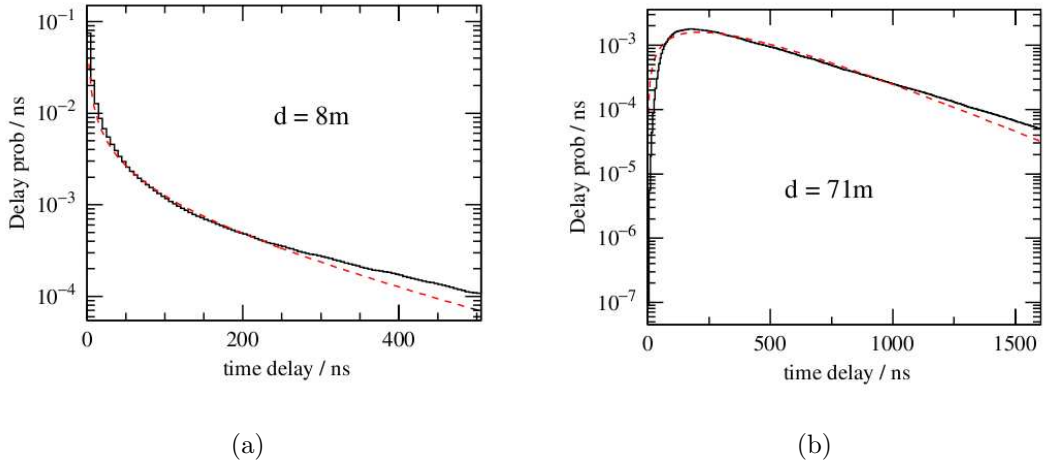


Figure 4.4: Comparison of the parametrized Pandel function (dashed curves) with detailed simulation (black histogram) at different distances  $d$  from the muon track. Taken from [51]

In these equations  $c_{medium} = \frac{c_{vac}}{n}$  is the speed of light in ice.  $\lambda_a$  is the absorption length,  $\Gamma(d/\lambda)$  the gamma function while  $N(d)$  is the normalization factor. Figure 4.4 shows examples of the Pandel function.

The Pandel function has some limitations that need to be considered. First of all it is not defined for values of  $t_{res} < 0$ . It also has a pole at  $t_{res} = 0$  both of which cause numerical difficulties. Other non-computational problems with the Pandel function are that it does not take into account DOM orientation relative to the light source, nor does it take into account PMT jitter. These issues need to be addressed, which is done by patching the Pandel function in several ways. First of all, to take into account the PMT orientation, the distance to the the track  $d$  is taken to be an effective distance  $d_{eff}(\eta)$ , which takes into account that light is more scattered the more the PMT is facing away from the track and as a matter of fact must be

scattered to be recorded if the PMT is facing completely away. The PMT jitter is taken into account by convoluting the Pandel function with a Gaussian with a width corresponding to all timing uncertainties. In this way, the pole at  $t_{res} = 0$  is removed and negative values for  $t_{res}$  are allowed. Noise hits are ever present in IceCube and need to be treated in the Pandel function. This is done by adding a small constant offset that corresponds to the average of all noise hits as determined through simulation.

Now that the Pandel function is defined we can go back to the likelihood function (see equation 4.12) maximize it to find the best fit. In practice, this is implemented by minimizing  $-\log(L(\mathbf{x}|\mathbf{a}))$ , which is the same as maximizing  $L(\mathbf{x}|\mathbf{a})$  but easier computationally. It also uses a seed track to begin the reconstruction to determine  $\mathbf{a}$ . Track parameters are then varied until the minimum of  $-\log(L(\mathbf{x}|\mathbf{a}))$  is reached. Advanced reconstruction techniques then proceed and use the result of the first minimization to seed the next one, which continues until a pre-set maximum of iterations is reached.

This is implemented in the software project Gulliver for the IceCube reconstruction [56]. This project is highly configurable and allows for different seeds, different PDFs, and minimizers. The current minimizer being used is MIGRAD which is implemented through TMinuit from the software project ROOT [57]. Gulliver does allow for other minimizers, which have been tested in the past but were not used in this thesis.

## 4.6 Specific LogLikelihood based reconstructions used in this thesis

This section will discuss specific Loglikelihood based reconstructions used in the thesis.

### 4.6.1 Single Photoelectron Fits (SPE)

The single photoelectron fit uses the modified Pandel function described in 4.5.2.2 to predict the arrival times of the first photoelectron. This implementation ignores all PE's that arrive after the first and hence does not use all of the information that is available; regardless, good results are still achieved. The SPE fit uses linefit, described in section 4.5.1, as a seed. In IC59 a 10 iteration SPE fit is seeded by a single iteration SPE fit. Each subsequent iteration uses the previous result as a seed and the best minimization of  $-\log(L(\mathbf{x}|\mathbf{a}))$  is used as the final result.

The output of the SPE-fit is not only a best fit track but also includes quality parameters that determine the goodness of the fit. The most used of these is the reduced log likelihood parameter (rlogl). Rlogl is the final minimized loglikelihood divided by the degrees of freedom, which are approximately equal to the number of DOMs participating in the event. This is a better quality parameter than just the minimized loglikelihood because direct comparison between the minimized loglikelihood of different events is not possible because a track with many hit OM's will have a larger value for the minimized loglikelihood than a track with few hit OM's even though the track with the additional hits may have a better reconstruction. Rlogl takes this into account and makes it possible to compare different tracks directly.

Another quantity that comes out of the likelihood reconstruction is the number of direct hits,  $N_{dir}$ . A direct hit is defined as a hit on an OM that has a  $t_{res}$  such that:

$$-15ns < t_{res} < 75ns \quad (4.15)$$

When this condition is met it can be postulated that the photon was not scattered on the way to the DOM and hence will convey more reliable information about the track compared to a photon that was scattered. Hence a track with many direct hits is likely to be of better quality than a track with few.

Another track parameter calculated at this time is the *length of the event parameter*. This parameter projects all hit DOM's onto the track and calculates the distance between the two points farthest apart. This effectively acts as the ‘‘lever arm’’ of the reconstruction and larger values in general correspond to better reconstructions. In this analysis this parameter is used as an input to the boosted decision tree when calculated for direct hits only and is referred to as  $L_{dir}$ .

#### 4.6.2 Multiple Photoelectron Fits

The PDFs discussed so far accurately model the arrival times of the first photoelectron, but ignore all subsequent photoelectrons. For high energy events, the most interesting events as far as this thesis is concerned, DOMs will see more than one photoelectron and hence the single photoelectron fit is not as accurate. This is corrected by using a PDF that models all photoelectrons that arrive at a DOM:

$$\text{MPE}(t_{res}) = n \cdot \text{SPE}(t_{res}) \cdot \left[ \int_{t_{res}}^{\infty} \text{SPE}(t) dt \right]^{n-1} \quad (4.16)$$

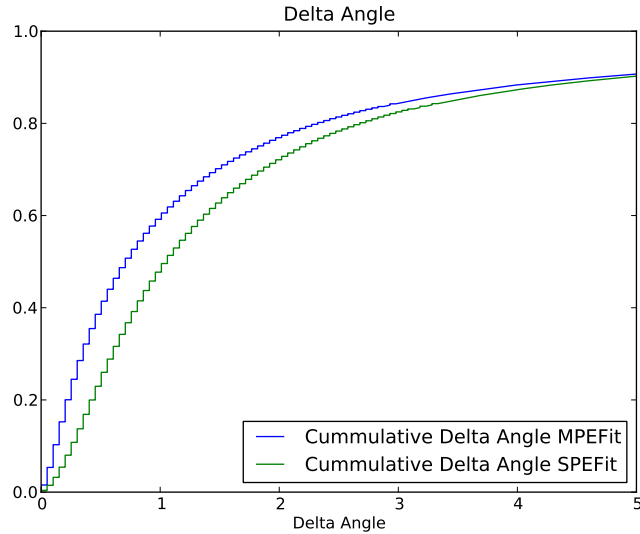


Figure 4.5: This plot shows a cumulative delta angle distribution for signal simulation (in degrees). Here a value of 1 on the y-axis means that all events are reconstructed with an angular offset from the true direction corresponding to the x-value at that point. It is clear that using a single iteration MPE fit improves the result.

This is a more accurate PDF and can yield better results than the simple PDF presented before. One of the issues is that this is a more complicated function that has more local minima, and hence one runs the risk of not finding the global minimum when minimizing  $-\log(L(\mathbf{x}|\mathbf{a}))$ . Moreover, the minimization is more time consuming and hence running many iterations of this minimization is time prohibitive. In this analysis these issues are addressed by first running a multiple iteration SPE fit, which then gets used as a seed for the MPE fit reconstruction. Doing multiple MPE fit reconstructions does not improve the track resolution and hence only one iteration is done. Figure 4.5 shows the improvement in angular resolution achieved by doing an additional MPE fit over just doing a SPE fit reconstruction.

### 4.6.3 Paraboloid Fit

The information in this section is taken from [58]. The paraboloid fitter is used to get an estimate of the uncertainty in a likelihood reconstruction by studying the behavior of the likelihood space around a reconstructed track. This is done by first transforming the coordinate space to one centered on the direction of the input track. It then proceeds by attempting to fit a paraboloid to the likelihood space around the seed track. The important result that this paraboloid provides is an estimate on the fitted track uncertainty. This uncertainty is known as paraboloid sigma and is calculated from the major and minor axis of the fitted paraboloid:

$$\sigma \equiv \sqrt{\frac{1}{2}(\sigma_1^2 + \sigma_2^2)} \quad (4.17)$$

$\sigma$  provides a good estimate for the track uncertainty and it can be checked using simulation. This check is done by calculating the difference between the true track and the reconstructed track and comparing that value to  $\sigma$  obtained from paraboloid sigma. In figure 4.6, the difference between the true track offset minus the uncertainty in paraboloid sigma is plotted. Ideally, the value would always be zero indicating that paraboloid sigma gets the uncertainty right all the time. Figure 4.6 shows that there is a clear peak near zero with Gaussian tails. The tail on the positive side is longer because paraboloid sigma is more likely to fall into a local minimum during the minimization and therefore underestimate the error than to not find a minimum at all and hence overestimate the error. This is something that is corrected for, however, the raw output is shown here to point out this limitation.

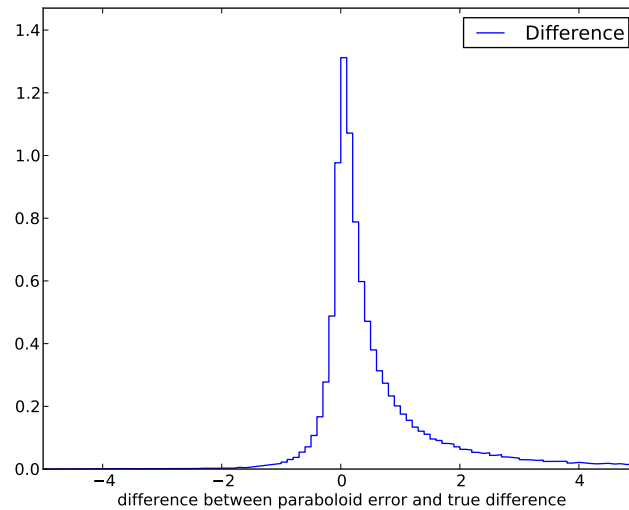


Figure 4.6: Plotted here is the difference between the true track offset minus the paraboloid error for that track ( $\sigma_{true} - \sigma_{paraboloid}$ ). Ideally this value should always be zero. This plot shows that this value is peaked around zero with Gaussian tails falling off in either direction. The tail on the positive end is more pronounced because paraboloid sigma is more likely to fall into a local minimum during the minimization than to not find a minimum and hence it is more likely to underestimate an error than to overestimate an error. This is something that is corrected for later but the raw output is shown here.

#### 4.6.4 Bayesian Up/Down Fit

Considering that most events that are recorded in IceCube are down-going muons the Bayesian Up/Down fit is designed to eliminate events that are misreconstructed as up-going. This is accomplished by first assuming that an event is most likely a down going muon and so the likelihood function is multiplied by a bias function in Zenith that favors down-going tracks over up-going tracks. In this way information about the bias in the data sample is introduced. The zenith function used models down-going muons as follows:

$$w = a_0 \cdot [\cos(\text{zenith})]^{a_1} \cdot e^{\frac{a_2}{\cos(\text{zenith})}} \quad (4.18)$$

with  $a_0 = 2.39655 \times 10^{-7}$ ,  $a_1 = 1.67721$ , and  $a_2 = 0.778393$ . This approach makes down-going tracks more likely and up-going tracks should only be found if the regular likelihood is good enough to counteract the bias introduced by the Bayesian weighting function.

A useful quality parameter can be defined as the difference between the regular likelihood and the Bayesian likelihood:

$$Q_{\text{bayesian}} = L_{\text{Bayesian}} - L_{\text{SPE}} \quad (4.19)$$

Here  $L_{\text{Bayesian}}$  is the Bayesian likelihood and  $L_{\text{SPE}}$  is the regular likelihood. Misreconstructed up-going events will have  $Q_{\text{bayesian}}$  values that are smaller than those for up-going events (Figure 7.2 shows  $Q_{\text{bayesian}}$  for events that are used as input to the Boosted decision tree learning algorithm).

### 4.6.5 Energy Reconstruction

The reconstruction techniques that have been described are all used to determine the direction of the muon while energy has not been reconstructed. The expected GRB neutrinos are theorized to have a harder energy spectrum than atmospheric neutrinos, which make up the irreducible background. Hence energy information can be used to help identify signal neutrinos and the energy needs to be reconstructed, which is accomplished with photorec [59].

Based on a fitted track, photorec calculates the average energy loss per unit propagation length for a muon ( $\frac{dE}{dX}$ ). Muons with higher energy lose more energy and because energy loss is related to the photons emitted along the track more photons are detected. Several things can influence the number of photons that are detected vs. how many photons are emitted. To get this proportionality right additional factors need to be taken into account, such as ice-properties, the distance from the reconstructed track to the DOMs observing photoelectrons and the amount of scattering/absorption between the creation and detection points of the photons. This algorithm assumes that the muon energy loss is uniform along the track.

### 4.7 The Topological Trigger

There is one more cut parameter that is used in this thesis that has not been discussed so far. This cut parameter is known as the topological trigger and is applied as a level 3 cut (see table 7.1 for a summary of the cut efficiencies). The topological trigger uses three criteria to determine whether pulses [50] are connected.

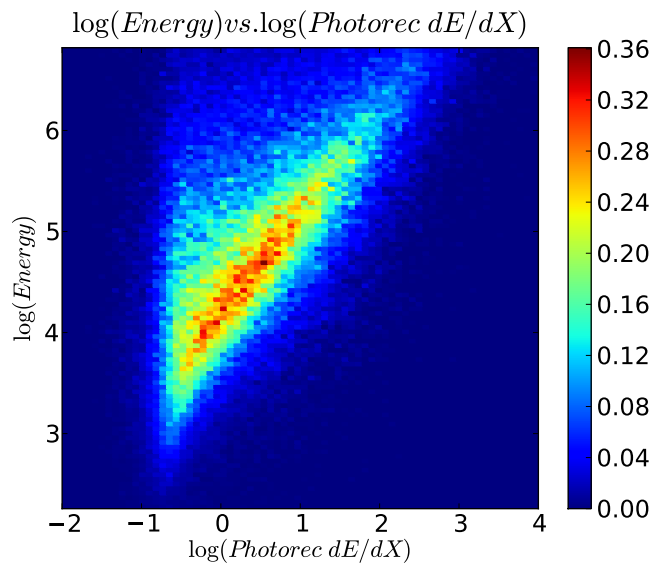


Figure 4.7: This plot shows the log of the true energy of a simulated muon on the y-axis while the log of the photorec parameter  $\frac{dE}{dX}$  is shown on the x-axis. A correlation between the two quantities can be seen and hence  $\frac{dE}{dX}$  can be used as a stand in for muon energy. Muon energy in turn is related to the primary neutrino energy and therefore  $\frac{dE}{dX}$  is related to the primary neutrino energy [60]

The criteria are:

- Timing within  $t$  of muon crossing time ( $\Delta t < 450\text{ns}$  for IC59)
- XY separation less than  $r$  meters (300m in X-Y spacing for IC59)
- Z spacing of less than  $z$  DOMs (30DOMs(510m) in Z for IC59)

If two pulses pass all of the criteria they are determined to be topologically connected and therefore belong to the same sub-event. After creating all the sub-events for a given event all sub events are reconstructed using a SPE fit (see section 4.6.1) and events that are not split, or events that have their largest sub event reconstructed as up-going are kept.

## Chapter 5

### GRB Selection

All GRB satellite triggers that occurred during the IceCube 59-string physics are considered for inclusion in the analysis, and by extension, in this thesis. Satellites being included are: Fermi, Swift, Konus and other Third Interplanetary Network (IPN3) satellites. Bursts are identified in the form "GRBYMMDDD", where YY and MM refer to the last 2 digits of the year and the month respectively. DDD refers to the last 2 digits of the day in addition to a suffix starting at 'A'. The suffix is there to distinguish multiple GRBs during one day with 'A' being the first GRB and 'Z' would be the 26<sup>th</sup> GRB of that day.

#### 5.1 Gamma-ray Burst Coordinate Network

The Gamma-ray Burst Coordinate network (GCN) is a system that distributes information about the location (and other information) from satellites to interested third parties. GCN initially sends out a *notice* for a detected GRB. This initial message is a satellite trigger and is sent out as quickly as possible in order to allow follow up measurements by other instruments (optical, X-ray or other wavelength). The information in the *notices* is not the most accurate information that a satellite can provide and more in-depth analyses are done on the GRB triggers on the ground by the various satellite operation groups. After this analysis is done a second set of

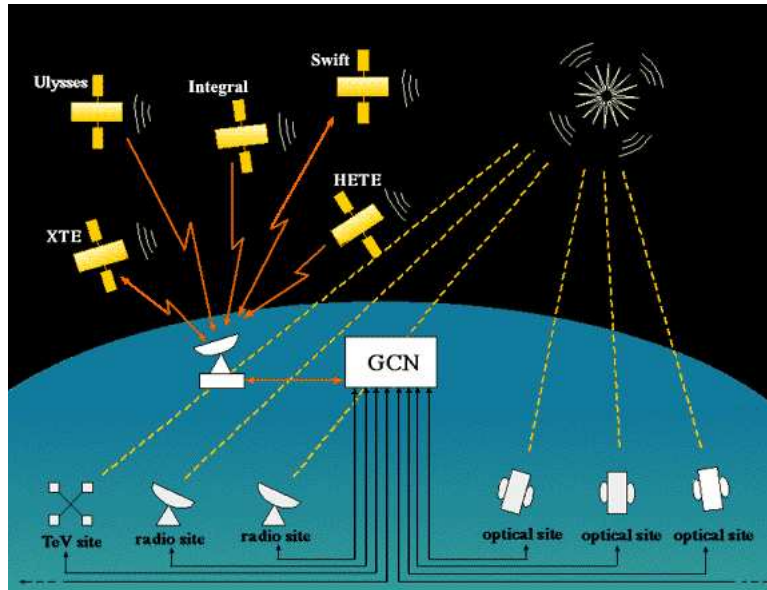


Figure 5.1: This figure shows a graphical representation of the Gamma-ray Burst Coordinates Network. It can be seen that the satellites feed into the GCN with the GCN distributing the information to any interested party to do afterglow observations or in the case of IceCube search the data taken during the time of a GRB for a neutrino coincidence [61].

messages, called *circulars* are sent out, which contain more accurate and detailed information about detected GRBs [61]. A graphical representation of GCN is shown in Figure 5.1.

## 5.2 Satellites

### 5.2.1 The Fermi Gamma-ray Space Telescope

The Fermi Gamma-ray Space Telescope (Fermi) observed the most GRBs used in this thesis. Fermi was launched on June 11, 2008 as a joint venture between NASA, The United States Department of Energy (DOE) and other government agencies in Germany, France, Italy, Japan and Sweden. Fermi was designed with a

goal of 10 years of operation and some of the key scientific goals were the understanding of active galactic nuclei (AGNs), to resolve unidentified sources of gamma-rays, to look for diffuse sources of gamma rays and to determine the high energy behavior of GRBs and other transient sources.

Fermi carries two scientific instruments on board to achieve its scientific goal. The first is the Large Area Telescope (LAT). The LAT is an imaging gamma-ray detector designed to detect photons in the energy range of 30MeV – 300GeV. Its field of view is limited to about 20% of the sky. The second instrument on board is the Gamma-ray Burst Monitor (GBM). The GBM consists of 14 scintillation detectors and is sensitive to photons in the energy range of 150keV – 30MeV. The GBM has the advantage that it is a  $4\pi$  detector and hence is sensitive to the entire sky that is not blocked by earth. This optimal sky coverage comes at the expense of angular resolution. The GBM is only able to resolve gamma-rays at a resolution that is similar to IceCube’s resolution ( $\sim 1^\circ$ ).

#### 5.2.1.1 Gamma-ray Burst Monitor (GBM)

As mentioned above the GBM is designed as an all sky detector and hence it needs to consist of multiple detectors placed all around the satellite. This is accomplished with two separate sets of detectors: twelve sodium iodide (NaI) scintillators and two cylindrical bismuth germanate (BGO) scintillators [62]. The NaI detectors are 12.7 cm in diameter and 1.27 cm in height. The BGO scintillators are 12.7 cm in diameter and 12.7 cm in height. The NaI detectors are designed to be sensitive

in the lower energy range of the GBM from about 1 keV to about 1 MeV and are responsible for burst triggers and locations. The BGO detectors cover the energy range of 150 keV to 30 MeV providing overlap with the NaI detector at the lower end and overlap with the LAT at the higher end. The GBM triggers if at least two of the NaI detectors observe a change in count rate. The localization uncertainty for the GBM is  $\sim 1^\circ$ , however, it varies significantly for GRBs in this sample and is as large as  $12^\circ$ .

#### 5.2.1.2 Large Area Telescope (LAT)

The LAT's purpose is to detect individual gamma-rays. In the energy range for which the LAT is designed, photons that interact with matter will pair produce  $e^+e^-$  pairs, which forms the underlying measurement principle, because it provides a unique gamma-ray signature compared to what you would see for cosmic rays. This is important because the cosmic ray flux is as much as  $10^5$  times larger compared to the gamma-rays. Therefore it is important to reconstruct  $e^+e^-$  pairs while rejecting cosmic rays.

Incident radiation initially passes through an anticoincidence shield, sensitive to charged particles, followed by thin layers of high-Z material (Tungsten) known as conversion foils. Pair production is facilitated in the field of a heavy nucleus, and after a  $e^+e^-$  pair is created particle tracking detectors measure the trajectory. The energy is measured by a calorimeter. The characteristic gamma-ray signature inside the LAT has three features: 1. there is no signal in the anticoincidence shield, 2.

there is more than one track starting at the same location within the particle tracker and 3. there is an electromagnetic shower in the calorimeter.

The LAT consists of a 4 by 4 array of identical towers, each 40 X 40 cm<sup>2</sup> tower consists of a tracker, calorimeter and data acquisition module. The tracker is built from 18 layers of silicon strip detectors. This technology has been used in ground based particle accelerators for many years and hence is a proven technology. The calorimeter consists of 8 layers of 12 CsI bars arranged hodoscopically and read out by photodiodes. The total thickness of the calorimeter is  $\sim 10$  radiation lengths and because of the hodoscopic arrangement it is able to detect three dimensional profiles of showers. Finally the anticoincidence shield covers the entire array of towers using segmented tiles of scintillator, which are read out by wavelength-shifting fibers and miniature phototubes. Figure 5.2 shows a schematic of the Fermi space telescope. More information on Fermi can be found here [17].

### 5.2.2 Swift

Swift provides the second most GRBs that are used in this thesis. Swift was launched in November of 2004 with the primary scientific goal being to determine the origin of GRBs and hence probe the early universe [16] [63].

Swift is designed to be a multi-wavelength detector that is sensitive to gamma rays, X-rays, ultraviolet and optical wavelengths. Moreover, it has the ability to quickly slew to a position of a burst after one is detected. There are three instruments on board the satellite: the Burst Alert Telescope (BAT), the X-Ray Telescope (XRT),

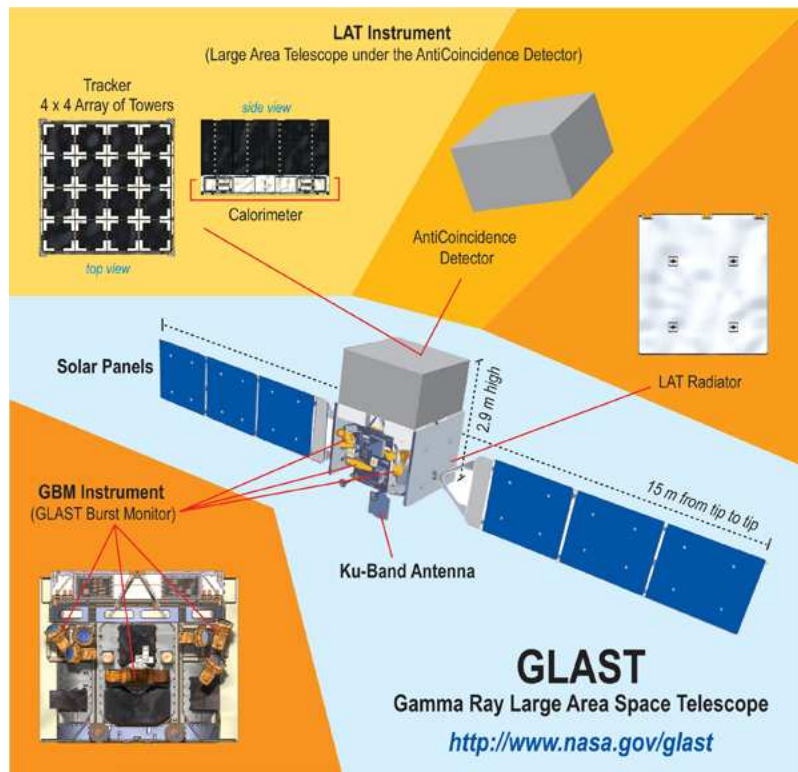


Figure 5.2: This image shows the Fermi space telescope, including all of the detectors found on the satellite[17]

and the Ultraviolet and Optical Telescope (UVOT). While the XRT and UVOT have very narrow fields of view (FoV), the BAT has a larger FoV and therefore is responsible for detecting GRBs. If BAT detects a new GRB, it can autonomously slew the satellite to bring the GRB into the FoV of the XRT and UVOT. The autonomous nature of Swift's slewing makes it possible to perform X-Ray and UV/optical observation of about 100 bursts per year within 20-70 seconds of a burst detection. Figure 5.3 shows a photograph of Swift just before its launch in 2004.

The most important instrument for this analysis on board Swift is the BAT, because it is responsible for the initial detection of gamma-ray emission from a burst [64]. Upon detection of a burst, a location is calculated and sent to the satellite control circuits so that Swift can slew to the direction of the burst. BAT is sensitive to photons in the 15 – 150keV energy range with a pointing resolution of 1-3arcmin. Data from the satellite is run through a refined analysis on the ground, which is the data that gets used in this thesis.

The BAT is able to monitor about two steradians of the sky using a coded aperture image algorithm. There are no focus optics involved in part because a large field of view is needed and in part because it is hard to use focus optics for photons above 10keV. BAT uses a coded aperture mask that is made up of 54,000 lead tiles arranged in a known pattern. Photons hitting this mask will cast a shadow across an array of detectors positioned below the mask. The detector is about 1 meter below the lead tiles and consists of 32,768 4mm CdZnTe hard X-ray detector tiles. A Fourier transform algorithm then compares the shadow detected to an expected shadow from every point in the sky. The result shows bright points for gamma ray



Figure 5.3: This image shows a photo of Swift just before launch in 2004. The three detectors are located on top of the spacecraft. BAT is the largest of the detectors and is seen as the large silver enclosure. XRT and UVOT are the much smaller detectors found between BAT and the black sheet at the back of the satellite. [16]

sources in the sky and dark background everywhere else. If one of the bright points exceeds a pre-determined trigger threshold, a GRB detection is claimed.

The X-Ray Telescope (XRT) is designed to detect X-ray afterglows from GRBs detected by the BAT. The XRT is sensitive to photons in the range of 0.2 – 10keV and is able to measure fluxes, spectra, and light curves over that energy range. The XRT has a wide dynamic range for flux and is able to cover  $\sim 7$  orders of magnitude in flux [65]. The XRT has an accuracy of  $\sim 5$  arcsec within 10 seconds of data taking of a typical X-ray source. The XRTs main purpose is to study X-ray counter parts to GRBs and does so by detecting GRB X-rays after Swift slews to the newly discovered GRB. X-ray data taking begins within 20-70 seconds after a GRB discovery and continues for days to weeks depending on the source. The XRT provides many of the final GRB coordinates used in this thesis. The UVOT has better angular resolution, however, many more GRBs have X-ray afterglows and hence the XRT sees more GRBs.

The Ultraviolet/Optical Telescope (UVOT) is designed to detect optical afterglows for GRBs. It is able to provide sub-arcsec accuracy in GRB position and can provide ultra-violet and optical photometry. Moreover, UVOT is used for long term follow-ups on GRB afterglow lightcurves. A few of the GRBs used in this thesis have their position localized by the UVOT, however, because of the event uncertainty of IceCube it isn't an advantage to use UVOTs position over the XRT position. Nevertheless, because the best position should be used and therefore UVOTs data is used when available. The UVOT also has the ability to determine the redshift of a host galaxy, which is used in the neutrino flux calculation shown in Chapter 2.2.3

and therefore yields a better prediction of the neutrino flux.

More information on Swift can be found in [16].

### 5.2.3 Third Interplanetary Network (IPN3)

The Third Interplanetary Network is a group of GRB detectors designed to measure the arrival time of gamma-rays from GRBs [66]. Seven of the GRBs used in this analysis are observed by IPN and have information provided by IPN used and therefore are in the minority compared to Fermi and Swift, which observed the remaining 91 GRBs used in this thesis. IPN uses information from multiple satellites and the arrival times of photons at each of the satellites to reconstruct the position of a GRB. The current version of IPN3 started in 1992 and currently consists of Swift, Suzaku, AGILE, Konus-Wind, Integral, 2001 Mars Odyssey, Messenger, Rhesi, and NASA/ESA Ulysses. Swift's XRT telescope is able to localize GRBs with much higher accuracy than the IPN network can on its own, and since Swift often follows up on GRB detections from one of the other IPN3 satellites, the XRT localization information is used in this thesis whenever possible. One of the GRBs used does not have an XRT follow up, and so the IPN localization is used. However, even when the IPN localization is not used the spectra information from IPN3 satellites can be used. Considering the BAT's limited energy range to which it is sensitive to it is often advantageous to use the spectral information from another IPN satellite. Below is some information about each of the satellites that provides spectral information to this thesis.

### 5.2.3.1 Konus/Wind

Konus/Wind was launched in 1994 by NASA with its primary purpose being to study solar wind [67]. The Konus instrument on board the satellite is the first Russian scientific instrument aboard an American satellite after space cooperation between the U.S.A. and Russia was resumed in 1987. There are two detectors on the satellite on its top and bottom allowing for isotropic sensitivity to gamma-rays. The energy range in which Konus is sensitive is 10keV to 10MeV.

### 5.2.3.2 Agile

Agile was launched into an equatorial orbit by the Italian Space Agency in 2007 [68] [69]. The on-board instrument, the *Super*AGILE instrument is a hard X-ray imager using a coded mask that is sensitive to photons in the energy range of 15 to 45keV. The best angular resolution of this instrument is 6 arcmin and to complement the hard x-ray instrument there is a complementary gamma-ray imaging detector (GRID), which uses a silicone tracker that is sensitive to gamma-rays in the energy range of 50MeV to 30GeV.

### 5.2.3.3 Suzaku

Suzaku is a Japanese satellite launched into circular earth orbit in 2005. Suzaku has an on board Wide-band all sky Monitor, which is able to submit alerts to GCN [70] [71]. There are four subdetectors that monitor the sky from 50keV to 5MeV, however, no localization information can be given on its own and therefore

relies on IPN3 net to provide the location of a GRB.

### 5.2.3.4 Integral

The last of the satellites used in this thesis is the European Space Agency's International Gamma-Ray Astrophysics Laboratory (INTEGRAL). It was launched in 2002 into earth orbit and has a period of 72 hours. There is a spectrometer on board and an on board imager (IBIS). Both instruments are able to provide images of the gamma ray sky in the 15keV to 10MeV energy range using a coded aperture technique. IBIS has the ability to localize GRBs to within a few arcminutes using on board systems. More information on Integral can be found here [72] [73].

### 5.2.4 Satellite Summary

Below is a summary table of the satellites used in this thesis (see table 5.1).

Table 5.1: Table of Satellite Parameters

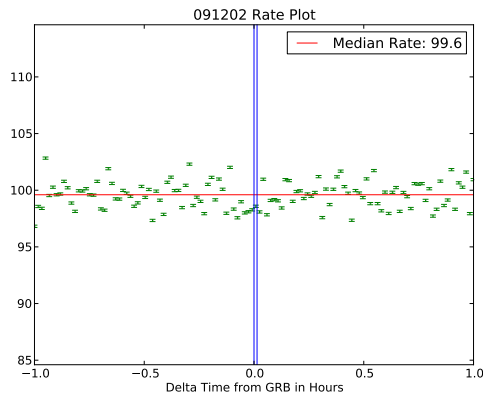
Satellite	Energy Range (keV)	Field of View (sr)	Localizations (arcmin)
Fermi (GBM)	150 - 30000	$4\pi$	60
Fermi (LAT)	30MeV - 300GeV	$\sim \pi$	1-3
Swift (BAT)	15 - 150	2	1-3
Swift (XRT)	0.2 - 10	$4.7 \times 10^{-5}$	$8.3 \times 10^{-2}$
Integral	$15 - 1 \times 10^5$	0.256	2-3
Konus/Wind	$10 - 1 \times 10^5$	$4\pi$	(IPN based)
Suzaku	$50 - 5 \times 10^4$	$4\pi$	(IPN based)
Agile	15 - 45	$4\pi/3$	(IPN based)

### 5.3 The IceCube 59-string GRB catalog

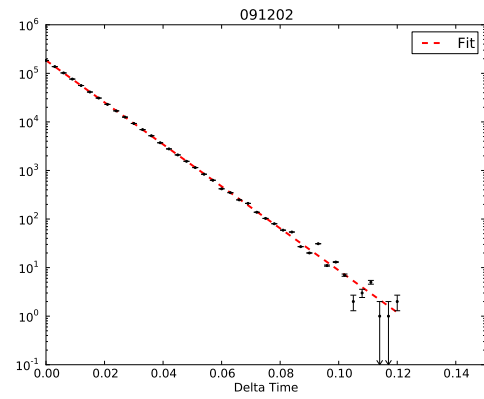
This section will cover the GRBs that are used in this thesis. All GRBs that are detected by one of the satellites are considered for inclusion in this analysis. The analysis presented here is a Northern sky GRB analysis, so the first cut removes all GRBs that have a reported declination in the southern sky. This cut leaves 106 GRBs in the sample. Next, it is checked that there is IceCube data available for GRB times. If there is, the data is checked for stability around the time of the GRB. This check removes an additional 10 GRBs and brings the total number down to 96 GRBs. To check the detector stability during a GRB the timing of the unfiltered events is checked. Stable IceCube data should have a constant rate and the time difference between subsequent events should behave in a Poissonian. In Figure 5.4 the overall rate plot during a GRB can be seen as well as the time difference plot for subsequent events. GRBs that have event rates vary by more than 5Hz would be excluded. Gamma-ray satellite values for GRBs used in this thesis are shown in table 5.3.

#### 5.3.0.1 GRB Neutrino Spectra Calculation

The neutrino spectra in this thesis are calculated using the equations presented in section 2.2.3. In table 5.4 values used to calculate the neutrino spectra as well as the neutrino spectra parameters themselves are presented. If gamma-spectrum parameters are not measured, average values are used for the neutrino spectra calculation [31]. These parameters are listed in tables 5.2. Combining all



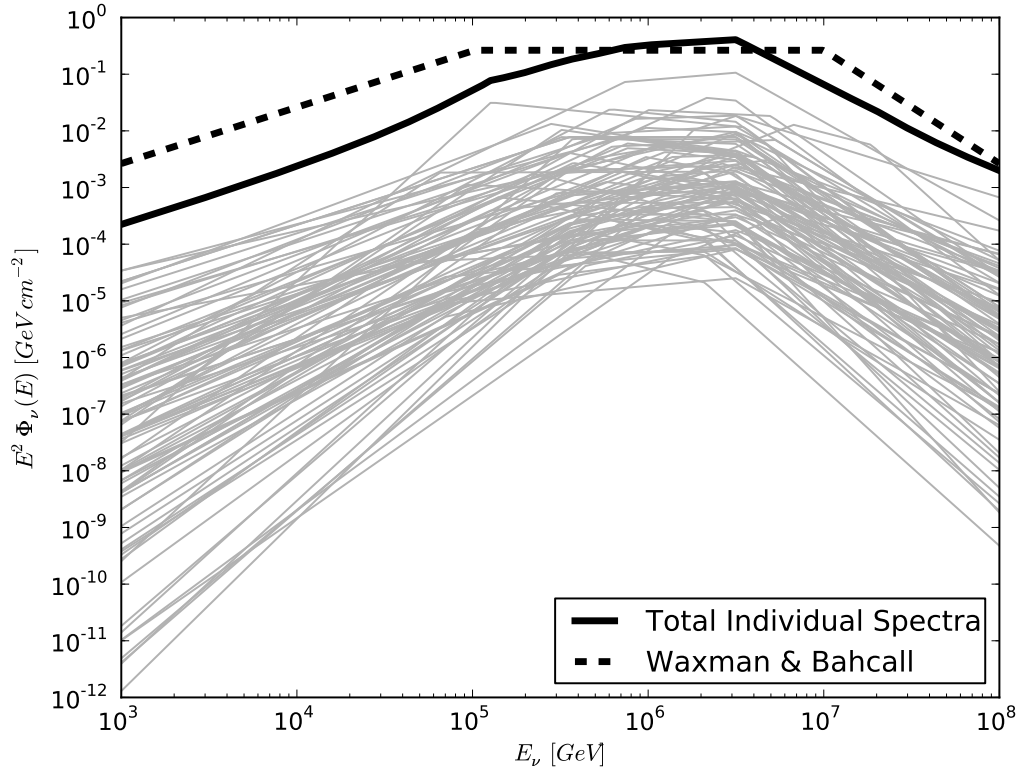
(a) Filter Level Rate



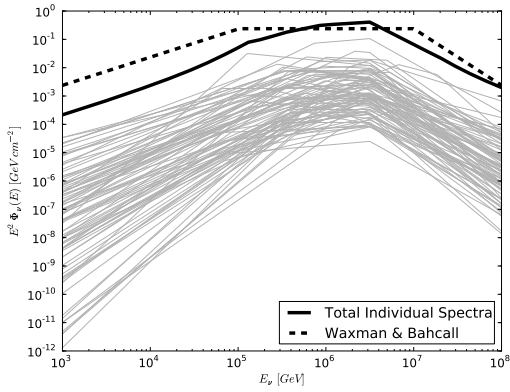
(b) Time Difference

Figure 5.4: Examples of IceCube Stability plots. In panel (a) the filter rate for all IceCube filters during a two hour time window around the GRB is shown. Panel (b) the time difference between subsequent events in the same two hour time window is plotted on a semi-log scale.

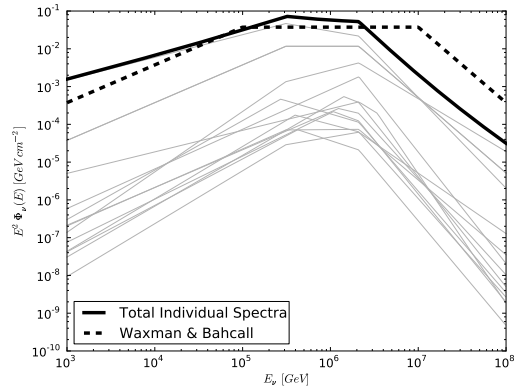
of the information presented so far, the neutrino spectrum for the Bursts used in this analysis can be plotted. Figure 5.5 shows the neutrino spectra for all the bursts used in this thesis, as well as separate plots for the Long Soft Bursts and the Short Hard Bursts.



(a)



(b)



(c)

Figure 5.5: Panel (a) shows the neutrino spectra for all of the GRBs used in this thesis. Panel (b) shows the spectra for Long Soft Bursts while Panel (c) shows the neutrino spectra for Short Hard Bursts. The Waxman & Bahcall benchmark flux is shown as well [1]

Table 5.2: Table of average values

Parameter	Long Soft Burst (LSB)	Short Hard Burst (SHB)	X-ray Flash
Fluence ( $F_\gamma$ )	$10^{-5}$ erg cm $^{-2}$	$10^{-5}$ erg cm $^{-2}$	$10^{-4}$ erg cm $^{-2}$
redshift (z)	2.15	0.5	2.15
$E_{peak}$	200 keV	1000 keV	20 keV
$\alpha_\gamma$	1	1	1
$\beta_\gamma$	2	2	2
$L_{iso}$	$10^{52}$ erg	$10^{51}$ erg	$10^{51}$ erg
$\Gamma_{jet}$	316	316	316
$t_{var}$	0.01 s	0.001 s	0.01 s
$\epsilon_e$	0.1	0.1	0.1
$\epsilon_b$	0.1	0.1	0.1
$f_e$	0.1	0.1	0.1

Table 5.3: General Burst Parameters

GRB	$T_0$	$T_1$	$T_2$	RA	Dec	GRB	$T_0$	$T_1$	$T_2$	RA	Dec
Northern Hemisphere Bursts											
GRB090520B	19:57:53	-0.384	0.256	332.0	43.2	GRB090522	08:15:49	-2.0	20.0	277.7	19.6
GRB090528B	12:22:31	-5.0	120.0	312.2	32.7	GRB090529	14:12:35	-49.0	39.3	212.468	24.459
GRB090529B	07:26:22	-1.792	5.376	231.2	32.2	GRB090529C	13:32:00	-0.002	10.048	162.7	47.3
GRB090530	03:18:18	-12.2	51.8	179.418	26.593	GRB090530B	18:14:24	-3.1	219.0	73.2	13.8
GRB090531	01:45:17	-12.6	29.4	178.655	7.817	GRB090607	05:30:17	0.0	2.5	191.169	44.105
GRB090610	15:33:26	-3.1	3.2	84.2	35.4	GRB090610C	21:12:08	-4.1	8.2	70.4	30.3
GRB090612	14:50:50	-1.024	5.12	81.1	17.8	GRB090616	03:45:42	-0.128	0.512	103.1	-3.7
GRB090617	04:59:59	-0.032	0.6	78.9	15.7	GRB090618	08:28:29	-4.4	213.6	293.995	78.357
GRB090620	09:36:23	-0.003	16.64	237.4	61.2	GRB090621	04:22:43	-6.1	45.06	11.022	61.941
GRB090621B	22:07:25	-0.064	0.148	313.47	69.028	GRB090702	10:40:37	0.0	10.0	175.897	11.502
GRB090703	07:54:02	-2.6	6.7	0.8	9.7	GRB090704	05:47:43	0.0	70.0	208.205	22.79
GRB090708	03:38:15	-10.0	110.0	154.632	26.616	GRB090709	07:38:34	-66.7	102.912	289.927	60.728
GRB090709B	15:07:42	-5.4	35.9	93.522	64.081	GRB090712	03:51:05	-99.1	157.8	70.097	22.525
GRB090713	00:29:28	-4.1	55.3	284.8	-3.3	GRB090715	17:25:39	-0.1	67.8	152.102	10.006
GRB090715B	21:03:14	-11.6	292.3	251.34	44.839	GRB090717B	02:40:32	-0.256	0.128	247.0	23.0
GRB090726	22:42:27	-34.7	47.3	248.68	72.884	GRB090727	22:42:18	-1.3	318.9	315.961	64.925
GRB090728	14:45:45	-5.0	63.2	29.653	41.633	GRB090802	05:39:03	-0.016	0.058	51.0	37.9
GRB090807	15:00:27	-9.5	151.5	273.744	10.266	GRB090807B	19:57:59	-0.64	1.408	326.9	7.2
GRB090809	17:31:14	-1.0	6.4	328.68	-0.084	GRB090809B	23:28:15	0.0	14.3	95.3	0.1
GRB090813	04:10:43	-0.8	8.96	225.779	88.568	GRB090814	00:52:19	-16.4	73.6	239.61	25.631
GRB090814B	01:21:33	0.0	50.0	64.755	60.59	GRB090814C	08:49:41	-0.064	0.192	332.5	58.9
GRB090815	07:12:12	-5.12	24.576	41.7	-2.0	GRB090815B	10:30:42	-7.168	23.552	21.4	53.4
GRB090817	00:51:33	0.0	250.0	63.966	44.129	GRB090820	00:38:16	0.0	60.0	87.7	27.0
GRB090823	16:11:12	0.0	14.848	128.677	60.652	GRB090826	01:37:31	-4.096	9.216	140.6	-0.1

Table 5.3:  $T_0$  – time of satellite trigger,  $T_1$  – time from trigger to beginning of window [s],  $T_2$  – time from trigger to end of window [s], RA – right ascension of burst [°], Dec – declination of burst [°]

Table 5.3: (continued)

GRB	$T_0$	$T_1$	$T_2$	RA	Dec	GRB	$T_0$	$T_1$	$T_2$	RA	Dec
GRB090831	07:36:37	0.0	49.408	145.1	51.0	GRB090902	09:38:05	-0.256	0.896	291.0	53.1
GRB090902B	11:05:08	-0.5	25.0	264.939	27.324	GRB090904	01:01:06	0.0	186.3	100.881	50.204
GRB090910	19:29:49	-7.2	44.0	296.2	72.3	GRB090912	15:50:29	-15.9	160.1	188.043	61.485
GRB090915	15:35:36	-3.0	5.0	238.02	15.488	GRB090916	07:00:44	0.0	68.5	126.582	25.941
GRB090922	12:56:42	0.0	10.24	17.1	74.3	GRB090925	09:20:34	-1.0	20.0	333.2	14.3
GRB090929B	10:09:07	-9.8	371.0	117.72	-0.658	GRB091003	04:35:46	-2.0	26.88	251.52	36.625
GRB091020	21:36:44	-8.7	38.3	175.73	50.978	GRB091024	08:55:58	-15.2	135.8	339.252	56.889
GRB091030	19:52:27	-1.7	40.0	41.67	21.54	GRB091104	08:49:22	-1.5	120.5	208.756	47.411
GRB091126B	09:19:49	-0.016	0.016	47.4	31.5	GRB091128	06:50:35	-24.832	71.425	127.7	1.7
GRB091130B	17:59:04	-4.7	127.4	203.148	34.088	GRB091202	23:10:12	0.0	50.0	138.834	62.55
GRB091208	08:46:00	-0.5	32.8	0.295	65.68	GRB091208B	09:49:57	-0.2	22.3	29.392	16.89
GRB091221	20:52:52	-43.6	41.1	55.798	23.241	GRB100111	04:12:49	-7.5	8.7	247.048	15.551
GRB100115	11:15:19	0.0	0.0	3.367	-0.827	GRB100116	21:31:00	0.0	111.0	305.02	14.45
GRB100117	21:06:19	-0.128	0.3	11.269	-1.595	GRB100122	14:47:37	-2.688	25.984	79.2	-2.7
GRB100131	17:30:58	-0.5	5.5	120.4	16.5	GRB100203	18:31:07	-50.0	60.0	96.225	4.793
GRB100205	04:18:43	-12.6	25.6	141.388	31.741	GRB100206	13:30:05	-0.019	0.124	47.162	13.157
GRB100212	14:07:22	-4.8	134.0	356.418	49.494	GRB100213	22:27:48	-0.7	2.2	349.392	43.379
GRB100213B	22:58:34	-12.7	35.3	124.282	43.448	GRB100216	10:07:00	0.0	0.0	154.259	35.568
GRB100223	02:38:09	-0.01	0.22	104.1	2.8	GRB100302	19:53:06	0.0	67.3	195.515	74.59
GRB100305	09:05:38	-9.2	70.3	168.367	42.404	GRB100316	02:23:00	-1.2	6.7	251.982	71.828
GRB100322B	07:06:18	0.0	0.0	76.489	42.685	GRB100413	17:33:28	-2.0	227.4	266.222	15.834
GRB100413B	08:42:41	-2.0	8.0	356.826	51.27	GRB100414	02:20:21	-1.5	28.9	192.113	8.693
GRB100418	21:10:08	-1.1	7.8	256.363	11.461	GRB100420	05:22:42	-30.0	70.0	296.128	55.769
GRB100423	00:34:59	-12.9	99.1	136.471	21.487	GRB100423B	05:51:26	-2.0	23.6	119.7	5.8
GRB100424	16:32:42	0.0	148.5	209.448	1.539	GRB100427	08:31:55	-4.1	11.3	89.171	-3.461
GRB100503	13:18:04	-51.0	89.0	147.5	4.0	GRB100511	00:49:56	-7.4	52.0	109.29	-4.65

Table 5.3:  $T_0$  – time of satellite trigger,  $T_1$  – time from trigger to beginning of window [s],  $T_2$  – time from trigger to end of window [s], RA – right ascension of burst [°], Dec – declination of burst [°]

Table 5.3: (continued)

GRB	$T_0$	$T_1$	$T_2$	RA	Dec	GRB	$T_0$	$T_1$	$T_2$	RA	Dec
GRB100513	02:07:08	-64.1	44.6	169.612	3.628	GRB100514	18:53:58	0.0	30.8	328.823	29.16
GRB100522	03:45:52	-0.5	40.385	6.987	9.402	GRB100526	16:26:10	-33.2	80.0	230.769	25.632
GRB100528	01:48:04	0.0	24.576	311.141	27.807						

Table 5.3:  $T_0$  – time of satellite trigger,  $T_1$  – time from trigger to beginning of window [s],  $T_2$  – time from trigger to end of window [s], RA – right ascension of burst [°], Dec – declination of burst [°]

Table 5.4: Burst Spectrum Parameters

GRB	$\gamma$ -ray spectrum							$\nu$ spectrum					
	$f_\gamma$	$z$	$\epsilon_\gamma^b$	$E_{min}$	$E_{max}$	$\alpha_\gamma$	$\beta_\gamma$	$f_\nu$	$\epsilon_\nu^b$	$\epsilon_\nu^s$	$\alpha_\nu$	$\beta_\nu$	$\beta_\nu + 2$
Northern Hemisphere Bursts													
090520B	4.5e-07	0.5	1000	0.01	1.0	1.4	2.4	3.59e-16	0.31	2.1	0.6	1.6	3.6
090522A	1.2e-06	2.15	75.8	0.01	1.0	1.03	3.03	6.93e-16	0.93	3.17	0.97	1.97	3.97
090528B	4.65e-05	2.15	172	0.01	1.0	1.1	2.3	6.82e-14	0.41	3.17	0.7	1.9	3.9
090529A	6.8e-07	2.625	200	0.02	0.15	2.0	3.0	9.41e-16	0.27	2.75	-0	1.0	3.0
090529B	3.4e-07	2.15	142	0.01	1.0	0.7	2.0	6.34e-16	0.5	3.17	1.0	2.3	4.3
090529C	3.1e-06	2.15	188	0.01	1.0	0.84	2.1	7.36e-15	0.37	3.17	0.9	2.16	4.16
090530A	1.1e-06	2.15	200	0.02	0.15	1.61	2.61	2.03e-15	0.35	3.17	0.39	1.39	3.39
090530B	5.9e-05	2.15	67	0.01	1.0	0.71	2.42	2.81e-14	1.05	3.17	0.58	2.29	4.29
090531A	1.3e-06	2.15	64.7	0.02	0.15	1.68	3.68	6.12e-16	1.09	3.17	0.32	1.32	3.32
090607A	1.1e-07	2.15	200	0.02	0.15	1.25	2.25	5.03e-16	0.35	3.17	0.75	1.75	3.75
090610A	7.32e-07	2.15	200	0.01	1.0	1.3	2.3	1.02e-15	0.35	3.17	0.7	1.7	3.7
090610C	8.54e-07	2.15	200	0.01	1.0	1.62	2.62	6.94e-16	0.35	3.17	0.38	1.38	3.38
090612A	2.37e-06	2.15	357	0.01	1.0	0.6	1.9	2.03e-14	0.2	3.17	1.1	2.4	4.4
090616A	2.23e-07	2.15	200	0.01	1.0	1.27	2.27	3.27e-16	0.35	3.17	0.73	1.73	3.73
090617A	4.68e-07	0.5	684	0.01	1.0	0.45	2.0	7.77e-16	0.45	2.1	1.0	2.55	4.55
090618A	0.00027	2.15	155.5	0.01	1.0	1.26	2.5	2.75e-13	0.45	3.17	0.5	1.74	3.74
090620A	6.6e-06	2.15	156	0.01	1.0	0.4	2.44	1.38e-14	0.45	3.17	0.56	2.6	4.6
090621A	4.4e-06	2.15	56.0	0.01	1.0	1.1	2.12	1.5e-15	1.26	3.17	0.88	1.9	3.9
090621B	3.71e-07	0.5	321.60	0.01	1.0	0.13	1.57	2.81e-16	0.97	2.1	1.43	2.87	4.87
090702A	1.5e-07	2.15	200	0.02	0.2	1.0	2.0	1.02e-15	0.35	3.17	1.0	2.0	4.0
090703A	6.8e-07	2.15	200	0.01	1.0	1.72	2.72	4.74e-16	0.35	3.17	0.28	1.28	3.28
090704A	5.8e-06	2.15	233.7	0.01	1.0	1.13	3.13	1.33e-14	0.3	3.17	0.87	1.87	3.87
090705A	1e-05	0.5	1000	0.01	10.0	1.0	2.0	1.25e-14	0.35	3.17	1.0	2.0	4.0

Table 5.4:  $f_\gamma$  [erg cm<sup>-2</sup>],  $\epsilon_\gamma^b$  [KeV],  $E_{min}$  [KeV],  $E_{max}$  [KeV],  $f_\nu$  [GeV<sup>-1</sup> cm<sup>-2</sup>],  $\epsilon_\nu^b$  [PeV],  $\epsilon_\nu^s$  [PeV]. The parameters  $f_\gamma$  and  $f_\nu$  are the fluxes at  $\epsilon_\gamma$  and  $\epsilon_\nu$  of the gamma-ray and neutrino spectrum, respectively.

Table 5.4: (continued)

GRB	$\gamma$ -ray spectrum							$\nu$ spectrum					
	$f_\gamma$	$z$	$\epsilon_\gamma^b$	$E_{min}$	$E_{max}$	$\alpha_\gamma$	$\beta_\gamma$	$f_\nu$	$\epsilon_\nu^b$	$\epsilon_\nu^s$	$\alpha_\nu$	$\beta_\nu$	$\beta_\nu + 2$
090708A	4e-07	2.15	47.5	0.01	1.0	1.29	3.29	9.64e-17	1.48	3.17	0.71	1.71	3.71
090709A	9.1e-05	1.0	298	0.02	3.0	0.85	2.7	4.6e-14	0.59	4.99	0.3	2.15	4.15
090709B	1.3e-06	2.15	130	0.01	1.0	1.01	3.01	1.69e-15	0.54	3.17	0.99	1.99	3.99
090712A	4.2e-06	2.15	505	0.01	1.0	0.68	2.68	6.56e-14	0.14	3.17	1.32	2.32	4.32
090713A	3.7e-06	2.15	99	0.01	1.0	0.34	2.34	6.95e-15	0.71	3.17	1.66	2.66	4.66
090715A	3.5e-06	2.15	1658	0.02	10.0	1.13	3.13	2.72e-14	0.04	3.17	0.87	1.87	3.87
090715B	9.3e-06	3.0	134	0.02	2.0	1.1	3.1	2.29e-14	0.33	2.49	0.9	1.9	3.9
090717B	4.83e-07	0.5	1000	0.01	1.0	1.02	2.02	8.25e-16	0.31	2.1	0.98	1.98	3.98
090726A	8.6e-07	2.15	200	0.02	0.15	2.25	3.25	5.4e-16	0.35	3.17	0.25	0.75	2.75
090727A	1.4e-06	2.15	200	0.02	0.15	1.24	2.24	6.58e-15	0.35	3.17	0.76	1.76	3.76
090728A	1e-06	2.15	200	0.02	0.15	2.05	3.05	8.25e-16	0.35	3.17	0.05	0.95	2.95
090802A	6.5e-07	2.15	283	0.01	1.0	0.42	2.4	3.37e-15	0.25	3.17	0.6	2.58	4.58
090807A	2.2e-06	2.15	200	0.02	0.15	2.25	3.25	1.38e-15	0.35	3.17	0.25	0.75	2.75
090807B	1.02e-06	2.15	37	0.01	1.0	0.6	2.4	2.06e-16	1.9	3.17	0.6	2.4	4.4
090809A	3.4e-07	2.737	200	0.02	0.15	1.34	2.34	2.26e-15	0.25	2.67	0.66	1.66	3.66
090809B	2.26e-05	2.15	198	0.01	1.0	0.85	2.02	6.04e-14	0.36	3.17	0.98	2.15	4.15
090813A	3.5e-06	2.15	161	0.01	1.0	1.25	2.0	4.84e-15	0.44	3.17	1.0	1.75	3.75
090814A	1.3e-06	2.15	200	0.02	0.15	1.81	2.81	1.6e-15	0.35	3.17	0.19	1.19	3.19
090814B	1e-05	2.15	200	0.02	0.2	1.0	2.0	6.78e-14	0.35	3.17	1.0	2.0	4.0
090814C	6.6e-07	0.5	790	0.01	1.0	0.39	2.39	1.78e-15	0.39	2.1	1.61	2.61	4.61
090815A	3.4e-06	2.15	200	0.01	1.0	1.5	2.5	3.36e-15	0.35	3.17	0.5	1.5	3.5
090815B	5.05e-06	2.15	15.1	0.01	1.0	1.82	2.7	6.89e-16	3.17	4.67	0.3	2.3	4.3
090817A	7.3e-06	2.15	115	0.01	1.0	1.1	2.2	6.63e-15	0.61	3.17	0.8	1.9	3.9
090820A	6.6e-05	2.15	215	0.01	1.0	0.69	2.61	1.71e-13	0.33	3.17	0.39	2.31	4.31
090823A	8.9e-06	2.15	188	0.02	2.0	0.49	2.49	2.67e-14	0.37	3.17	1.51	2.51	4.51

Table 5.4:  $f_\gamma$  [erg  $cm^{-2}$ ],  $\epsilon_\gamma^b$  [KeV],  $E_{min}$  [KeV],  $E_{max}$  [KeV],  $f_\nu$  [GeV $^{-1}$   $cm^{-2}$ ],  $\epsilon_\nu^b$  [PeV],  $\epsilon_\nu^s$  [PeV]. The parameters  $f_\gamma$  and  $f_\nu$  are the fluxes at  $\epsilon_\gamma$  and  $\epsilon_\nu$  of the gamma-ray and neutrino spectrum, respectively.

Table 5.4: (continued)

GRB	$\gamma$ -ray spectrum							$\nu$ spectrum					
	$f_\gamma$	$z$	$\epsilon_\gamma^b$	$E_{min}$	$E_{max}$	$\alpha_\gamma$	$\beta_\gamma$	$f_\nu$	$\epsilon_\nu^b$	$\epsilon_\nu^s$	$\alpha_\nu$	$\beta_\nu$	$\beta_\nu + 2$
090826A	1.26e-06	2.15	172	0.01	1.0	0.96	2.96	2.62e-15	0.41	3.17	1.04	2.04	4.04
090831A	1.66e-05	2.15	399.6	0.01	1.0	1.52	1.96	3.84e-14	0.18	3.17	1.04	1.48	3.48
090831B	1e-05	0.5	1000	0.01	10.0	1.0	2.0	1.25e-14	0.35	3.17	1.0	2.0	4.0
090902A	2.11e-06	0.5	388	0.01	1.0	0.3	2.05	1.59e-15	0.8	2.1	0.95	2.7	4.7
090902B	0.000374	1.822	775	0.01	0.05	0.696	3.85	2.25e-12	0.11	3.53	0.85	2.304	4.304
090904A	3e-06	2.15	200	0.02	0.15	2.01	3.01	2.63e-15	0.35	3.17	0.01	0.99	2.99
090910A	9.2e-06	2.15	274.8	0.01	1.0	0.9	2.0	3.73e-14	0.26	3.17	1.0	2.1	4.1
090912A	4.5e-06	2.15	69.3	0.02	0.15	1.66	3.66	2.3e-15	1.02	3.17	0.34	1.34	3.34
090916A	9.5e-07	2.15	200	0.02	0.15	1.42	2.42	2.77e-15	0.35	3.17	0.58	1.58	3.58
090922A	1.14e-05	2.15	139.3	0.01	1.0	0.77	2.28	1.68e-14	0.51	3.17	0.72	2.23	4.23
090925A	9.46e-06	2.15	156	0.01	1.0	0.6	1.91	2.32e-14	0.45	3.17	1.09	2.4	4.4
090929B	1.16e-05	2.15	282	0.02	1.0	0.41	1.82	8.57e-14	0.25	3.17	1.18	2.59	4.59
091003A	3.76e-05	0.8969	486.2	0.01	1.0	1.13	2.64	2.4e-14	0.4	5.26	0.36	1.87	3.87
091020A	1e-05	2.15	47.9	0.01	1.0	0.2	1.7	4.38e-15	1.47	3.17	1.3	2.8	4.8
091024A	1e-05	1.092	200	0.01	0.4	1.5	2.5	1.92e-15	0.8	4.77	0.5	1.5	3.5
091029A	2.4e-06	2.752	61.4	0.02	0.15	1.88	3.88	1.74e-15	0.81	2.66	0.12	1.12	3.12
091030A	3.03e-05	2.15	507	0.01	1.0	0.88	2.2	2.53e-13	0.14	3.17	0.8	2.12	4.12
091104A	7.7e-07	2.15	200	0.02	0.15	1.74	2.74	1.08e-15	0.35	3.17	0.26	1.26	3.26
091109A	1.6e-06	3.076	200	0.02	0.15	1.31	2.31	1.58e-14	0.21	2.45	0.69	1.69	3.69
091126B	2.2e-07	0.5	731	0.01	1.0	0.23	2.23	5.33e-16	0.42	2.1	1.77	2.77	4.77
091127A	1.87e-05	0.49034	36	0.01	1.0	1.27	2.2	3.65e-16	6.69	8.74	0.8	2.8	4.8
091128A	3.76e-05	2.15	178.8	0.01	1.0	0.99	3.9	5.41e-14	0.39	3.17	0.9	2.01	4.01
091130A	1e-05	0.5	1000	0.01	10.0	1.0	2.0	1.25e-14	0.35	3.17	1.0	2.0	4.0
091130B	1.3e-06	2.15	200	0.02	0.15	2.15	3.15	9.32e-16	0.35	3.17	0.15	0.85	2.85
091202A	1e-05	2.15	200	0.02	0.2	1.0	2.0	6.78e-14	0.35	3.17	1.0	2.0	4.0

Table 5.4:  $f_\gamma$  [erg  $cm^{-2}$ ],  $\epsilon_\gamma^b$  [KeV],  $E_{min}$  [KeV],  $E_{max}$  [KeV],  $f_\nu$  [GeV $^{-1}$   $cm^{-2}$ ],  $\epsilon_\nu^b$  [PeV],  $\epsilon_\nu^s$  [PeV]. The parameters  $f_\gamma$  and  $f_\nu$  are the fluxes at  $\epsilon_\gamma$  and  $\epsilon_\nu$  of the gamma-ray and neutrino spectrum, respectively.

Table 5.4: (continued)

GRB	$\gamma$ -ray spectrum							$\nu$ spectrum					
	$f_\gamma$	$z$	$\epsilon_\gamma^b$	$E_{min}$	$E_{max}$	$\alpha_\gamma$	$\beta_\gamma$	$f_\nu$	$\epsilon_\nu^b$	$\epsilon_\nu^s$	$\alpha_\nu$	$\beta_\nu$	$\beta_\nu + 2$
091208A	6.2e-06	2.15	314	0.02	2.0	0.24	2.24	3.99e-14	0.22	3.17	1.76	2.76	4.76
091208B	5.8e-06	1.0633	144.20	0.01	1.0	1.44	2.32	1.08e-15	1.14	4.83	0.68	1.56	3.56
091221A	1.38e-05	2.15	207	0.01	1.0	0.69	2.3	3.81e-14	0.34	3.17	0.7	2.31	4.31
100111A	1.5e-06	2.15	200	0.01	1.0	1.66	2.66	1.15e-15	0.35	3.17	0.34	1.34	3.34
100115A	1e-05	0.5	1000	0.02	0.15	1.0	2.0	9.39e-14	0.35	3.17	1.0	2.0	4.0
100116A	5.7e-05	2.15	968	0.02	10.0	0.96	2.96	3.69e-13	0.07	3.17	1.04	2.04	4.04
100117A	4.1e-07	0.5	287	0.01	1.0	0.14	2.14	2.32e-16	1.08	2.1	1.86	2.86	4.86
100122A	1e-05	2.15	45.6	0.01	1.0	0.98	2.31	2.51e-15	1.54	3.17	0.69	2.02	4.02
100130B	1.342e-05	2.15	208.00	0.01	1.0	1.22	3.22	2.26e-14	0.34	3.17	0.78	1.78	3.78
100131A	7.723e-06	2.15	132.10	0.01	1.0	0.63	2.21	1.19e-14	0.53	3.17	0.79	2.37	4.37
100203A	1e-05	0.5	1000	0.02	0.15	1.0	2.0	9.39e-14	0.35	3.17	1.0	2.0	4.0
100205A	4e-07	2.15	200	0.02	0.15	1.6	2.6	7.56e-16	0.35	3.17	0.4	1.4	3.4
100206A	9.3e-07	0.5	506	0.01	1.0	0.09	2.35	9.68e-16	0.61	2.1	0.65	2.91	4.91
100212A	3.81e-07	2.15	159.30	0.01	1.0	1.62	3.62	2.58e-16	0.44	3.17	0.38	1.38	3.38
100213A	2.7e-07	2.15	200	0.02	0.15	1.34	2.34	9.68e-16	0.35	3.17	0.66	1.66	3.66
100213B	1e-05	2.15	39.1	0.02	0.15	2.04	4.04	3.22e-15	1.8	3.17	0.04	0.96	2.96
100216A	4.7e-08	0.5	1000	0.02	0.15	0.6	1.6	1.42e-15	0.35	3.17	1.4	2.4	4.4
100223A	1.42e-06	0.5	1143	0.01	1.0	0.31	2.31	7.84e-15	0.27	2.1	1.69	2.69	4.69
100302A	3.1e-07	4.813	200	0.02	0.15	1.72	2.72	3.6e-15	0.1	1.72	0.28	1.28	3.28
100305A	1.5e-06	2.15	200	0.02	0.15	1.27	2.27	6.49e-15	0.35	3.17	0.73	1.73	3.73
100316A	8.2e-07	2.15	200	0.02	0.15	1.46	2.46	2.16e-15	0.35	3.17	0.54	1.54	3.54
100413A	2.66e-05	3.9	446	0.01	10.0	1.01	3.01	4.17e-13	0.07	2.03	0.99	1.99	3.99
100413B	1e-05	0.5	1000	0.01	10.0	1.0	2.0	1.25e-14	0.35	3.17	1.0	2.0	4.0
100414A	4.88e-05	1.368	612	0.1	1.0	0.56	3.05	1.98e-13	0.2	4.21	0.05	2.44	4.44
100418A	3.4e-07	0.624	200	0.02	0.15	2.16	3.16	3.42e-17	1.33	6.14	0.16	0.84	2.84

Table 5.4:  $f_\gamma$  [erg  $cm^{-2}$ ],  $\epsilon_\gamma^b$  [KeV],  $E_{min}$  [KeV],  $E_{max}$  [KeV],  $f_\nu$  [GeV $^{-1}$   $cm^{-2}$ ],  $\epsilon_\nu^b$  [PeV],  $\epsilon_\nu^s$  [PeV]. The parameters  $f_\gamma$  and  $f_\nu$  are the fluxes at  $\epsilon_\gamma$  and  $\epsilon_\nu$  of the gamma-ray and neutrino spectrum, respectively.

Table 5.4: (continued)

GRB	$\gamma$ -ray spectrum							$\nu$ spectrum					
	$f_\gamma$	$z$	$\epsilon_\gamma^b$	$E_{min}$	$E_{max}$	$\alpha_\gamma$	$\beta_\gamma$	$f_\nu$	$\epsilon_\nu^b$	$\epsilon_\nu^s$	$\alpha_\nu$	$\beta_\nu$	$\beta_\nu + 2$
100420A	5.7e-07	2.15	200	0.02	0.15	1.17	2.17	3.26e-15	0.35	3.17	0.83	1.83	3.83
100423A	4.8e-05	2.15	621	0.02	2.0	0.5	2.15	5.93e-13	0.11	3.17	0.85	2.5	4.5
100423B	1.226e-05	2.15	1034	0.01	1.0	0.83	3.15	2.41e-13	0.07	3.17	0.15	2.17	4.17
100424A	1.5e-06	2.15	200	0.02	0.15	1.83	2.83	1.77e-15	0.35	3.17	0.17	1.17	3.17
100427A	3.01e-06	2.15	121.0	0.01	1.0	1.02	3.02	3.48e-15	0.58	3.17	0.98	1.98	3.98
100503A	1.23e-05	2.15	211.60	0.01	1.0	0.85	2.24	3.14e-14	0.33	3.17	0.76	2.15	4.15
100511A	7.08e-06	2.15	946.6	0.01	1.0	1.3	2.43	5.01e-14	0.07	3.17	0.57	1.7	3.7
100513A	1.4e-06	4.772	200	0.02	0.15	1.62	2.62	2.04e-14	0.1	1.73	0.38	1.38	3.38
100514A	4e-07	2.15	200	0.02	0.15	1.97	2.97	3.73e-16	0.35	3.17	0.03	1.03	3.03
100522A	5.2e-06	2.15	138	0.01	1.0	1.81	3.81	2.53e-15	0.51	3.17	0.19	1.19	3.19
100526A	2.5e-06	2.15	200	0.02	0.15	1.83	2.83	2.96e-15	0.35	3.17	0.17	1.17	3.17
100528A	2.77e-05	2.15	316.5	0.01	1.0	1.16	1.99	9.68e-14	0.22	3.17	1.01	1.84	3.84

Table 5.4:  $f_\gamma$  [erg  $cm^{-2}$ ],  $\epsilon_\gamma^b$  [KeV],  $E_{min}$  [KeV],  $E_{max}$  [KeV],  $f_\nu$  [GeV $^{-1}$   $cm^{-2}$ ],  $\epsilon_\nu^b$  [PeV],  $\epsilon_\nu^s$  [PeV]. The parameters  $f_\gamma$  and  $f_\nu$  are the fluxes at  $\epsilon_\gamma$  and  $\epsilon_\nu$  of the gamma-ray and neutrino spectrum, respectively.

## Chapter 6

### Analysis Techniques

This chapter is divided into two parts. The first part focuses on the event selection technique, while the second part focuses on the analysis technique used.

#### 6.1 Event selection

IceCube had an event rate of  $\sim 2000\text{Hz}$  in the 59 string configuration. The neutrino expectation for this configuration is  $\sim 300$  atmospheric neutrino events per day and therefore event selection is very important. This is accomplished in three cut stages. The first of which is described in Chapter 3.4.5 (the online filter), with the second stage being described in Chapter 7.2.1 (level 3 pre-selection cuts). The final cut stage uses a Boosted Decision Tree (BDT), which will be described here. For information on how the BDT was used in this analysis please see Chapter 7.5. The information about Boosted Decision trees found in this section is taken from [74], [75] and [76]. For this analysis a Boosted Decision Tree (BDT) was used to separate signal from background. The BDT is a supervised machine learning algorithm used to classify events as background or signal like. The underlying mechanism used for separating signal from background is the Decision Tree. In a BDT a misclassified event in the first Decision Tree will have its weight boosted. This procedure is repeated until a selected maximum number of trees (the forest) is trained.

## 6.2 Decision Trees

Decision Trees work by picking cuts from a provided list of classification variables. The start is a Root node that contains all of the training events. The decision tree attempts to split signal and background sets in the root node as best as it can. It picks the classification variable that best accomplishes that goal, and does the same for the 2 resulting nodes (the left and right child). It continues this process until it either runs out of data, a node reaches a previously specified purity or the tree reaches a specified maximum depth. This method is powerful, however, it is also unstable. That is to say that small changes in the training sample will change the output significantly. This problem can be reduced by training many decision trees with different training sets and then passing events through all of the trained trees and assigning a score to it based on the average result. This method is called the random forest method and although better than just training a single decision tree is still inferior to the BDT method.

### 6.2.1 Decision Trees technical details

The key issue with a Decision tree is to define a criterion that describes the goodness of separation between signal and background events at each split node. Let us assume that  $W_s$  are the weights of the signal events and  $W_b$  are the weights of the background events. In that case the purity of the sample at any given node is described as:

$$P = \frac{\sum_s W_s}{\sum_s W_s + \sum_b W_b} \quad (6.1)$$

For a given node we can define the impurity,  $G_{ini}$ , as follows:

$$G_{ini} = \left( \sum_{i=1}^n W_i \right) P (1 - P) \quad (6.2)$$

$n$  is the number of events on the node in question. It is important to note that  $P(1 - P) = 0$  for a node that contains only background or signal events. It follows that  $G_{ini} = 0$  for a pure sample. The goal is to split a parent node into the best separated child nodes and hence we want to maximize the quantity:

$$G_{ini_{father}} - G_{ini_{leftchild}} - G_{ini_{rightchild}} \quad (6.3)$$

Finally if a node has a purity greater than  $\frac{1}{2}$  it is said to be a signal node, otherwise it is called a background node. Events that need to be classified get passed through a trained Decision tree and get a score of  $-1$  if they land on a background node and a score of  $1$  if they land on a signal node. In the above mentioned random forest the event to be classified would get passed through all of the trained trees and depending on how many times it lands on signal/background nodes it would get a score somewhere between  $-1$  and  $1$ , with scores closer to  $1$  being more signal like. Boosting algorithms can improve the performance and help with the stability of a decision tree and will be talked about in the next section.

### 6.3 Boosting Algorithms

Boosting algorithms can be applied to any machine learning scheme and in this case are applied to decision trees. The general idea behind boosting, is to give events that were misclassified in a given decision tree a higher weight in the next

decision tree. This causes the next decision tree to try harder to classify events correctly that did not get classified correctly in the previous tree. The process is repeated until a user specified number of trees is reached and a final event weight is calculated from the average of all the trees. Some common boosting algorithms are AdaBoost,  $\varepsilon$ -Boost,  $\varepsilon$ -LogitBoost and  $\varepsilon$ -HingeBoost. The analysis in this thesis uses the AdaBoost algorithm and the following section will focus on that boosting algorithm.

### 6.3.1 AdaBoost

Let there be  $N$  total events in the training sample each with weight  $w_i$ . Let the weights be normalized such that  $\sum_i W_i = 1$ . Furthermore lets assume that the event classification variables are  $c_i$  for each event. Since we are dealing with a supervised learning algorithm we need to classify each event as signal or background. So let  $y_i = 1$  if the event is a signal event and  $y_i = -1$  if the event is a background event. For the following calculations we need to define two more things:

1.  $T_m(c_i) = 1$  if the set of classification variables causes the  $i$ 'th event to land on a signal node of the  $m$ 'th tree.  $T_m(c_i) = -1$  if that set of classification variables causes the  $i$ 'th event to land on a background node of the  $m$ 'th tree.
2.  $I(y_i \neq T_m(c_i)) = 1$  if  $y_i \neq T_m(c_i)$  and 0 if  $y_i = T_m(c_i)$ .

For the  $m$ 'th tree in our forest lets define:

$$err_m = \frac{\sum_{i=1}^N w_i I(y_i \neq T_m(c_i))}{\sum_{i=1}^N w_i} \quad (6.4)$$

Then calculating:

$$\alpha_m = \beta \times \ln \left( \frac{1 - err_m}{err_m} \right) \quad (6.5)$$

$\beta$  is a constant factor used in the AdaBoost method. With the default being  $\beta = 1$ .

The event weights are then updated in the following way:

$$w_{(m+1)_i} = w_{m_i} e^{-\alpha_m I(y_i \neq T_m(c_i))} \quad (6.6)$$

Here  $w_{(m+1)_i}$  is the weight of the  $i$ 'th event for the  $(m + 1)$ 'th tree. The  $i$ 'th event weight only gets updated for the  $m + 1$  tree if it gets misclassified in the  $m$ 'th tree.

After reweighing all misclassified events the weights need to be re-normalized:

$$w_i \rightarrow \frac{w_i}{\sum_{i=1}^N w_i} \quad (6.7)$$

Finally an event with classification variables  $c$  gets a score assigned according to:

$$T(c) = \sum_{m=1}^M \alpha_m T_m(c) \quad (6.8)$$

which is a weighted sum of the weighted scores from the individual trees. The advantage of the boosting algorithm is that a few odd events in the training sample will not effect the outcome as much as in the decision tree, and hence improves stability. Actual IceCube performance of this technique will be discussed in the specific analysis sections of Chapter 7.5. Figure 6.1 is a visual representation of a BDT.

## 6.4 Unbinned Likelihood Method

For a more detailed description of the unbinned likelihood method please see [78]. In the previous section I described a method to apply quality cuts to the data

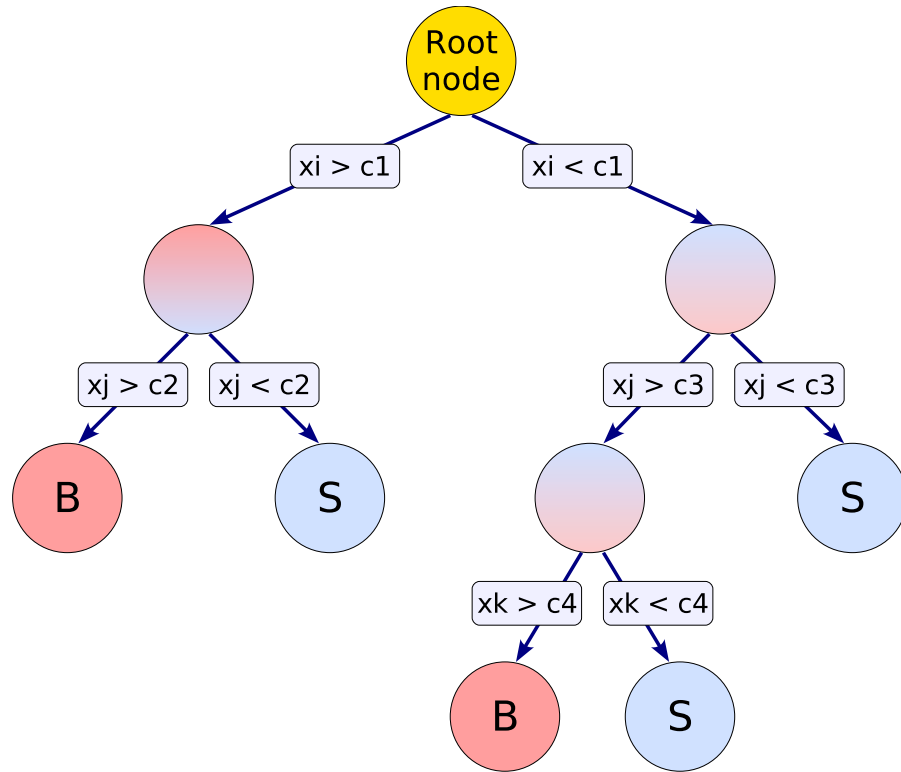


Figure 6.1: Schematic view of a decision tree taken from [77]. This schematic shows the splitting of events starting at the Root node. At each stage a cut is applied that splits the events in the node into signal and background. The algorithm chooses the best cut variable at each stage and cuts can be used more than once or not at all. The leaf nodes at the bottom are classified as either signal or background depending on if the majority of events on that node are signal or background events. Events that were misclassified by the training of the decision tree are given a higher weight and therefore the next decision tree places higher priority on classifying those events correctly, which is known as boosting.

that is produced by IceCube. After applying a BDT cut the resulting dataset is the starting point for the unbinned likelihood method.

In contrast to a binned method where only events that are within a defined box around a GRB are kept, the unbinned likelihood method does not make such a cut and instead uses PDFs to evaluate the probability of an event belonging to the background or signal population. The method requires to define a signal  $S(\vec{x})$  and a background  $B(\vec{x})$  PDF. In this analysis there are 3 PDFs used, space, time and energy. These PDFs are described in detail in the analysis section (see 7.6).

The total signal PDFs of all the GRBs are combined using a simple sum:

$$S_{tot}(\vec{x}_i) = \sum_{j=1}^{N_{GRBs}} S_j(\vec{x}_i) \quad (6.9)$$

here  $S_j(\vec{x}_i)$  is the signal PDF for the  $j$ th GRB. The background has to be estimated for each GRB separately since there are asymmetries in the IceCube detector in both Azimuth and Zenith. This is accomplished by taking all of the off-time data to estimate the background in detector coordinates. The event rate does vary during the season but this effect is ignored since it is very small, and is accounted for in the systematic study. The PDFs are then combined in an extended log-likelihood function ([78]).

In the standard method of maximum likelihood the probability density of  $x$ ,  $P(x; a)$ , is normalized to 1:

$$\int P(x; a) dx = 1 \quad (6.10)$$

The extended maximum likelihood method relaxes this requirement and instead of the function  $P(x; a)$  one uses the function  $Q(x; a)$  with an unfixed normalization.

This means that in some increasing or decreasing  $Q(x; a)$  in some regions of  $x$  increases or decreases the probability of events occurring in that region. This means that  $Q(x; a)$  is normalized to the expected number of events  $n_t$ . In the case of the GRB analysis this would be the total number of events expected inside the total GRB time window. Hence the normalization is:

$$\int Q(x; a)dx = n_t \quad (6.11)$$

This method works better than the standard maximum likelihood method if the number of events is unknown a priori. Hence this method is used in experiments where data is taken over some period of time and events will in some way occur at random inside that time window, and therefore it is the appropriate method to use for a GRB analysis. Incorporating the expected number of events into the Maximum likelihood function can be accomplished by multiplying the standard maximum likelihood function by the corresponding Poisson probability:

$$L = e^{-n_t} \frac{n_t^N}{N!} \times \prod_{i=1}^N P(x_i; a) \quad (6.12)$$

Taking the logarithm of both sides and ignoring the 'N!' term because it does not depend on  $a$ :

$$\ln(L) = -n_t + N\ln(n_t) + \sum_{i=1}^N \ln(P(x_i; a)) \quad (6.13)$$

$$= -n_t + \sum_{i=1}^N \ln(n_t P(x_i; a)) \quad (6.14)$$

$$= -n_t + \sum_{i=1}^N \ln(Q(x; a)) \quad (6.15)$$

which is the extended maximum likelihood function.

The above calculation is independent of the actual PDFs involved. At this point the

relevant PDFs need to be used to define a signal and a background only hypothesis. The actual PDFs will be described in 7.6 and for now  $S_i$  is the signal PDF and  $B_i$  is the background PDF.  $n_b$  is the expected number of background events while  $n_s$  is the number of signal events in the time window and is the variable we want to minimize. The background only hypothesis gives:

$$Q(x; a) = n_b B_i \quad (6.16)$$

and

$$n_t = n_b \quad (6.17)$$

For the signal and background case:

$$Q(x; a) = n_s S_i + n_b B_i \quad (6.18)$$

and

$$n_t = n_b + n_s \quad (6.19)$$

Using these equations we can define a likelihood function for the signal and null hypothesis:

$$\ln(L) = -n_b - n_s + \sum_{i=1}^N \ln(n_s S_i + n_b B_i) \quad (6.20)$$

$$\ln(L_0) = -n_b + \sum_{i=1}^N \ln(n_b B_i) \quad (6.21)$$

From these equations a test statistic can be defined as:

$$\lambda = \ln\left(\frac{L}{L_0}\right) = \ln(L) - \ln(L_0) \quad (6.22)$$

$$= -n_s + \sum_{i=1}^N (\ln(n_s S_i + n_b B_i) - \ln(n_b B_i)) \quad (6.23)$$

and hence:

$$\lambda = -n_s + \sum_{i=1}^N \ln\left(\frac{n_s S_i}{n_b B_i} + 1\right) \quad (6.24)$$

This is the test statistic that is evaluated for data and minimized to find the optimal value of  $n_s$ . To determine the significance of a particular test statistic value, real data is scrambled in time and  $10^9$  trials are performed for the background only case. From the resulting distribution of  $\lambda$ , significance levels can be defined (see Figure 7.8 for a plot of the Test Statistic calculated in this thesis).

## Chapter 7

### Northern Hemisphere Search

This chapter will outline an analysis procedure to search for neutrinos in coincidence with the 96 northern hemisphere bursts that happened during good IC59 runs, as defined in Chapter 5.3. The data that was taken within 2 hours of a GRB is first set aside, or blinded, while data taken throughout the rest of the year is used to characterize the expected background and develop quality cuts. The on-time data is finally unblinded and analyzed with an unbinned likelihood method, described in section 6.4. No neutrinos were found on source and in time with a GRB and hence a limit is calculated.

#### 7.1 GRB Triggers

There are 96 northern hemisphere bursts that happened during the IC59 run that had good IceCube data. There were an additional 9 bursts that happened during times the detector was off (2), taking calibration data (2), or was producing unstable data (5). The on-time window for each GRB is defined as the time between the first time reported by any satellite ( $T_{start}$ ) and the last reported time ( $T_{stop}$ ). Any run that has a start or stop time within 2 hours of either  $T_{start}$  or  $T_{stop}$  is set aside and is considered blinded. For the analysis the GRB window is padded with Gaussian tails that have a minimum  $1-\sigma$  value of 2 seconds and a maximum  $1-\sigma$

value of 20 seconds. The normal  $1\text{-}\sigma$  value is chosen to be  $T_{stop} - T_{start}$ . The time window is then cut off after  $2\sigma$  and any events that fall outside that range are not considered. The padding is done to allow for small timing errors and to make the analysis of very short GRBs ( $\sim 0.1$  seconds) have a more meaningful time window.

## 7.2 IceCube Data

As mentioned in section 3.4.5. this analysis uses data from 2 IceCube filters. It turns out that just taking the data right around a GRB to characterize the background of that GRB is not enough at harder cut levels and so the 2 hours around the GRB are kept blind and the rest of the year is used to help characterize the background. For this study only good runs are used and the first 3 days of data from each month are set aside to be used as the background dataset for training the Boosted Decision Tree (section 6.1). With runs around GRBs blinded, bad runs eliminated and the first 3 days of data for each month set aside we are left with 276 days of lifetime for this background sample.

### 7.2.1 Pre-selection Cuts

Considering that the data volume produced by IceCube is very large the computer resources are not available to process all of the data to Analysis level. This means that some pre-selection cuts need to be made in order to reduce the amount of data that gets processed to Level 3. These cuts are:

- $\text{LLHZenith} \geq 80 \ \&\& \ \text{MPEFitRlogl} \leq 9 \ \&\& \ \text{MPEFitLdir} \geq 100$

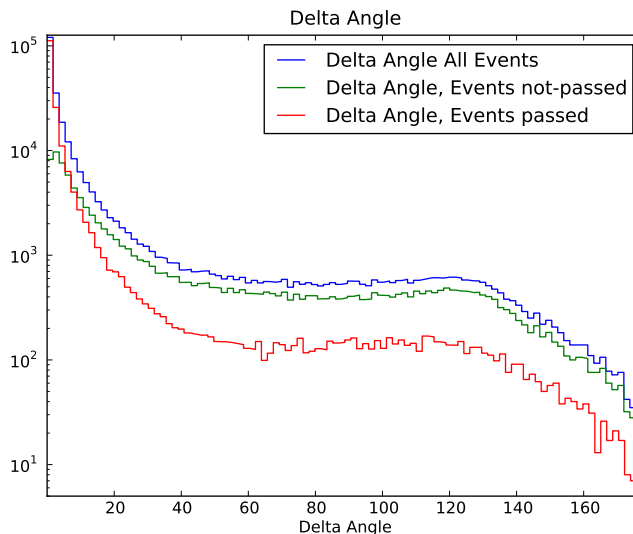


Figure 7.1: This figure shows a histogram event direction differences between the true muon direction and the reconstructed one (in degrees). This plot is created using signal simulation.

- Topological Trigger cut (see section 4.7).

These cuts reduce the total data volume by a factor of 30 removing mis-reconstructed muons while keeping well reconstructed events. Figure 7.1 shows the angle difference of the reconstructed direction of an event with the true muon direction for neutrino simulation. Events that do not pass the pre-selection cuts do not in general have good reconstructed directions. A summary of the effect of these cuts is shown in table 7.1. After the pre-selection cuts more sophisticated cutting methods are employed. A boosted decision tree is trained to further separate signal from background (see section 6.1 for theoretical details and section 7.5 for the implementation in this analysis).

### 7.3 Simulation

Neutrinos for each GRB are simulated using the Monte Carlo chain described in section 3.7. Neutrinos are simulated with an  $E^{-1}$  spectrum. This spectrum is hard enough that the neutrino events can be reweighed to produce each GRB's individual neutrino spectrum. Atmospheric muons are simulated as well and are used to check the performance of the BDT, however, this simulation is not used in this analysis directly. An independent all-sky neutrino simulation is also used to verify the performance of the boosted decision tree independently and, along with Corsika simulation (see section 3.7), represents a cross check for this analysis.

### 7.4 Processing

This analysis considers all muon-like events. This means that in addition to the muon filter, the EHE filter is also considered. After the data is transferred to the north, all events are processed to level 2. Level 2 is a relatively light processing of the data that does a 10 iteration SPE fit, which is used as the seed to a single iteration MPE fit. More CPU intensive fits are not done at this time. After level 2, additional cuts are made to separate signal from background and events that get classified as neutrino candidates with respect to these cuts get processed to level 3. This level does the more CPU intensive calculations including a Paraboloid fit and a Bayesian likelihood fit, which are used in this analysis. While data and Collaboration-wide simulation are processed to this level by the Collaboration, the individual GRB's simulation must be processed to this level as well. This is done

by adapting the processing scripts to run on the local computing resources. The adapted scripts were run on data and simulation that was processed by the official scripts using the computing resources in Wisconsin, and the results were compared to make sure they were consistent. After data and simulation are processed to Level 3, a BDT is used to further separate signal from background. The signal efficiencies and event rates at each level are shown in table 7.1.

## 7.5 Boosted Decision Tree

After processing data to level 3 a boosted decision tree is trained. For this purpose the first 3 days of every month of the IC59 run were used as the background sample. The data used was spread out over the year to minimize the effect of seasonal variations. One of the systematic studies done was to use data from only December to train the BDT and compare the result (Systematic section). The signal input to the BDT was a signal simulation of all of the GRBs in the sample. The events were weighted to the individual GRB spectra for the training. This was implemented in ROOT's TMVA [57] [77] package and 6 parameters were used. They are:

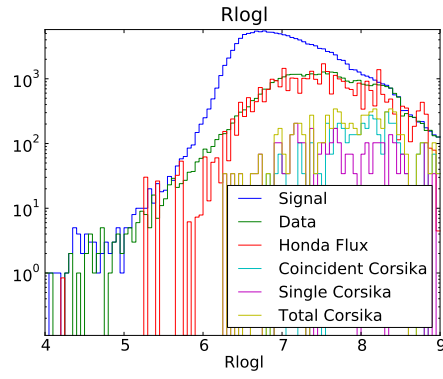
- MPEFit rlogl
- MPEFit Ldir
- MPEFit Ndir
- 8 iteration SPE Bayesian likelihood ratio
- Linefit Velocity

- The difference between MPEFit Zenith and Linefit Zenith

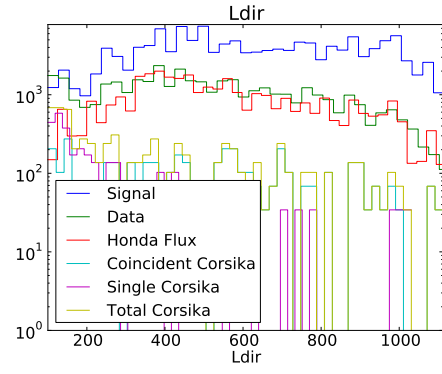
Figure 7.2 shows plots of the parameters in the level 3 dataset used in the training of the BDT. Shown is data, signal, all-sky neutrino simulation weighted to an atmospheric spectrum (Honda [79]) and muon simulation (single Corsika and coincident Corsika). Using these input variables a BDT is trained. To test the performance of the trained BDT an independent signal simulation sample is used along with data from the rest of the year; that is to say data that was taken during a good run, that was not within 2 hours of a GRB and was not used in the training of the BDT. Moreover independent all sky neutrino simulation was used to gauge performance. Plots 7.3 show the performance of the BDT. You can see that data and background simulation agree for lower BDT scores while data and atmospheric neutrino simulation agree for higher BDT values. The place where about 50% of data is signal and 50% is background is a BDT score of 0.0. This is illustrated in figure 7.4 showing the ratio of data to simulation. In table 7.1 a summary of the different cut levels is shown. The event rate is shown at each cut level along with the signal efficiency for both GRB signal and atmospheric neutrino signal.

Table 7.1: Cuts Summary Table

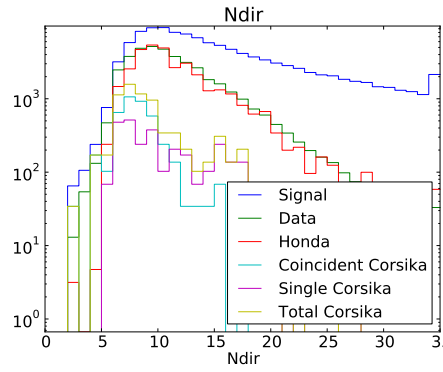
Level	Event Rate	signal efficiency	Atmospheric neutrino efficiency
Level0 (Raw Data)	2000Hz	100%	100%
Level1 (see 3.4.5)	20Hz	90%	78.9%
Level3	0.24Hz	68%	50%
Final Cut Level	$1.8^{-3}$ Hz	50%	35%



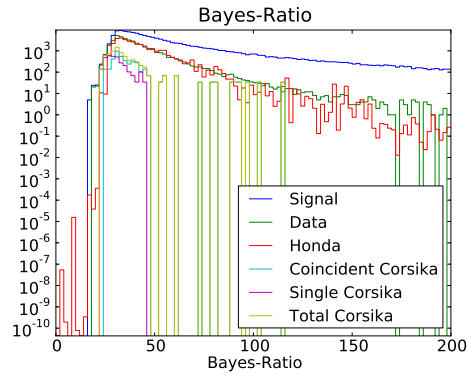
(a)



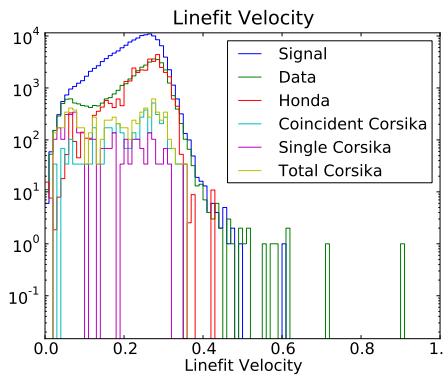
(b)



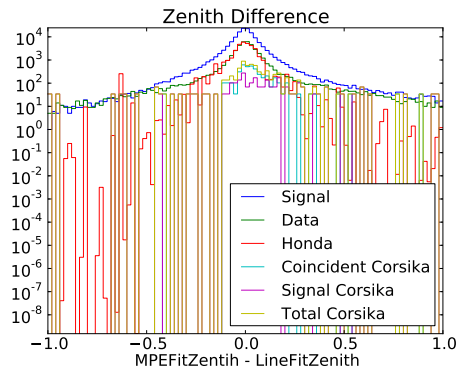
(c)



(d)



(e)



(f)

Figure 7.2: Level 3 Quality Parameters used to train the BDT. The blue line represents the GRB neutrino signal, green is data, red is neutrino simulation weighted to an atmospheric flux (Honda [79]) while the yellow line shows the total background simulation remaining at level 3.

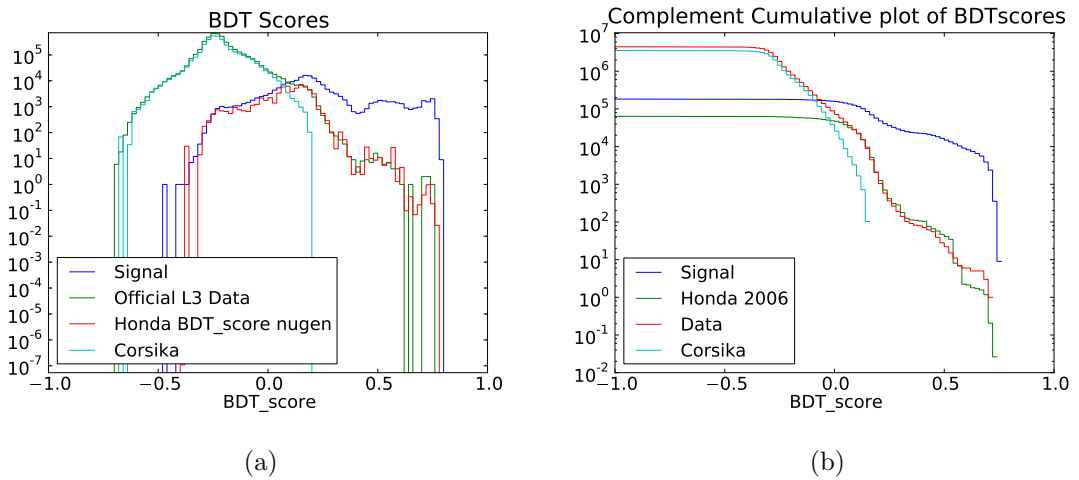


Figure 7.3: This plot shows the performance of the BDT. Signal is seen in blue, with data being green. Atmospheric neutrino simulation is plotted in red and background simulation is in teal. Data and background simulation agree in the background-like region (BDT score  $< 0$ ) while data agrees with the atmospheric neutrino simulation in the more signal-like region, with a turn over around a BDT score of 0.05.

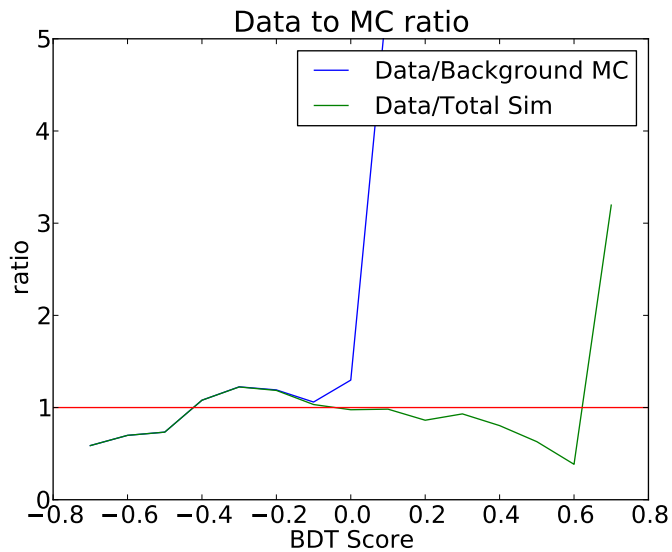


Figure 7.4: This figure shows the ratio of Background simulation to data for different BDT scores. There is a clear turn over near a BDT score of 0 where there are more signal events remaining in data than background events.

## 7.6 Unbinned Likelihood Method

The unbinned likelihood method theory was covered in 6.4 and this section is devoted to showing how it is implemented in this analysis. The signal and background PDFs for each event are described as follows:

$$S_i^{tot}(\vec{x}, t, \vec{q}) = \text{PDF}_i^{space}(\vec{x}) \times \text{PDF}_i^{time}(t) \times \text{PDF}_i^{Energy}(E) \quad (7.1)$$

$$B_i^{tot}(\vec{x}, t, \vec{q}) = \text{PDF}_i^{space}(\vec{x}) \times \text{PDF}_i^{time}(t) \times \text{PDF}_i^{Energy}(E) \quad (7.2)$$

here  $\vec{x}$  represents the reconstructed direction and error,  $t$  represents time and  $E$  is the reconstructed event energy.

### 7.6.1 The Space PDF

The signal space PDF is described by a two dimensional Gaussian:

$$\text{PDF}_i^{space}(\vec{x}) = \frac{1}{2\pi\sigma_i^2} e^{-\frac{(\vec{x}_i - \vec{x}_{GRB})^2}{2\sigma_i^2}} \quad (7.3)$$

here  $\sigma_i^2$  is defined as follows:

$$\sigma_i^2 = \sigma_{event}^2 + \sigma_{GRB}^2 \quad (7.4)$$

with  $\sigma_{event}$  being the IceCube event uncertainty as calculated by Paraboloid sigma (see 4.6.3) and  $\sigma_{GRB}$  is the uncertainty in the location of the GRB as reported by the satellites.  $\vec{x}_i$  is the reconstructed track direction and  $\vec{x}_{GRB}$  is the location of the GRB.

The background space PDF is computed from the distribution of all off time background events in the final sample. The events get histogrammed in space and a spline

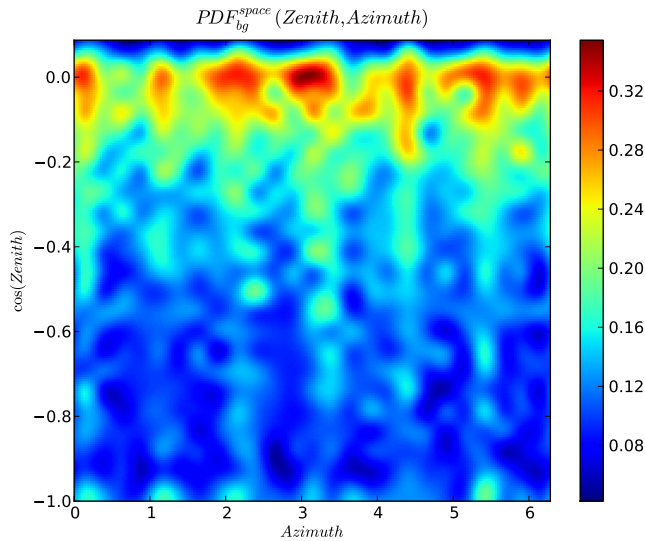


Figure 7.5: This plot shows the Background PDF for the final data sample. A spline interpolation was used after histogramming all events that survive the final cut.

interpolation is performed to smooth out the histogram. Figure 7.5 shows the background space PDF at the final cut level.

### 7.6.2 The Time PDF

The time PDF is flat over  $T_{100}$  of the burst and then falls smoothly in a Gaussian on either side. The width of the Gaussian is equal to the  $T_{100}$  of the burst with a minimum of 2 seconds and a maximum of 20 seconds. The time PDF gets cut off on either side two Gaussian widths away from the  $T_{100}$  time period. Figure 7.6 shows an example of the Time PDF for a theoretical GRB with  $T_{100} = 10s$ . The background time PDF is assumed to be flat over the entire on time window.

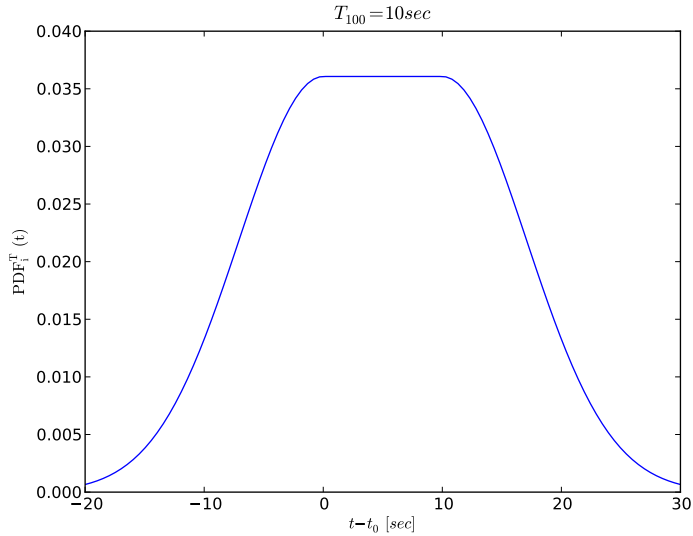


Figure 7.6: This plot shows the Time PDF for a theoretical GRB with  $T_{100} = 10s$ . It is flat over the  $T_{100}$  region with Gaussian tails on either side. The width of the Gaussian is chosen to be equal to  $T_{100}$ .

### 7.6.3 The Energy PDF

The third component of the total PDF is the energy component. In 2.2.3 it was shown that GRB neutrinos have a harder energy spectrum than atmospheric neutrinos and hence this information can be used to distinguish GRB neutrinos from atmospheric neutrinos. This process is made more difficult because the Earth starts becoming opaque to neutrinos above  $\sim 100\text{TeV}$  and hence neutrinos with energies greater than  $100\text{TeV}$  are only expected near the horizon. This means that the energy distribution in the detected neutrinos changes with zenith angle. There isn't enough simulation or data available to compute an energy PDF for each GRB separately and so the assumption is made that a sufficiently narrow zenith band will adequately take this effect into account. Hence the northern sky is split into three

regions ( $85^\circ < \theta < 115^\circ$ ,  $115^\circ \leq \theta < 145^\circ$  and  $145^\circ \leq \theta$ ). In each region the energy variable  $\frac{dE}{dX}$  (see section 4.6.5) is histogrammed for both signal and background. The resulting histograms are then divided bin by bin to get the ratio of energy PDF used in the final analysis. This can be done because as seen in the equations of Chapter 6.4 only the ratio of the signal PDF to the background PDF is important and therefore this ratio can be pre-computed rather than doing it during the minimization of the log-likelihood. In figure 7.7 the energy PDFs as used in the final analysis are shown. Moreover 7.7 shows the energy PDFs for each region along with the statistical error bars that arise from dividing two histograms.

#### 7.6.4 The Test Statistic

Now that the PDFs have been defined the test statistic can be calculated according to 6.4. To determine the  $5\sigma$  discovery line off-time data is randomized in time  $10^9$  times and the test statistic is calculated for each trial. The resulting distribution can be seen in figure 7.8, which defines the significance of the result once the on time data is unblinded.

### 7.7 Cut Optimization

At this point in the analysis a cut value has to be chosen. This analysis could be optimized for discovery or limit setting potential. It will be shown in this section that the optimized cut only depends loosely on this choice. Nevertheless the goal of this analysis was to make a discovery and so the analysis was optimized for that

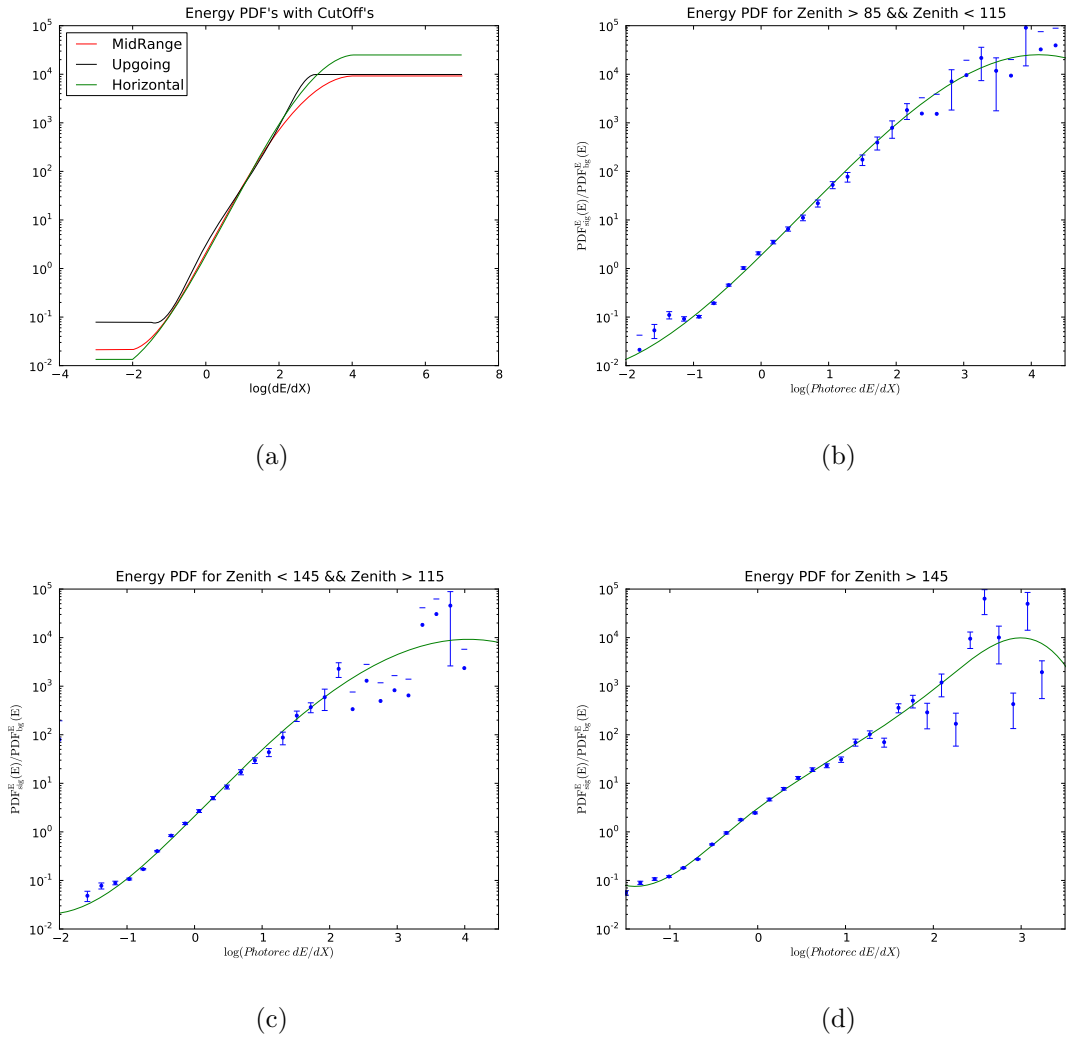


Figure 7.7: Panel (a) shows the energy PDFs as used in the final analysis. Because there is not enough data available for the very low and very high energy regions events that fall into those regions get assigned a value equal to the highest value for which there was data. Panels (b-d) show the energy PDF in the individual regions. The data points that were used to get the PDFs are shown along with their statistical error bars that arise from dividing two histograms. In figure 4.7 it is shown that  $\frac{dE}{dX}$  is a good stand in for the neutrino energy.

purpose. As a cross check the analysis was also optimized for the limit setting potential and both methods will be shown here.

### 7.7.1 Optimizing for discovery

Discovery is defined as finding a test statistic value in excess of the  $5\sigma$  fluctuation in background. In order to define where the  $5\sigma$  line is, background only data is scrambled in time  $10^9$  times from and  $\lambda$  is calculated each time. The resulting distribution gives the likelihood of background fluctuating to different  $\lambda$  values. In figure 7.8 this distribution is shown. Most trials result in a  $\lambda$  value of zero which are not shown on this plot. Once a  $5\sigma$  line ( $\lambda = 6.8$ ) is defined, signal events can be added to the scrambled background data set at a fraction of the expected model flux and the percentage of trials beyond the  $5\sigma$  line can be calculated at each fractional flux. This calculation can be done at different cut levels and the optimal cut for a  $5\sigma$  discovery for the model flux can be found in this fashion. This process takes 100-1000 CPU-hours per cut level and hence it is CPU prohibitive to do a scan of the entire cut range in small steps. This forced a rough initial scan of the cut range, followed by a finer search near the minimum. Figure 7.9 shows the result of this optimization. The weakest optimized cut from this calculation is a BDT score of 0.1. There are small fluctuations near the minimum which are to be expected as more events get cut away and the  $5\sigma$  line moves as a result. Another way to optimized the cut is to ask the question what is the model flux required to achieve a  $5\sigma$  discovery in 90% of the trials. Figure 7.10 shows the result of this calculation.

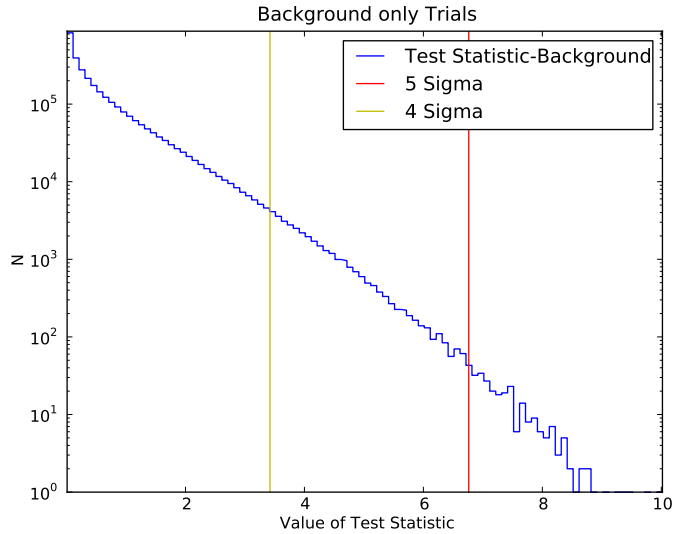


Figure 7.8: This figure shows the distribution of  $\lambda$  for background only time-scrambled data.

This optimization yields a similar result to the previous method.

### 7.7.2 Optimizing for a Limit

This analysis hopes to make a discovery and hence should be optimized for that, however, as a cross check an optimization for the limit setting potential should also be done. Considering that the limit will vary depending on the final value of the test statistic after unblinding, a value of  $\lambda$  for which the optimization is done needs to be chosen. In this case the value of  $\lambda = 0$  was chosen since it would give the best limit in case of a non-detection. Again it is too CPU intensive to scan the entire cut parameter space to determine the optimized cut, so a rough scan was done first followed by a fine scan of the region near the optimized cut. The result is shown in figure 7.11. The optimized cut in this case is more clear as the fluctuations near the

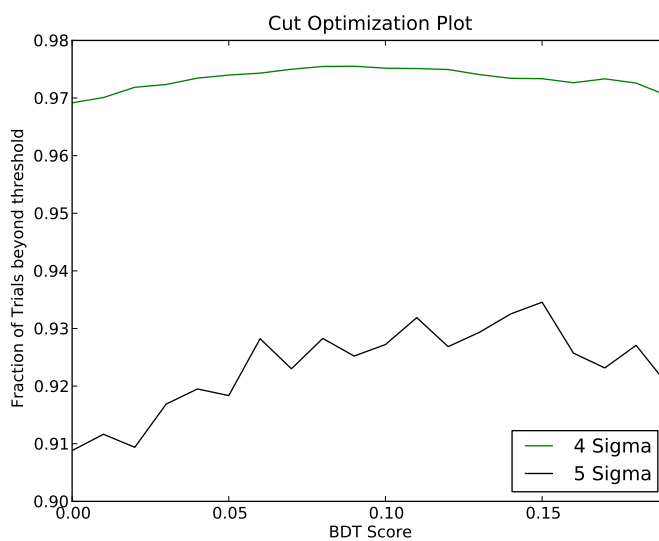


Figure 7.9: This figure shows how many signal injected trials achieve a 5, 4 $\sigma$  discovery when model flux is injected. The optimized cut is near a BDT score of 0.1.

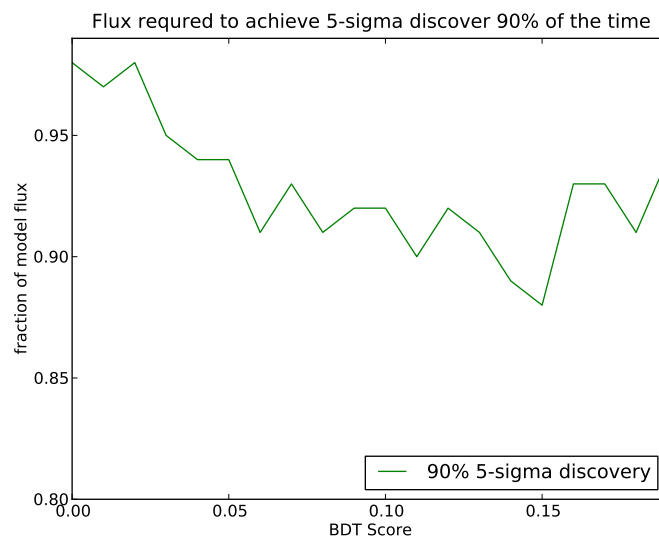


Figure 7.10: This figure shows the fraction of the model flux required to achieve a 5 $\sigma$  result in 90% of the random trials.

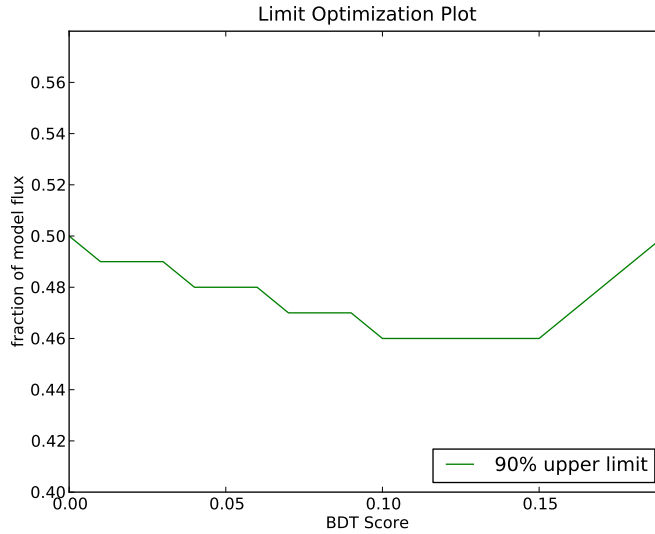


Figure 7.11: This figure shows the 90 % upper limit as a function of BDT score.

minimum are not there. The best limit setting cut for this analysis is found to be a BDT score of 0.1, which is very close to the value calculated when optimizing the analysis for a discovery. As a result the analysis retains its limit setting power even though it is optimized for a discovery.

## 7.8 Analysis Potential

After determining the optimized cut, the potential for this analysis to make a discovery can be analyzed. This can be done assuming the model flux calculation presented in Chapter 2. From figure 7.9 one can see that if the full model flux is injected there is more than a 90% chance to make a  $5\sigma$  discovery. In figure 7.12 the potential to make a  $5\sigma$  discovery is plotted with respect to the fraction of the model flux. It can be seen that even at half the model flux there is still a 50% chance to

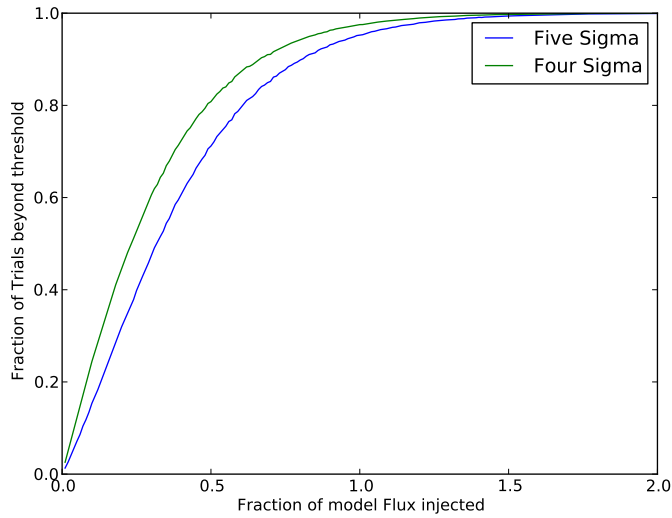


Figure 7.12: This figure shows the probability of making a  $5\sigma$  discovery with respect to a fraction of the model flux.

make a  $5\sigma$  discovery.

Before unblinding the data the limit for all possible  $\lambda$  values needs to be defined. This is done by injecting a fraction of the model flux and calculating the 90% upper limit each time (see appendix B for an explanation of how the limit is calculated). This is done starting at 0.01 times the model flux and is done up to 2 times the model flux in steps of 0.01. This maps out the statistical plane of possible values for  $\lambda$  given a range of signal fluxes. From this the 90% upper limit can be determined for any value of the test statistic  $\lambda$ . If  $\lambda$  is larger than the  $5\sigma$  threshold, a discovery is claimed and no limit will be set. Figure 7.13 shows the distribution of the test statistic for an injected model flux of 0 – 1.8 times the theoretical flux. The 90% upper limit line is shown as well, which indicates the limit that would be set after observing a given value of the test statistic in data.

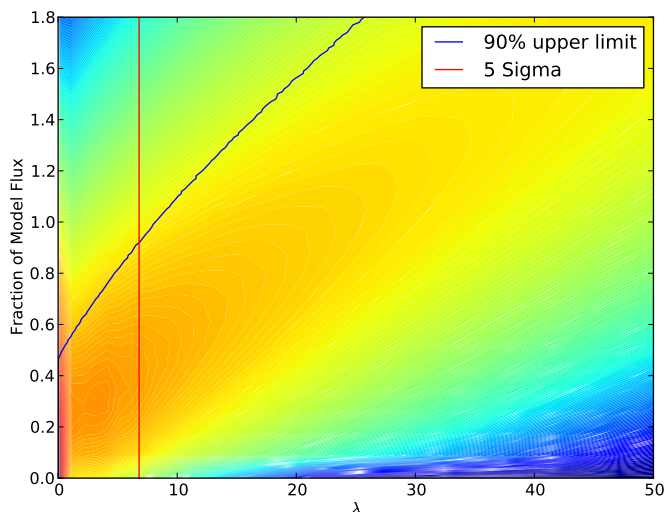


Figure 7.13: This plot shows the distribution of the test statistic for various injected model flux fractions. The 90% upper limit line is shown as well, which would indicate the limit that would be set at a given observed test statistic.

## 7.9 Systematics

IceCube is an experiment that has the potential to be dominated by systematic error, because of an incomplete understanding of the South Pole ice, moreover neutrino cross sections have never been directly measured at the energies that IceCube is sensitive to, all of which contributes to the systematic error. In this analysis the systematic error in the background estimate is small because detector data was used to estimate the background, however the final limit was determined through simulation, which is affected by systematic errors. There are various tunable parameters in the simulation chain that can be adjusted to different values. The parameters that were chosen to be varied are parameters that are known, however, have error bars on them. The values were then adjusted to the maximum and minimum al-

lowed values and the limit for this analysis was recomputed. The result from each systematic study was noted and the total systematic error was calculated by adding the individual systematic errors in quadrature.

## 7.9.1 Individual tunable parameters

### 7.9.1.1 Dom Sensitivity

The first of the parameters that are tunable within the simulation framework is the DOM sensitivity to light. This parameter is measured in a lab before the DOM is deployed, however, the lab measurement is an idealized situation and a variance of  $\pm 8\%$  is generally accepted as possible (see [80]). In essence changing the DOM sensitivity increases or decreases the total light that is detected in the detector. The effect for low energy events is that events either get detected or not detected depending on the DOM sensitivity setting. The analysis presented here is optimized for high energy events so the impact of DOM sensitivity is less important, however, at the high energy end of the spectrum the reconstructed event energy is affected by the DOM sensitivity settings which has a direct effect on this analysis. The effects of changing the DOM sensitivity can be seen in table 7.2.

Table 7.2: DOM sensitivity table

DOM Sensitivity Change	Limit Set	% change
$\pm 0\%$	0.44	-
+8%	0.44	$\pm 0\%$
-8%	0.46	+5%

### 7.9.1.2 Neutrino Cross Section

Another parameter that can be varied in simulation is the neutrino cross section. The neutrino cross sections for IceCube are calculated according to the CTEQ5 (Coordinated Theoretical-Experimental Project on QCD) model [36]. This particular model uses information from neutrino cross section experiments in the GeV range to create a neutrino cross section model. The analysis presented in this thesis is most sensitive for neutrino energies  $> 10\text{TeV}$  and hence the neutrino cross sections are extrapolated. The uncertainties for these extrapolations are believed to be  $\sim 3\%$  and hence they were varied by  $\pm 3\%$  for this systematic study. The effect of this variation is shown in table 7.3.

Table 7.3: Neutrino Cross Section Table

Cross Section Change	Limit Set	% change
$\pm 0\%$	0.44	-
+3%	0.43	-2%
-3%	0.45	+2%

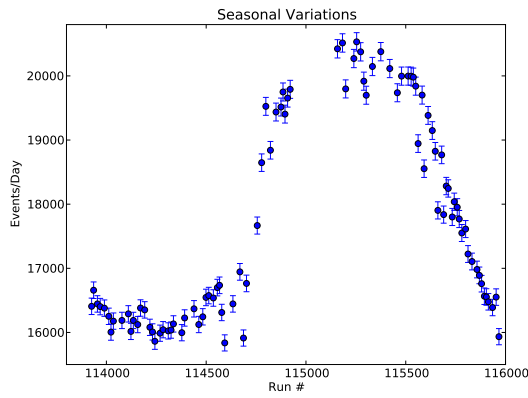
### 7.9.1.3 Seasonal Variation

In IceCube the observed event rate changes over time. This is caused by the expansion and contraction of the atmosphere above the South Pole. A thicker atmosphere allows for showers to range out more before reaching the surface and therefore more showers are able to create events in IceCube. Therefore the rate is largest when the atmosphere is the warmest, and hence the most expanded, above the South Pole. The affect of this is shown in figure 7.14. The effect is more pronounced for weaker

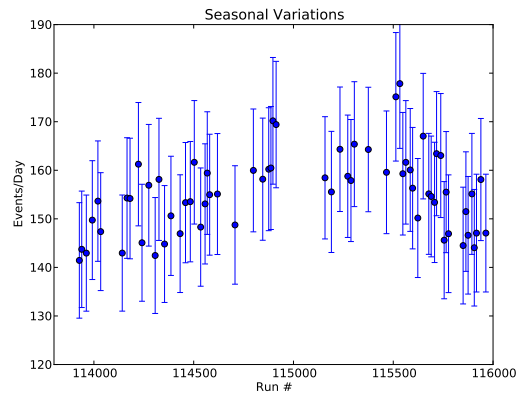
cuts but still present at the optimized cut. The analysis ignores this variation of the background rate, because of the low expected background ( $\sim 10^{-3}$  events on source and on time), however, it is accounted for in systematics.

There are two places where the variation in background rate comes into play. The first being in the training of the BDT and the second being in the estimation of the background rate. To check for systematic errors in the training of the BDT a second BDT was trained using data from the month of December only. This input background was the only thing that was changed and a new limit was computed after re-optimizing the analysis for this new training. The result was that the optimized cut passes  $\sim 41000$  events with both BDTs. The limit set in either case is 0.44 times the model flux, which indicates that the training of the BDT does not contribute significantly to the overall systematic error.

The second place the background rate comes into play is in the LogLikelihood method used in this analysis. In the calculation of the test statistic,  $\lambda$ , (see figure 7.8) the total background rate is directly involved. This can be seen in the definition of  $\lambda$  (see equation 6.24) with  $n_b$  representing the total background rate. As seen in Figure 7.14 the background rate varies as much as 10% from the median rate used in this analysis, so to account for this effect the limit was recalculated for a background rate that is varied by  $\pm 10\%$ . The result can be seen in table 7.4.



(a)



(b)

Figure 7.14: The plots here show the event rate per day for the full IC59-run. The x-axis shows the run number of each run (the run started in May 2010 and ended in May 2011). The month of December is blinded out here because it was used for training the BDT. This effect is seen around run number 115000. Panel (a) shows the result at level 3 before training the BDT. Panel (b) shows the effect of the seasonal variation at the optimized cut.

Table 7.4: Background Variation Table

Background Rate Variation	Limit Set	% change
$\pm 0\%$	0.44	-
+10%	0.44	0%
-10%	0.43	-2%

#### 7.9.1.4 The IceModel

In IceCube a major factor is the propagation of photons through the South Pole ice. The IceModel used in this analysis is SPICE (South Pole Ice, see [81]). The IceModel used in the analysis before this one is known as AHA. The limit was computed independently for each IceModel in this analysis. This yields to a difference in the final limit set by  $\pm 2\%$ , which is used as the IceModel error.

#### 7.9.2 The Total Systematic error

At this point the total systematic error for this analysis needs to be computed. The errors are added in quadrature to compute a final systematic error for this analysis. This result is seen in table 7.5.

Table 7.5: Total Systematic Error

Systematic Study	+% change	-% change
DOM Sensitivity	+5%	-0%
Neutrino Cross Section	+2%	-2%
Seasonal Variation	+0%	-2%
IceModel	+2%	-2%
Total Systematic Error	+6%	-3%

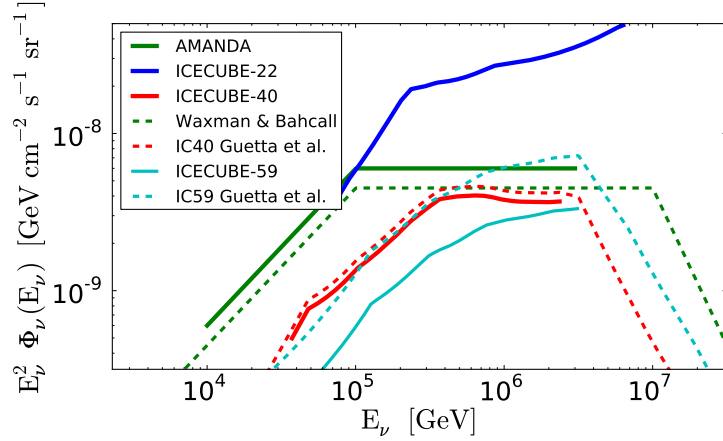


Figure 7.15: This plot shows the final result of this analysis. The 90% upper limit is 0.44 times the model flux. Previous limits are also shown on this plot by the solid lines. The dashed lines represent the model prediction with the dashed green line representing the Waxman 2003 [82] prediction. All other dashed lines represent the Guetta et al. model prediction [3]. This analysis is about a factor of 2 more sensitive than the previous best result achieved by IceCube-40. The systematic error from section 7.9 was incorporated by changing the IC59 limit by +6%.

## 7.10 Result of this Analysis

No events in the blinded time window were also on source in space with a GRB. This means that  $\lambda = 0$  and a 90% upper limit can be set at  $0.44^{+6\%}_{-3\%}$  times the model flux according to figure 7.13. This translates to a limit of 0.46, including the systematic error, which is shown in plot 7.15. This result improves the previous best limit set by IceCube-40 by a factor of  $\sim 2$ .

## 7.11 Combining this result with the previous result

The limit given in section 7.10 is the limit for the IC59 analysis only. If this limit is combined with the limit of the IC40 analysis the combined limit can

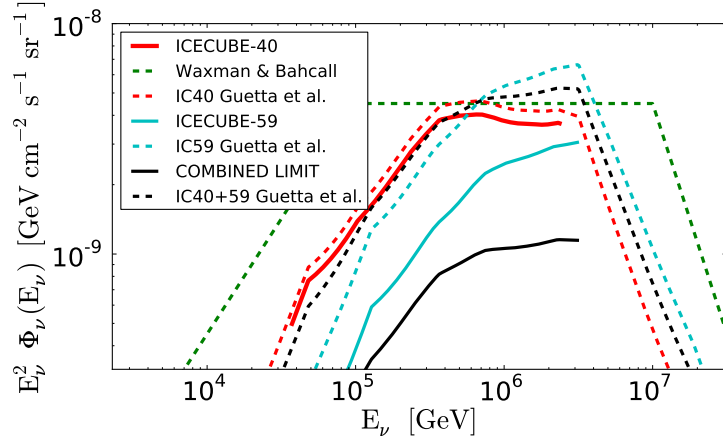


Figure 7.16: This plot shows the final result of the analysis presented in this thesis as well as the previous best result presented here [83]. Moreover, the combined result of these two analyses is shown in black. The dashed line shows the expected theoretical flux while the solid line shows the limit achieved when these two analyses are combined. The limit set is  $\sim 0.22$  times the expected theoretical flux. The dashed lines represent the model prediction with the dashed green line representing the Waxman 2003 [82] prediction. All other dashed lines represent the Guetta et al. model prediction [3].

be pushed significantly lower than the limit of either analysis by itself. The IC40 analysis and resulting limit is described here [4], with a final limit of 0.82 times the expected signal flux, therefore the limit is about a factor of two worse than the IC59 limit, nevertheless it is worthwhile combining the two limits. Two limit combining methods are outlined in appendix B and the final combined limit is determined to be 0.22 times the theoretical flux. In figure 7.16 this combined limit is shown.

In Chapter 8 the implications of this result to the model is discussed.

## Chapter 8

### Discussion of the result

This Chapter will discuss the result from the previous chapter. The implication for the neutrino production model in GRBs will be discussed and parameters in the model will be constrained.

#### 8.1 Discussion of the Result

Considering that the combined limit discussed in 7.11 is almost a factor of five less than the neutrino flux predicted in 2.2.3 it is worth asking what this means in terms of neutrino production theories of a GRB? The main question that needs to be answered is: are there tunable parameters that are not measured by the satellites that can be adjusted to account for this low limit, yet still allows for the observed gamma rays, or is there another more fundamental problem with the theory i.e. are protons not accelerated in GRBs. If it turns out that there are indeed no protons being accelerated in GRBs (or much fewer than expected), the implication would be that GRBs are not the source of ultra high energy cosmic rays (UHCRs) which would leave the origin of UHCRs a mystery. This section will attempt to give some insight into this question.

The natural place to start looking is the bulk Lorentz factor (2.2.3.1). This value is rarely measured for GRBs, and while it is well constrained on the low end, recent

developments imply that it may have been underestimated [84, 85] for some GRBs. Considering that  $\Gamma$  goes into the neutrino flux calculation directly to the 4<sup>th</sup> power as well as going into the break energy calculations as a power of 2.5 it is reasonable to assume that small changes to  $\Gamma$  would significantly affect the final limit of this analysis. The standard value for  $\Gamma = 316$ , but as implied in [86]  $\Gamma$  as high as 1000 could be possible. From recent Fermi [17] results an upper limit of  $\Gamma = 700$  is computed [87] and because the limit set at  $\Gamma > 700$  is very weak the limit this analysis is able to set is computed over a range of 200 – 700. The lower limit is taken from the considerations in 2.2.3.1 while the upper limit is taken from [87]. The result is plotted in Figure 8.1.

In the case of  $\Gamma = 700$  the best limit that can be set is  $\sim 9$  times the signal flux, which, means that in that case the model flux cannot be excluded by this analysis alone. In the case of  $\Gamma = 700$  a combined limit with the IC40 analysis cannot be set due to fact that  $\Gamma = 700$  data does not exist for the IC40 analysis. However, if one makes the assumption that the total limit scales similar to the IC59 limit than the combined limit should be scaled by a factor of  $\sim 2$ . This means that the total limit set would be  $\sim 4.5$  times the model flux, which means that the combined analysis is also unable to exclude this model. Considering that IceCube is now complete it is important to ask how well IceCube can do over its lifetime. For this lets assume that the sensitivity of the full IceCube detector is similar to the sensitivity of the combined IC40+IC59 analysis. IceCube has a planned life of 10 years and making the assumption that IceCube will not be systematics limited the limit at  $\Gamma = 700$  would be  $\sim 0.4$  times the model flux for that  $\Gamma$ . This means that IceCube should

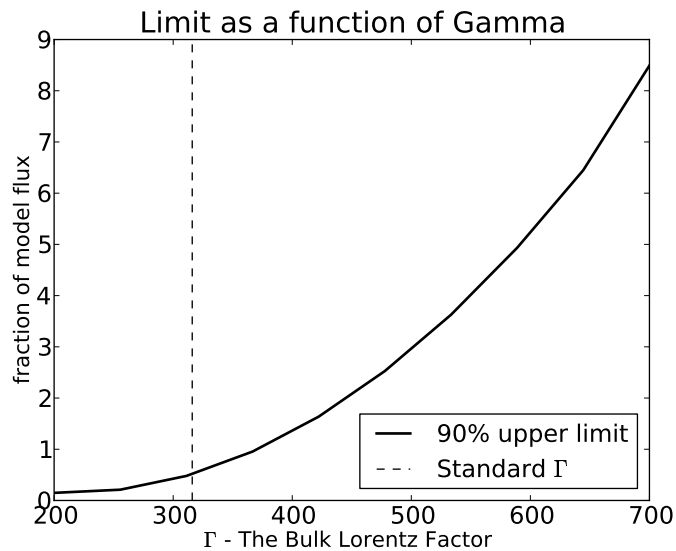


Figure 8.1: This plot shows the limit of the analysis present in this thesis as a function of  $\Gamma$ . The value used in this analysis is  $\Gamma = 316$  for which a limit of 0.44 times the theoretical flux is set. If on the other hand the extreme value of  $\Gamma = 700$  is assumed the limit that this analysis would be able to set is changed to  $\sim 9$  times the theoretical flux. At  $\Gamma \sim 350$  the limit this analysis would set is 1.0 times the expected theoretical flux.

be able to make a GRB neutrino discovery or exclude the model at a high confidence.

Another parameter that could contribute to the non-detection of a neutrino flux from GRBs is the variability of the observed  $\gamma$ -ray light curve,  $t_{var}$ . This parameter is assumed to be the characteristic time between the collision of different shock fronts in the GRB fireball. Conceptually if this time is shorter, shock fronts will collide more frequently, causing a greater number of accelerated particles and therefore more neutrinos. Looking at the equations of section 2.2.3 it can be seen that  $t_{var}$  is important in the normalization factor (see equation 2.15) as well as in the second break energy (see equation 2.13). Recent limits on  $t_{var}$  indicate that if  $t_{var}$  varied by a factor of 10 UHECR could still be explained as originating from GRBs [88]. Therefore,  $t_{var}$  was varied by a factor of 10 and the limit was recomputed in incremental steps from 0.1 – 10 times the standard  $t_{var}$  value. The result is plotted in figure 8.2. In the worst case you can see that the limit set at  $10\times$  the standard  $t_{var}$  is 3.7 times the expected flux. The model can be excluded at 90% confidence for a  $t_{var}$  of  $\sim 2.8$  times the standard  $t_{var}$ .

In the neutrino production model presented in 2.2.3 there are other factors that can change the total expected neutrino flux. Of these one value that has never been measured for any GRB is  $f_e$ , the total fraction of energy that is carried in electrons vs. protons. This value acts as an overall scale factor and according to [25] there is no good theoretical way to determine this value. Furthermore, [25] explains that GRB afterglow observations have indicated that this value should be of order 0.1. A variation of a factor of 2 in this value could be explained [25] and

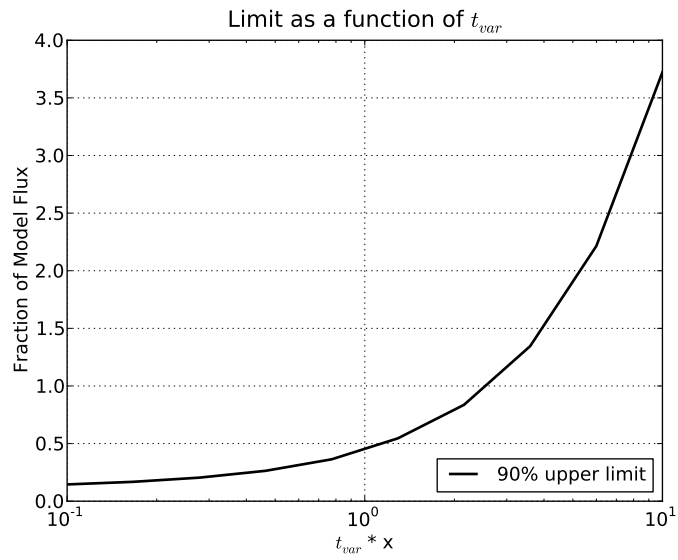


Figure 8.2: This plot show the limit set by IC59 as a function of  $t_{var} \times X$ . Here X is a multiplication factor by which  $t_{var}$  was multiplied. The limit set at  $X \sim 2.8$  is 1 times the signal flux, while in the worst case the limit set would be 3.7 times the model flux. The range chosen here was decided from considerations in [88]

hence a variation in the final expected signal flux by  $\sim 2$  can be explained as well.  $\Gamma$ ,  $t_{var}$  and  $f_e$  are the three parameters in the fireball model (see section 2.2.3) that were varied in order to modify the signal expectation from the model. The relationship between  $\Gamma$  and  $t_{var}$  is not immediately apparent, because both of these parameters come into play in the normalization factor as well as the second break energy.  $f_e$  on the other hand only affects the normalization factor and hence can be viewed as an overall scaling factor. In order to determine the exact relationship between  $\Gamma$  and  $t_{var}$  the limit for the IC59 analysis was calculated at various different points in the  $\Gamma/t_{var}$  phase space and then interpolated to achieve 2D contour plot. This is shown in figure 8.3. The thick black line indicates where  $1\times$  the model can be excluded at a 90% confidence, while the dashed lines indicate the standard values used in this analysis.

From figure 8.3 it is clear that a significant portion of the allowed phase space cannot be excluded using IC59 data alone. It is interesting to ask how well IceCube will be able to do over the life of the experiment. IceCube has a planned life time of  $\sim 10$  years and if the assumption that IceCube in the 86 string configuration is about as sensitive as the combined IC40+59 string search the sensitivity for 10 years of IC86 can be extrapolated. This extrapolation is plotted in Figure 8.4. The plot shows that most of the allowed phase space for the plotted variables is excluded with 10-years of IceCube in the 86 string configuration.

The one parameter that has not been plotted here is  $f_e$ . This parameter is a scaling factor in the overall normalization and can vary as much as a factor of 2 [25]. Assuming the worst case and plotting that the worst case exclusion region for 10

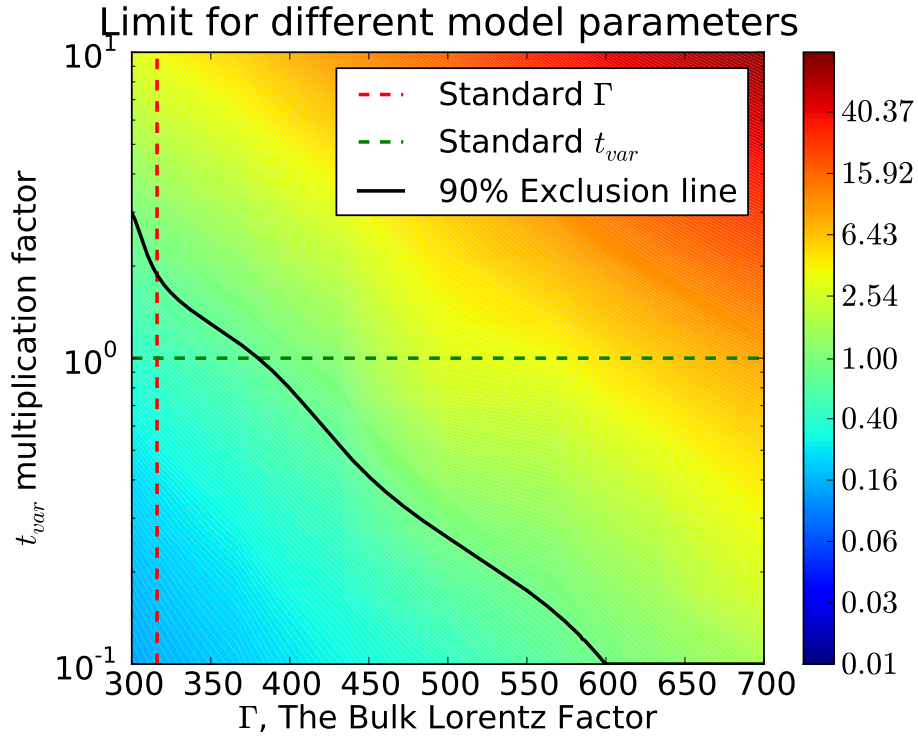


Figure 8.3: This plot shows the limit set by the IC59 analysis as a function of the  $t_{var}$  multiplication factor  $X$  and  $\Gamma$ . The color scale indicates the fraction of the model flux that can be excluded at each point of the phase space. The thick black line indicates where  $1\times$  the model can be excluded while the dashed lines indicated the standard values used in this analysis. The excluded region is the region found to the left and below the exclusion line. Note that this plot is a 'log(z)' plot.

years of IceCube-80 can be found. Figure 8.5 shows this scenario. It can be seen that although the exclusion region has shrunk compared to using the standard  $f_e$  (see figure 8.4) a significant portion of the allowed phase space is still excluded after 10 years of IceCube-80. It is argued in [88] that the phase space region that would not be excluded directly by this analysis would be disfavored by theory because for those values of  $\Gamma$  and  $t_{var}$  not enough Ultra High Energy Cosmic Rays would be produced in this model.

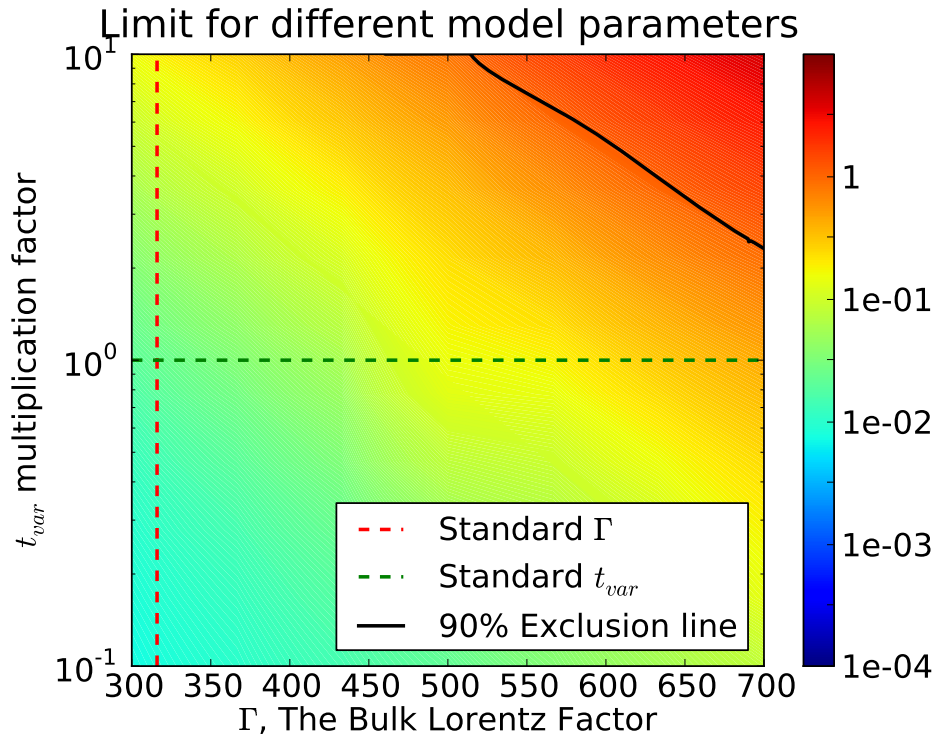


Figure 8.4: This plot shows the extrapolated limit that 10 years of Ice-Cube in the 86 string configuration will be able to achieve as a function of  $t_{var}$  and  $\Gamma$ . The color scale indicates the fraction of the model flux that can be excluded at each point of the phase space. The thick black line indicates where  $1 \times$  the model can be excluded while the dashed lines indicated the standard values used in the model. The excluded region is the region found to the left and below the exclusion line, which indicates that 10 years of IC-80 should be able to exclude most of the allowed phase space of these two parameters. Note that this plot is a 'log(z)' plot.

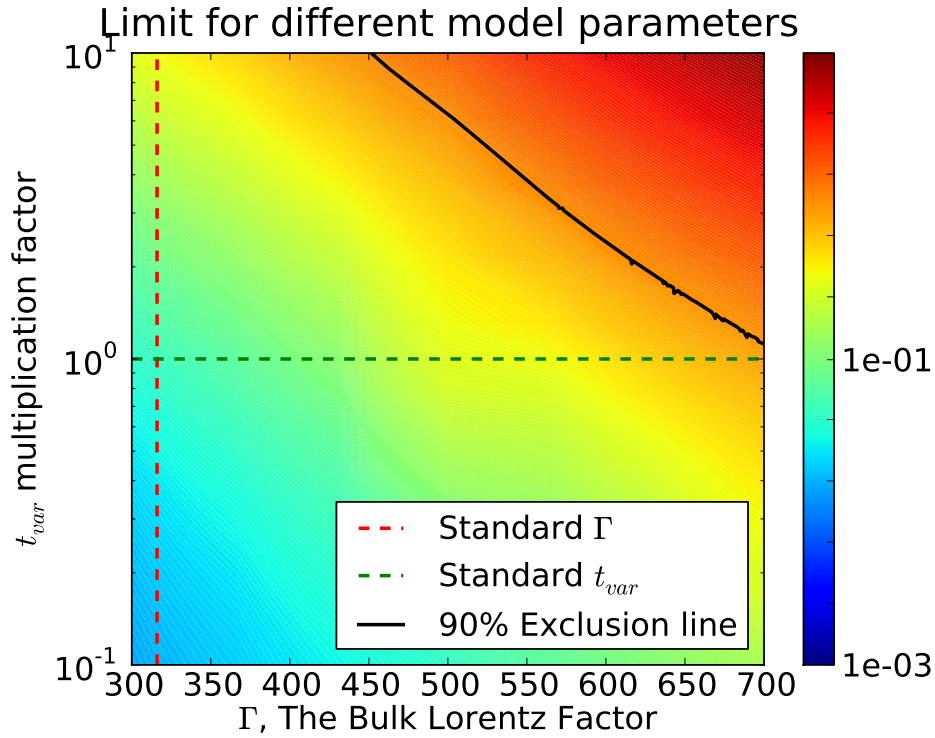


Figure 8.5: This plot shows the extrapolated limit that 10 years of Ice-Cube in the 86 string configuration will be able to achieve as a function of  $t_{var}$  and  $\Gamma$ , if  $f_e$  is varied in such a way as to achieve the worst possible scenario. The color scale indicates the fraction of the model flux that can be excluded at each point of the phase space. The thick black line indicates where  $1\times$  the model can be excluded while the dashed lines indicated the standard values used in the model. The excluded region is the region found to the left and below the exclusion line, which indicates that 10 years of IC-80 should be able to exclude most of the allowed phase space of these two parameters even when the worst case is assumed for the  $f_e$  parameter. Note that this plot is a 'log(z)' plot.

## Chapter 9

### Conclusion and Outlook

#### 9.1 Conclusion

The IceCube 59-string data was used to search for a neutrino signal in coincidence with a GRB trigger. 98 bursts were in the northern hemisphere were considered and no neutrino signal was found and a limit of 0.46 times the theoretical flux was set. The limit was then combined with the previous non-detection, the IceCube 40-string result. The combined limit is able to exclude a neutrino flux 5 times below the expected flux at a 90% confidence, which conclusively excludes the model as it was assumed in for this flux calculation. The model has various tuneable parameters that affect the final predicted flux. The model parameters then were adjusted within a range that would still allow GRBs to be the source of UHECRs, and explain the non-detection of this analysis.

Construction of IceCube finished in December, 2010, which means that there are now 86 strings buried in the South Pole ice. With the full detector the sensitivity to a neutrino signal increases so the question of how long it would take to exclude the allowed parameter space is asked. IceCube is slanted to operate at least 10 years in the 86-string configuration, which is long enough to cover most of the allowed parameter space, however (see figure 8.4. To cover the entire allowed parameter space it would take  $\sim 25$  years of IceCube in the 86-string configuration. The statements

made about the IC-86 performance depend on the availability of satellite data from GRBs and therefore once the current GRB missions reach the end of their lives IceCube may not be able to do further GRB searches, if there are no new GRB missions launched. However, this should not be discouraging, considering that it will take  $\sim 3$  years of IC86 operation to cover about half of the allowed parameter space, and as IceCube continues to operate more stringent limits on the neutrino emission models from GRBs will be set and hence more stringent limits on the GRB-UHECR models in use today. Alternatively IceCube could be the first neutrino detector to discover a neutrino flux with extra-galactic origin.

## Appendix A

### Shock Acceleration

This appendix is devoted to shock acceleration.

#### A.1 Accelerating Particles

In the previous section the production of high energy neutrino's was discussed. This section will talk about the processes that are responsible to produce the high energy particles involved in the production of high energy neutrino's.

##### A.1.1 Fermi acceleration

The first acceleration process that one has to talk about when talking about cosmic ray particles is the so called Fermi acceleration process. There are two types of Fermi acceleration method's that are similar but still different enough that it is warranted to talk about them separately.

###### A.1.1.1 First order Fermi acceleration

First order Fermi acceleration is a process that happens within a shock-wave and is responsible for transferring kinetic energy from the shock-wave to a single charged particles. In order to talk about this mechanism let us consider one test particle that enters a shock-wave and is then accelerated. The first assumption that

we have to make is that the particle entering the shock-wave is relativistic before it enters the acceleration region. The basic idea is that after the particle enters the acceleration region it undergoes stochastic collisions and in each collision it gains an amount of energy that is proportional to its own current energy,  $\delta E = \zeta E$ . This of course means that after  $n$  encounters the particle has energy:

$$E_n = E_0(1 + \zeta)^n \quad (\text{A.1})$$

It is known that a particle that enters an acceleration region will eventually leave that acceleration region and hence there is a probability  $P_{esc}$  that the particle will leave the acceleration region after each encounter. This means that after one encounter the probability of the particle to remain in the acceleration region is  $1 - P_{esc}$  and hence the probability of it to still be in the acceleration region after  $n$  encounters is:

$$(1 - P_{esc})^n \quad (\text{A.2})$$

The next question that should be asked is: how many encounters will it take to reach energy  $E_n$ . To get this number we need to take the log of  $E_n = E_0(1 + \zeta)^n$  and manipulate the result to reach:

$$n = \frac{\ln \frac{E_n}{E_0}}{\ln(1 + \zeta)} \quad (\text{A.3})$$

Now lets combine this with the probability that a particle will escape after each encounter in order to get the fraction of particles that will make it to an energy  $E_n$  or more. So the number of particles that will make it is proportional to:

$$N(\geq E) \propto \sum_{n=m}^{\infty} (1 - P_{esc})^m = \frac{(1 - P_{esc})^n}{P_{esc}} \quad (\text{A.4})$$

Here  $n$  is the value from above. Substituting  $n$  into the equation for  $N(\geq E)$  we get:

$$N(\geq E) \propto \frac{(1 - P_{esc})^{\frac{\ln \frac{E_n}{E_0}}{\ln(1+\zeta)}}}{P_{esc}} \quad (\text{A.5})$$

Now if we take the  $\ln$  of both sides:

$$\ln(N(\geq E)) \propto \ln \frac{1}{P_{esc}} + \ln(1 - P_{esc}) \ln \frac{E_n}{E_0} \ln(1 + \zeta) \quad (\text{A.6})$$

Now if we exponentiate both sides and rearrange second term in the above equation we get:

$$N(\geq E) \propto \frac{1}{P_{esc}} \left( \frac{E_n}{E_0} \right)^{-\frac{\ln \frac{1}{1-P_{esc}}}{\ln(1+\zeta)}} \quad (\text{A.7})$$

Now if we make the assumption that both  $P_{esc}$  and  $\zeta$  are small we can expand the exponent of the above equation in a series. Doing so we get:

$$\ln \frac{1}{1 - P_{esc}} \approx 0 + P_{esc} + \text{Higher order Terms} \quad (\text{A.8})$$

and

$$\ln(1 + \zeta) \approx \zeta - \frac{1}{2}\zeta^2 + \text{Higher order Terms} \quad (\text{A.9})$$

Combining the above results and ignoring all Higher order terms we get:

$$\frac{\ln \frac{1}{1-P_{esc}}}{\ln(1 + \zeta)} \approx P_{esc}/\zeta \quad (\text{A.10})$$

therefore we get:

$$N(\geq E) \propto \frac{1}{P_{esc}} \left( \frac{E_n}{E_0} \right)^{-P_{esc}/\zeta} \quad (\text{A.11})$$

Looking at the above equation it is clear that the resulting spectrum will be a power law spectrum. Also looking at the equation it is obvious that if the escape probability increases and the amount of energy transferred decreases that steepens

up the spectrum while a lower escape probability and higher energy transfer per collision will make the spectrum shallower. Qualitatively this is exactly what we would expect to happen.  $P_{esc}$  and  $\zeta$  are both determined by the physics in the shock front and is the subject of the next section.

### A.1.1.2 Physics inside the shock wave

First lets consider what happens when a shock waves moves through a region of magnetized plasma. Lets assume that there is a test particle inside the magnetized plasma ahead of the approaching shock front (upstream). The test particle will enter the shock front when the shock front arrives and start moving to the region of shocked plasma that was left by the shock front (downstream). In that region it will get scattered by so called magnetic mirrors (more on that later) and will gain velocity through that process. After it was scattered often enough and has gained enough velocity it will move back through the shock front to the upstream region. This is known as one cycle. The energy gained during one cycle is the important question at hand.

Lets start by defining what happens in the downstream region of the shock wave. We assume that all scattering in that region is elastic and so the velocity of the particle will change after each scattering and eventually the average motion of the particle will coincide with the plasma. After the particle moves back through the shock front and re-enters the upstream region it will have gained energy proportional to the Lorentz factor between the upstream and downstream region. To make things

simple lets assume that the particle enters and exits the downstream region with an angle equal to  $\pi/2$ . So to start lets assume that the particle has energy  $E_1$  in the upstream region. Transferring that energy to the frame of the downstream plasma we get  $E'_1 = \gamma E_1$ . All the scatterings inside the cloud are elastic and hence no energy is gained by the particle so that  $E'_2 = E'_1$  just before the particle exits the downstream region. Now lets transform back to the laboratory frame and we get that  $E_2 = \gamma E'_2$ . Now since  $E'_2 = E'_1$  we can write:

$$E_2 = \gamma^2 E_1 \tag{A.12}$$

Of course this is an unrealistic scenario since particles will not enter and exit the region at an angle of  $\pi/2$ . Hence we will need to modify the above equation to take into account the angle of incidence ( $\theta_i$ ) and the angle of exit ( $\theta_e$ ). Using those angles we can write  $E'_1 = \gamma E_1(1 - \beta \cos \theta_i)$ . Where beta is the standard  $v/c$ . Moreover we can write  $E_2 = \gamma E'_2(1 + \beta \cos \theta_e)$ . Now doing the same substitution as before we get:

$$E_2 = \gamma^2 E_1(1 - \beta \cos \theta_i)(1 + \beta \cos \theta_e) \tag{A.13}$$

The particle entering this acceleration region was assumed to be relativistic (as mentioned above) and hence it was assumed that  $pc \approx E$  for this calculation.

It is useful to try to figure out what the average energy gain per cycle is. The factors we need to consider for that calculation are the average of each of the cosine functions. We know that the  $-1 \leq \cos \theta_i \leq 0$  and  $0 \leq \cos \theta_e \leq 1$ . Finding the averages of  $\cos \theta_i$  and  $\cos \theta_e$  we get  $-2/3$  and  $2/3$  respectively. Plugging that in we

get:

$$E_2 = \gamma^2 E_1 \left(1 - \frac{-2}{3}\beta\right) \left(1 + \frac{2}{3}\beta\right) \quad (\text{A.14})$$

or

$$E_2 = \gamma^2 E_1 \left(1 + \frac{4}{3}\beta + \frac{4}{9}\beta^2\right) \quad (\text{A.15})$$

The above equation gives the resulting energy of a particle after one cycle. To get the fractional energy gain per cycle one has to subtract the original energy from the resulting energy.

### A.1.1.3 Second Order Fermi acceleration

In the previous section the process of particle energy gain was discussed, however, an important part was left out: The way a charged particle gains energy when it is scattered off a moving magnetic field. Second order Fermi acceleration gives insight in the amount of energy gained by a particle moving in the presence of randomly moving magnetic mirrors. The basic idea is, that if a particle moves into a magnetic field that is moving towards it will gain energy and if it moves into a magnetic field that is moving away from it it will lose energy. Of course if the magnetic field is stationary the particle neither loses or gains energy. Fermi argued that a particle is more likely to move into a magnetic field that is moving towards it than one that is moving away from it and hence there will be a net energy gain. The reason this process is called second order Fermi acceleration is the fact that the energy gained per bounce depends on the mirrors velocity squared and hence this process is known as second order Fermi Acceleration.

## Appendix B

### Neyman Limit and Combining Limits

This Appendix is devoted to outline how to calculate a Neyman limit used in this analysis, as well as outline an analytic method to combining two null results for a GRB Analysis.

#### B.1 Neyman Limits

For a full account on Neyman limits please refer to [83] and the references contain in that paper. This section will outline how a Neyman limit was calculated for the analysis presented in this Thesis.

In the case of a GRB analysis the upper limit is calculated by first calculating the final test statistic after unblinding the analysis (before unblinding a sensitivity for a given final test statistic can be calculated). After the final value of the test statistic is known, signal events from simulation are injected at a fraction of the model flux. This fraction gets varied until 90% of the signal trials yield a value that is greater than the test statistic from the final result. In the case of the analysis presented in this Thesis the test statistic evaluated after unblinding was zero and the final limit was 0.44 Times the model flux (see 7.10).

## B.2 Combining Limits

The analysis preceding this analysis also had a non-detection [4] and therefore the limits can be combined. This section will outline two methods of doing so. The first will be a brute force method while the second will be a more elegant analytic method. It will be shown that either method leads to a similar result.

### B.2.1 Brute Force

The simplest method for combining two limits would be to start with the simulation data sets for the two analyses that need to be combined and combine the signal events into one file that contains all events. This combined file would be the total expected signal flux for both analysis. Considering that both analyses saw a null result the actual distribution of the test statistic can be ignored, because any injected signal trial that has a value  $> 0$  will contribute to the upper limit. This means that the fraction of the signal flux injected from simulation needs to be adjusted until 90% of signal injected trials yield a test statistic value  $> 0$ . In the case for combining the IC40 and the IC59 result this comes to 0.22 times the expected flux.

### B.2.2 The Analytic Method

This method only works if the two analyses that are being combined both had a final test statistic of zero and hence works in this case.

It turns out that most of the background only trials  $= 0$  and therefore we want 90%

of our experiments with a signal flux injected to have a test statistic larger than 0. So let us assume that we have  $N$  signal events, where  $N$  is large, and each event has a probability of contributing to the experiment of  $P_n$  (under the assumption that  $P_n \ll 1$ ). In that case the probability of seeing nothing is:

$$P_{nothing} = \prod_n (1 - P_n) \quad (\text{B.1})$$

Then for 90% Neyman limit we want to see nothing 10% of the time. Hence  $P_{nothing} = 0.1$ . At this point let us also make the assumption that  $P_n \simeq P_m$  for all  $n$  and  $m$  ( $P_n \ll 1$  still). Then:

$$P_{nothing} = \prod_n (1 - P_n) = (1 - P_n)^{N/P_n} = 0.1 \quad (\text{B.2})$$

Where  $N$  is the total number of simulated events needed with a probability of  $P_n$  to set a limit equal to the expected flux. So:

$$N = \log(0.1) \frac{P_n}{\log(1 - P_n)} \quad (\text{B.3})$$

In the limit  $P_n \ll 1$ :

$$\frac{P_n}{\log(1 - P_n)} = -1 \quad (\text{B.4})$$

and so:

$$N = -\log(0.1) = 2.3 \quad (\text{B.5})$$

This means that if the sum of all the simulation events were equal to 2.3 the limit we could set would be 1 time the Guetta et al. flux. In the IC40 analysis the sum of the weights was 2.8. So if the weights were smaller by a fraction of 0.82 the the limit would be the Guetta et. all flux or to say it in other words:

The IC40 limit is:  $0.82 * \text{the Guetta et. all flux}$ . The Brute force method yielded 0.81 [4]

The IC59 limit is:  $0.44 * \text{the Guetta et. all flux}$ . The Brute force method yielded 0.46.

### B.2.2.1 Combining limits

Now to combine the limits we can just add the expected number of simulation events together and get: Total number of events = 9.9 and hence the limit for IC40+59 is:

$0.23 * \text{the Guetta et. all flux}$ .

### B.2.3 Conclusion

Both the Analytic method and the Brute force method yield a similar final limit and hence a combined limit can be set at  $\sim 0.22$  times the total theoretical flux.

## Bibliography

- [1] Waxman Eli. Gamma-ray bursts: Potential sources of ultra high energy cosmic-rays. *Nucl. Phys. Proc. Suppl.*, 151:46–53, 2006.
- [2] Peter Meszaros. Gamma-Ray Bursts. *Rept. Prog. Phys.*, 69:2259–2322, 2006.
- [3] Dafne Guetta, D. Hooper, J. Alvarez-Muniz, F. Halzen, and E. Reuveni. Neutrinos from individual gamma-ray bursts in the BATSE catalog. *Astropart. Phys.*, 20:429–455, 2004.
- [4] Abbasi R. et al. Limits on Neutrino Emission from Gamma-Ray Bursts with the 40 String IceCube Detector. 2011.
- [5] Naomi Greenberg-Slovin (Translator) Govert Schilling (Author). *Flash!: The Hunt for the Biggest Explosions in the Universe*. Cambridge University Press, 2002.
- [6] Klebesadel; Ray W. Strong; Ian B. Olson; Roy A. Observations of Gamma-Ray Bursts of Cosmic Origin. *Astrophysical Journal*, 182:L85, 1973.
- [7] NASA. Burst and Transient Source Explorer - BATSE. 1991. URL: <http://www.batse.msfc.nasa.gov/batse/>.
- [8] K. Hurley. Receding from our grasp. *Nature*, 357:112–113, 1992.
- [9] L. Piro. The Beppo-SAX experiment (overview). In J. D. Hadjimetrioy & J. H. Seiradakis, editor, *Joint European and National Astronomical Meeting*, 1997.
- [10] E. Costa et al. Discovery of the X-Ray Afterglow of the Gamma-Ray Burst of February 28 1997. 1997.
- [11] Daniel E. Reichart. Light Curves and Spectra of Dust Echoes From Gamma-Ray Bursts and their Afterglows: Continued Evidence that GRB 970228 is Associated with a Supernova. 2000.
- [12] Daniel E. Reichart. The redshift of GRB970508. 1997.
- [13] NASA. HETE-2: The high energy transient explorer mission. URL: <http://heasarc.nasa.gov/docs/hete2/>, 2000.
- [14] Krzysztof Z. Stanek et al. Spectroscopic Discovery of the Supernova 2003dh Associated with GRB 030329. *Astrophys. J.*, 591:L17–L20, 2003.
- [15] Derek B. Fox et al. The afterglow of GRB050709 and the nature of the short-hard gamma-ray bursts. *Nature*, 437:845–850, 2005.

- [16] NASA. The swift gamma ray burst mission. *URL: <http://heasarc.nasa.gov/docs/swift/swiftsc.html>*, 2004.
- [17] NASA. Fermi: Gamma ray space telescope. *URL: <http://fermi.gsfc.nasa.gov/>*, 2008.
- [18] Ehud Nakar. Short-hard gamma-ray bursts. *Phys. Rept.*, 442:166–236, 2007.
- [19] Derek B. Fox and P. Meszaros. GRB Fireball Physics: Prompt and Early Emission. *New J. Phys.*, 8:199, 2006.
- [20] Shiho Kobayashi, Tsvi Piran, and Re'em Sari. Can internal shocks produce the variability in GRBs? *Astrophys. J.*, 490:92–98, 1997.
- [21] P Meszaros and M. J. Rees. Relativistic fireballs and their impact on external matter - Models for cosmological gamma-ray bursts. *Astrophys. J.*, 405:278, 1993.
- [22] Enrico Fermi. On the Origin of the Cosmic Radiation. *Phys. Rev.*, 75:1169–1174, 1949.
- [23] D. Band et al. BATSE observations of gamma-ray burst spectra. 1. Spectral diversity. *Astrophys. J.*, 413:281–292, 1993.
- [24] P. Mészáros. Gamma-ray bursts. *Reports on Progress in Physics*, 69:2259–2321, August 2006.
- [25] Julia K. Becker. High-energy neutrinos in the context of multimessenger physics. *Phys. Rept.*, 458:173–246, 2008.
- [26] D. Branford et al. Nuclear pion photoproduction in the Delta resonance region. *Phys. Rev.*, C61:014603, 2000.
- [27] D. Guetta, M. Spada, and E. Waxman. On the neutrino flux from gamma-ray bursts. *Astrophys. J.*, 559:101, 2001.
- [28] Francis Halzen and Dan Hooper. High-energy neutrino astronomy: The cosmic ray connection. *Rept. Prog. Phys.*, 65:1025–1078, 2002.
- [29] B. Paczynski. Gamma-ray bursters at cosmological distances. *Astrophys. J.*, 308:L43–L46, September 1986.
- [30] Soebur Razzaque, Peter Meszaros, and Bing Zhang. GeV and higher energy photon interactions in gamma-ray burst fireballs and surroundings. *Astrophys. J.*, 613:1072–1078, 2004.
- [31] R. Abbasi et al. Search for muon neutrinos from Gamma-Ray Bursts with the IceCube neutrino telescope. *Astrophys. J.*, 710:346–359, 2010.

- [32] John N. Bahcall and Eli Waxman. High energy astrophysical neutrinos: The upper bound is robust. *Phys. Rev.*, D64:023002, 2001.
- [33] Francis Halzen. Cosmic neutrinos from the sources of galactic and extragalactic cosmic rays. *Astrophys. Space Sci.*, 309:407–414, 2007.
- [34] Thomas K. Gaisser, Francis Halzen, and Todor Stanev. Particle astrophysics with high-energy neutrinos. *Phys. Rept.*, 258:173–236, 1995.
- [35] John David Jackson. *Classical Electrodynamics*. Wiley, New York, 1999.
- [36] H. L. Lai, J. Huston, S. Kuhlmann, J. Morfin, F. Olness, J. F. Owens, J. Pumplin, and W. K. Tung. Global QCD analysis of parton structure of the nucleon: CTEQ5 parton distributions. *European Physical Journal C*, 12:375–392, February 2000.
- [37] R. Gandhi, C. Quigg, M. H. Reno, and I. Sarcevic. Ultrahigh-energy neutrino interactions. *Astroparticle Physics*, 5:81–110, August 1996.
- [38] W. M. Yao et al. Review of particle physics. *J. Phys.*, G33:1–1232, 2006.
- [39] D. Chirkin and W. Rhode. All lepton propagation Monte Carlo. Prepared for 29th International Cosmic Ray Conference (ICRC 2005), Pune, India, 3-11 Aug 2005.
- [40] M. Ackermann et al. Optical properties of deep glacial ice at the South Pole. *Journal of Geophysical Research (Atmospheres)*, 111(D10):13203–+, July 2006.
- [41] A. Achterberg et al. First year performance of the IceCube neutrino telescope. *Astropart. Phys.*, 26:155–173, 2006.
- [42] C. A. Mead. Quantum theory of the refractive index. *Phys. Rev.*, 110(2):359–369, Apr 1958.
- [43] Chiba University. Icecube pmt calibration. URL: <http://www-ppl.s.chiba-u.jp/research/IceCube/pmt/>, 2006.
- [44] R. Abbasi et al. The IceCube data acquisition system: Signal capture, digitization, and timestamping. *Nuclear Instruments and Methods in Physics Research A*, 601:294–316, April 2009.
- [45] C. E. Navia, C. R. A. Augusto, H. M. Portella, and H. Shigueoka. How opaque is the earth to ultrahigh energy neutrinos? *Phys. Rev. D*, 67(10):103008, May 2003.
- [46] *Hadronic Interaction Models and the Air Shower Simulation Program CORSIKA*, Hamburg, Germany, August 2001.

- [47] J. Lundberg et al. Light tracking for glaciers and oceans: Scattering and absorption in heterogeneous media with Photonics. *Nucl. Instrum. Meth.*, A581:619, 2007.
- [48] NVIDIA Corporation. *NVIDIA CUDA Compute Unified Device Architecture Programming Guide*. NVIDIA Corporation, 2007.
- [49] C. Roucelle. Documentation for the domcalibrator module. Technical report.
- [50] D. Chirkin. Feature extraction of icecube waveforms. Technical report.
- [51] J. Ahrens et al. Muon Track Reconstruction and Data Selection Techniques in AMANDA. *Nucl. Instrum. Meth.*, A524:169–194, 2004.
- [52] P. B. Price and K. Woschnagg. Role of group and phase velocity in high-energy neutrino observatories. *Astropart. Phys.*, 15:97–100, 2001.
- [53] Dirk Pandel. Bestimmung von Wasser- und Detektorparametern und Rekonstruktion von Myonen bis 100 TeV mit dem Baikal-Neutrinooteleskop NT-72. Diploma thesis, Humboldt-Universitt zu Berlin, Berlin, Germany, February 1996.
- [54] George Japaridze and Mathieu Ribordy. Realistic arrival time distribution from an isotropic light source. 2005.
- [55] N. van Eijndhoven, O. Fadiran, and G. Japaridze. Implementation of a Gauss convoluted pandel PDF for track reconstruction in neutrino telescopes. *Astropart. Phys.*, 28:456–462, 2007.
- [56] D. Boersma. Gulliver loglikelihood reconstruction framework. Technical report, 2009.
- [57] CERN. ROOT. 1994. URL: <http://root.cern.ch/>.
- [58] T. Neunhöffer. Estimating the Angular Resolution of Tracks in Neutrino Telescopes Based on a Likelihood Analysis. *Astropart. Phys.*, 25:220–225, 2006.
- [59] Sean Grullon, David J. Boersma, and Gary Hill. Photonics-based log-likelihood reconstruction in icecube. Internal report, IceCube, Madison, Wisconsin, July 2008. URL: <http://internal.icecube.wisc.edu/reports/details.php?type=report&id=icecube\%2F200807001>.
- [60] W. Huelsnitz. *Search for quantum gravity with IceCube and high energy atmospheric neutrinos*. PhD thesis, University of Maryland, College Park, 2010.
- [61] NASA. GCN: The gamma ray bursts coordinates network. URL: <http://gcn.gsfc.nasa.gov>, 2009.
- [62] William R. Leo. *Techniques for nuclear and particle physics experiments: a how-to approach*. Springer, 1994.

- [63] N. Gehrels et al. The Swift Gamma-Ray Burst Mission. *AIP Conf. Proc.*, 727:637–641, 2004.
- [64] S. D. Barthelmy et al. The Burst Alert Telescope (BAT) on the Swift MIDEX Mission. 2005.
- [65] David N. Burrows et al. The Swift X-ray Telescope. *Space Sci. Rev.*, 120:165, 2005.
- [66] IPN. IPN3 homepage. 1990. URL: <http://www.ssl.berkeley.edu/ipn3/>.
- [67] NASA. Konus-Wind homepage. 1994. URL: <http://heasarc.gsfc.nasa.gov/docs/heasarc/missions/wind.html>.
- [68] ASI. Agile satellite. 2007. URL: [http://www.cgspace.it/index.php?option=com\\_content&task=view&id=143&Itemid=66](http://www.cgspace.it/index.php?option=com_content&task=view&id=143&Itemid=66).
- [69] M. Tavani et al. The AGILE space mission. *Nucl. Instrum. Meth.*, A588:52–62, 2008.
- [70] JAXA. Suzaku satellite. 2005. URL: <http://www.astro.isas.ac.jp/suzaku/>.
- [71] Masanori Ohno et al. Spectral Properties of Prompt Emission of Four Short Gamma-Ray Bursts Observed by the Suzaku-WAM and the Konus- Wind. 2008.
- [72] ESA. INTEGRAL homepage. 2002. URL: <http://sci.esa.int/science-e/www/area/index.cfm?fareaid=21>.
- [73] Sandro Mereghetti. Gamma-Ray Bursts observed by INTEGRAL. *AIP Conf. Proc.*, 727:607–612, 2004.
- [74] B. P. Roe, H.-J. Yang, J. Zhu, Y. Liu, I. Stancu, and G. McGregor. Boosted decision trees as an alternative to artificial neural networks for particle identification. *Nuclear Instruments and Methods in Physics Research A*, 543:577–584, May 2005.
- [75] H.-J. Yang, B. P. Roe, and J. Zhu. Studies of boosted decision trees for Mini-BooNE particle identification. *Nuclear Instruments and Methods in Physics Research A*, 555:370–385, December 2005.
- [76] Yoav Freund and Robert E. Schapire. A short introduction to boosting. 1999. *Journal of Japanese Society for Artificial Intelligence*, 14(5):771-780, September, 1999. (Appearing in Japanese, translation by Naoki Abe.).
- [77] Andreas Hoecker, Peter Speckmayer, Joerg Stelzer, Jan Therhaag, Eckhard von Toerne, and Helge Voss. TMVA: Toolkit for Multivariate Data Analysis. *PoS, ACAT:040*, 2007.
- [78] R.J. Barlow. *Statistics*. Wiley, 1989.

- [79] M. Honda, T. Kajita, K. Kasahara, S. Midorikawa, and T. Sanuki. Calculation of atmospheric neutrino flux using the interaction model calibrated with atmospheric muon data. 75(4):043006–+, February 2007.
- [80] R. Abbasi et al. Calibration and characterization of the IceCube photomultiplier tube. *Nuclear Instruments and Methods in Physics Research A*, 618:139–152, June 2010.
- [81] Dimitry Chirkin. Study of South Pole ice transparency with IceCube flashers. URL: <http://icecube.wisc.edu/~dima/work/WISC/ppc/spice/paper/a.pdf>.
- [82] E. Waxman. Astrophysical sources of high energy neutrinos. *Nucl. Phys. B Proc. Suppl.*, 118:353–362, April 2003.
- [83] Gary J. Feldman and Robert D. Cousins. Unified approach to the classical statistical analysis of small signals. *Phys. Rev. D*, 57(7):3873–3889, Apr 1998.
- [84] Xiaohong Zhao, Zhuo Li, and Jinming Bai. The bulk Lorentz factors of Fermi-LAT GRBs. *Astrophys. J.*, 726:89, 2011.
- [85] En-Wei Liang et al. Constraining GRB Initial Lorentz Factor with the Afterglow Onset Feature and Discovery of a Tight Gamma 0-E iso Correlation. *Astrophys. J.*, 725:2209–2224, 2010.
- [86] Alicia M. Soderberg and Enrico Ramirez-Ruiz. Constraints on the Bulk Lorentz Factor of GRB 990123. *AIP Conf. Proc.*, 662:172–175, 2003.
- [87] M. Ackermann et al. Detection of a spectral break in the extra hard component of GRB 090926A. *Astrophys. J.*, 729:114, 2011.
- [88] M. Ahlers, M. C. Gonzalez-Garcia, and F. Halzen. GRBs on probation: testing the UHE CR paradigm with IceCube. 2011.